Spring 5-1-2020

Impact Resistance of Fiber-Reinforced Composites Using Computational Simulations

Maitham Alabbad
maitham.alabbad@maine.edu

Recommended Citation

Alabbad, Maitham, "Impact Resistance of Fiber-Reinforced Composites Using Computational Simulations" (2020). *Electronic Theses and Dissertations*. 3174.
https://digitalcommons.library.umaine.edu/etd/3174

IMPACT RESISTANCE OF FIBER-REINFORCED COMPOSITES USING COMPUTATIONAL SIMULATIONS

By

Maitham Alabbad

B.S. in Mechanical Engineering University of Maine, 2017

A THESIS

Submitted in Partial Fulfillment of the

Requirements for the Degree of

Master of Science

(in Mechanical Engineering)

The Graduate School

The University of Maine

May 2020

Advisory Committee:

Dr. Senthil S. Vel, Arthur O. Willey Professor of Mechanical Engineering, Co-Advisor

Dr. Roberto A. Lopez-Anido, PE, Professor of Civil Engineering, Co-Advisor

Dr. Zhihe Jin, Professor of Mechanical Engineering

IMPACT RESISTANCE OF FIBER-REINFORCED COMPOSITES USING COMPUTATIONAL SIMULATIONS

By Maitham Alabbad

Thesis Co-Advisors: Dr. Senthil Vel and Dr. Roberto Lopez-Anido

An Abstract of the Thesis Presented
in Partial Fulfillment of the Requirements for the
Degree of Master of Science
(in Mechanical Engineering)
May 2020

Composite materials are widely used in aerospace, automotive and wind power industries due to their high strength-to-weight and stiffness-to-weight ratios and their improved mechanical properties compared to metals. The damage resistance of composite materials due to low velocity impact depends on fiber breakage, matrix cracking and delamination between the interfaces. In this research, a numerical investigation of low velocity impact response of a multidirectional symmetric carbon-epoxy composite laminate is carried out and presented. Two different finite element models are developed for composite laminates made of non-crimp fabric to investigate their behavior under different levels of impact energy. In the first approach, a finite element homogeneous ply model is generated wherein the heterogeneous plies are replaced by equivalent homogeneous anisotropic plies. In the second approach, a finite element mesoscale model that captures the individual constituents of the composite (i.e., the tows and matrix) has been developed. Different failure criteria have been presented in the literature to predict the damage modes of the composites during and after impact events. The 3D Hashin failure criteria is implemented to predict the intralaminar failure and the surface-based cohesive behavior is implemented to capture the delamination between the plies. Following the low velocity impact investigation, the finite element models are subjected to axial compression to investigate the compressive residual strength after impact, which is a measure of damage tolerance. The numerical predictions, the low velocity impact response as well as the compressive residual strength after impact, are validated with experimental data. The homogeneous ply laminate impacted up to 50 J is seen to be capable of predicting the impact response as well as the compressive residual strength after impact.

ACKNOWLEDGEMENTS

I would like to thank my co-advisors, Dr. Senthil Vel and Dr. Roberto Lopez-Anido for their support, feedback and guidance for the past two years. Also, I would like to acknowledge my committee member, Dr. Zhihe Jin for his help in my undergraduate and graduate career through teaching valuable coursework and technical knowledge.

I would like to thank my family and friends for their support and encouragement to make this happen. I would like also to extend my thanks to Justin McDermott for his feedback and sharing his experimental data with me. Finally, I gratefully acknowledge the Department of Mechanical Engineering and my co-advisors for the financial support for this research work.

TABLE OF CONTENTS

LIST OF FIGURES

LIST OF TABLES

Chapter 1 Introduction

This thesis presents an investigation of carbon fiber-reinforced composites subjected to low velocity impact loading and compression after impact (CAI) using computational simulations. An experimental investigation was previously carried out at the University of Maine's Advanced Structure and Composites Center to analyze the damage resistance and tolerance of 3D woven composites and 2D non-crimp fabric (NCF) composites (McDermott, 2019). The primary objective of this thesis is to assess the damage resistance and tolerance of the NCF composites using computational simulations. This research is carried out to support the usage of composites for industrial applications and expand the knowledge of the mechanical behavior of composites using numerical tools. In this study, finite element models of NCF composite are developed to analyze their behavior under low velocity impact loading. Different damage models are used to determine the effect of impact loading and predict the compressive residual strength of the composite after impact. A finite element analysis is performed using ABAQUS to assess the extent of damage and the compressive residual strength of the laminated composites. The computational results are validated with the experimental results presented by McDermott (2019).

1.1 Background

A composite material is formed by a combination of two or more materials to form a new material. The most common composites are those made from fibers and held together in a binder (Barbero, 2011, p.1). Composite material includes a very wide selection of the available materials, such as fiber-reinforced polymers, metal matrix composites, ceramic matrix composites and reinforced concrete.

Carbon fiber-reinforced composites have been widely used in industrial applications. Many factors that influence the use of composites such as the weight reduction, high stiffness and strength, resistance to fatigue damage and corrosion resistance. These factors enhance the use of composites in some applications, most frequently in aerospace and transportation industries.

Composite structures subjected to different types of loading can reduce the strength of the structures significantly. Impact loading is one of the most concerning loading in composite structures. Impact due to tool drops or flying debris on a runway can introduce significant damage in composite structures. Some damage in composite structures are internal and cannot be detected by visual inspection in which this damage grows under load and can significantly reduce the load carrying capacity of the structure (Abrate et al., 2011). Damage in composite structure has been investigated experimentally and numerically. The finite element method plays an important role in the industry to develop numerical tools, which could help to improve the performance of composite structures. Numerical modelling makes it possible to accurately generate the laminated composite models and simulate the mechanical behavior of composites under different types of tests such as impact loading. This thesis presents a prediction of the mechanical behavior of carbon fiber-reinforced composite subjected to impact loading as well as predict the compressive residual strength of the laminated composite after impact. During the impact process, the composite absorbs the impact energy in the form of various damage modes, such as fiber breakage, matrix cracking and delamination. In order to enhance the impact resistance and damage tolerance of the composite materials, various damage modes during the impact need to be investigated using failure criteria that predict intralaminar failure (such as fiber and matrix failure) as well as interlaminar failure (such as delamination).

1.2 Literature review

In many industries, the application of fiber reinforced composite materials has seen a rapid growth in structural applications, especially in the aerospace industry in the past few decades. Composite materials are used in the aircraft industry in the mid-1960s and early 1970s. The military was the first users of composite material where it was applied on the F-14 and F-15 fighter aircraft (Safri et al., 2014). Fiber reinforced composite materials allow for numerous direct and indirect benefits over traditional metals and metallic alloys, which generally results in lighter weight structures. Additionally, fiber reinforced composite materials have a better fatigue performance and resistance to corrosion compared to metals. Fiber reinforced composite materials are naturally brittle and generally display a linear-elastic response up to failure without any plastic deformation (Dogan et al., 2012).

Composite structures might experience structural failure and damage due to void in the microstructure of the material, existence of a notch and corrosion of the material (Findlay et al., 2002). Composites in structural applications or aircraft structure are exposed to many kinds of impact loading during the process of manufacturing as well as in service (Hirai et al., 1998). Impacts are considered one of the dangerous and unsafe types of loads because it affects the performance of the composite laminates. It can be categorized as a low velocity impact, intermediate impact and high velocity impact (Naik et al., 2004). The low velocity impact occurs at a velocity below 10 m/s, intermediate impact occurs between 10 m/s and 50 m/s and high impact occurs in the range of velocity from 50 m/s to 1000 m/s (Vaidya et al., 2011). For low velocity impact, this event occurs mostly in service of during maintenance activities (Mathivanan et al., 2010). While high velocity impact events occur mostly during take-off, flight and landing of the aircraft. In addition, bird strikes are one of the major causes of high velocity impact due to high probability of occurrence (Pernas-Sanchez et al., 2012). When a bird strikes an aircraft, the relative velocities between the two bodies are so high that the material of the aircraft could undergo instant failure (Mathivanan et al., 2010). Damage types/modes that might occur in composite laminates due to impact are intralaminar failure such as matrix failure and fiber failure and interlaminar failure or delamination (Zumpano et al., 2008). Matrix failure usually takes the form of matrix cracking and it happens due to the transverse low velocity impact (Vaidya et al., 2011). Matrix cracking is the first type of damage caused by impact and usually occurs parallel to the fibers due to tension, compression and shearing (Sjoblom et al., 1988). However, delamination is the most critical damage mechanism in composites due to impact. Delamination occurs between the plies in the laminated composite (Prichard et al., 1990). Delamination or separation between the plies happens due to bending stiffness difference between adjacent plies, whereas fiber failure occurs due to high stress field and indentation effects. Fiber damage usually exists after matrix cracking and delamination in the composite. The fiber damage is mostly found just below the impactor as well as in the back face/surface due to high bending stress (Vaidya et al., 2011).

Damage modes are commonly dependent on several parameters such as type of load applied, model geometry, constituent material, laminate layup, impact velocity and location of the impact

(Carruthers et al., 1998 and Hull et al., 1991). The location of the impact region is an important factor to understand the damage of the impact. A study conducted in the past few years (Breen et al., 2006) shows that the damage formation and levels of strength reduction are different for central and edge impacts. Edge impact is found to cause a greater reduction in compressive strength while a central impact causes more tensile strength reduction. Likewise, the impact velocity plays an important factor in the type of damage and the damaged area. Comparing the low velocity impact with high velocity impact for the same impact energy, it was found that the energy absorbed during low velocity impact was about 40 % lower than that of the high velocity impact. In addition, the damage area of the low velocity impact was observed to be about 20 – 30 % smaller than the high velocity impact, and the damage area increased as the mass decreased for high velocity impacts (Zumpano et al., 2008).

Impact situations can be simulated by performing drop weight impact simulations using a finite element package software such as LS-DYNA and ABAQUS. A drop weight impact allows the simulation of a wide variety of real-world impact situations and collect detailed performance data to improve the performance of composite structures (Mathivanan et al., 2010). For modeling purposes, a failure criterion is required to simulate damage and identify the damage mode such as fiber or matrix failure. For intralaminar failure, some failure criteria are general which do not have the capability to detect the failure modes such as Tsai-Wu criterion, Tsai-Hill criterion and Azzi-Tsai-Hill criterion. Various other failure criteria have been proposed in the literature such as Hashin and Rotem failure criteria (1973), Hashin failure criteria (1980) and Puck failure criteria (2002). Hashin and Rotem and Hashin proposed a quadratic failure criterion in the form of material strengths, where each branch of the criteria represents a failure mode.

Several researchers have used the 3D Hashin failure criteria successfully to predict the intralaminar damage in fiber reinforced composite under low velocity impact (Megat-Yosoff et al., 2019). Guo et al. (2013) used 3D Hashin failure criteria and exponential damage evolution function to avoid a sudden decrease in the stiffness which may cause stiffness matrix singularities. In addition, Maio et al. (2013) used the 3D Hashin failure criteria for intralaminar failure initiation and exponential law proposed by Matzenmiller et al. (1995) for damage evolution. The proposed damage model predicted delamination in a form of peanut shape and size, aligned along the fiber direction. Zhang et al. (2015) used the three-dimensional failure criteria proposed by Hashin and Hou et al. (2000) to predict failure in braided composites.

As previously mentioned, interlaminar damage failure or delamination is the most critical and an important failure mode in composite materials under impact loading. Cohesive zone modeling is the most widely used delamination modeling approach in which the interface is modeled independently, and it does not require the knowledge of the crack position. In cohesive zone modeling, both damage initiation and damage propagation are modeled separately. The failure criteria in terms of interface stresses are used to predict delamination initiation, whereas the fracture mechanics-based approach is used to predict delamination evolution (Megat-Yosoff et al., 2019). However, Zhang et al. (2015), Topac et al. (2017) and Abir et al. (2017) used the surface-based cohesive behavior to implement delamination between the plies under the assumption of zero thickness zone of the cohesive zone. This modeling scheme is based on master/slave surfaces, which follows bilinear traction separation or displacement law and it is computationally efficient.

Damage tolerance is defined as the capability of a structure to continue performing their intended functions with some tolerable level of damage (Abir et al., 2017). In composites, damage tolerance is determined by measuring the residual strength of the composite structure. The common approach to perform damage tolerance analysis is to carry out an impact test followed by a CAI test to obtain the residual strength of the structure. There has not been too much research carried out on compression after impact tests using computational simulations. Abir et al. (2017) developed a finite element (FE) model to perform low velocity impact followed by CAI test. The author implemented the maximum stress and Tsai Wu failure criteria for damage initiation. It was observed that failure under CAI was due to local buckling and delamination growth. Also, the important parameters that affect the residual strength of composites were the Mode-II interlaminar fracture toughness and fiber compressive fracture toughness. Increase in the Mode-II interlaminar fracture toughness reduces delamination size and increases damage tolerance. Gonzalaz et al. (2012) performed low velocity impact and CAI simulations using interlaminar and intralaminar damage models. The FE model predicted the compressive strength after impact and compared it with an experiment where there is about 20% error between simulation and experiment data. Waas et al. (2018) developed continuum shell-based FE models to simulate the response of composite structure under impact loading the compression after impact loading. The FE models predicted the compressive strength after impact within 7.2% in some cases while others ranged up to 14.4%.

1.3 Approach

In this study, two approaches are considered to develop the finite element models of composites and investigate their behavior under low velocity impact loading. The first approach is to develop a homogeneous ply model as a plate where the material of the plate is considered to be equivalent throughout the plate; therefore, there is no distinction between its constituents. Second approach is to develop a mesoscale model as a plate which consists of tows geometries as well as matrix geometries where the constituents of the plate are considered as different parts. The orientation of the plies for the both models vary from layer to layer.

In the first investigation of this study, the modeling of mesoscale composites is presented. The mesoscale finite element models are generated using TexGen software, which is an open source software for modeling the geometry of composite structures such as woven and non-woven composites. The mesoscale parameters, such as the tow height, tow spacing, tow width and ply thickness, for the modeling purposes are approximated through experimental examination. Then, unit cell models are generated using TexGen to predict the effective elastic properties (homogenized properties) and to determine the appropriate mesh size for the mesoscale models.

In the second investigation, preliminary finite element analysis is performed using mesoscale models and homogeneous ply models to examine the structural response of both models subjected to different types of loads and compare them to each other. The structural analysis is performed within the finite element analysis package ABAQUS. The structural response of the mesoscale and homogeneous ply models is analyzed by performing static simulations of tensile loading and flexural loading. The reason for performing the structural analysis is to ensure that both models give the same structural response under certain types of static loadings before moving to more complicated problems such as dynamic loadings.

In the next investigation, the modeling technique for the NCF laminated composites is presented. The NCF laminated composites are used for the low velocity impact and CAI simulations. A finite element homogeneous ply model and a finite element mesoscale model are developed to investigate their mechanical behavior under impact loading. The homogeneous ply model is generated within ABAQUS while the mesoscale plies are generated using TexGen. The mesoscale plies are imported into ABAQUS for further assembly. In this study, all the parts/models are generated with the use of continuum/solid elements. Solid elements have three translational degrees of freedom for each node. Since this research is carried out to study the behavior of composites subjected to impact loading, the transverse response or the through thickness response is important to predict more accurate results. The solid elements are capable of predicting the transverse response more accurately compared to other element types such as shell elements. The disadvantage of solid elements is that it requires more elements compared to shell elements to produce results with high accuracy.

In the next investigation, the mechanical behavior of the NCF laminated composites is investigated under low velocity impact loading in ABAQUS. There are two models that are analyzed under impact loading. The NCF laminates used in this investigation are the mesoscale model and the homogeneous ply model. The NCF laminates are impacted with different energy levels to examine the damage accumulation of the models. The 3D Hashin failure criteria and the exponential damage evolution law are used in this study to evaluate the intralaminar damage during impact. Additionally, the interlaminar damage is evaluated through the use of the quadratic stress criterion and the Benzeggagh-Kenane (BK) mixed mode fracture law based on the fracture energy release rate method. Once the impact response is simulated for the NCF laminates, CAI simulations are performed to predict the damage tolerance of the NCF composites. Finally, the simulations results are validated with experimental investigation.

1.4 Contributions

The aim of this research is to expand the knowledge of the mechanical behavior of carbon fiber reinforced composites subjected to low velocity impact loading and predict the compressive residual strength of the composites after impact. The contribution of this research falls into the category of computational simulations. Numerical analysis tools are developed to help the industry and institutions to improve and examine the performance of composite structures. This tool is used to perform damage analysis of laminated composite models. In addition, a Fortran subroutine is developed to implement the damage models of the intralaminar failure and to evaluate the laminated composites during and after impact events.

The simulations of impact and CAI of the laminated composite models are investigated using the FE package ABAQUS. Most of the literature consider only a homogeneous ply model to examine the mechanical behavior of the laminates under impact loading. In this study, a mesoscale model is considered as well to provide a more detailed description of the damage from the impact event. The impact response of the mesoscale model is predicted and compared to the response of the homogeneous ply model and both models are validated with experimental data.

1.5 Thesis outline

This thesis is organized as follows, the second chapter focuses on the modeling technique used in this study and preliminary finite element analysis. The third chapter presents the details of impact simulations modeling and the mechanical behavior response of the NCF laminated composite models under impact loading. The fourth chapter details the modeling of CAI simulations and the response of the NCF laminated composites. Conclusions and recommendations are summarized in the fifth chapter.

Chapter 2 Modeling of Non-Crimp Fabric Composites

2.1 Introduction

The intention of this study is to investigate the behavior of composite laminates under impact loading and compression after impact (CAI). The composite laminates studied in this thesis are a multidirectional fiber-reinforced composite and consist of 24 layers. An important part of the modeling purposes is the prediction of the effective elastic properties through a homogenization process using unit cell finite element models. The unit cell models can be defined as the smallest material volume element for which the macroscopic model is sufficient to represent the whole model. The unit cell model can provide sufficient accuracy of representing the material's larger scale (Omairey et al., 2019). Figure 2.1 illustrates a schematic of fiber arrays and its corresponding unit cell. A convergence study is carried out using unit cell models to determine the homogenized elastic properties and the appropriate mesh size. Additionally, a preliminary finite element analysis is performed to study the structural response of a lamina as well as laminates under plane tensile and flexural loading. A mesoscale finite element model and homogeneous finite element model are developed for the structural analysis. The mesoscale model consists of tows geometries and matrix geometries whereas the homogeneous ply model is just a plate with using the smeared elastic properties. Both models are used to investigate a lamina as well as laminate plates.

The modeling of the unit cell, convergence study and structural analysis are discussed in detail in this chapter. In addition, the generation of the composite laminate models for the impact and

CAI simulations are discussed as well. The finite element modeling technique and the modeling assumptions are presented in detail along with the modeling software used.

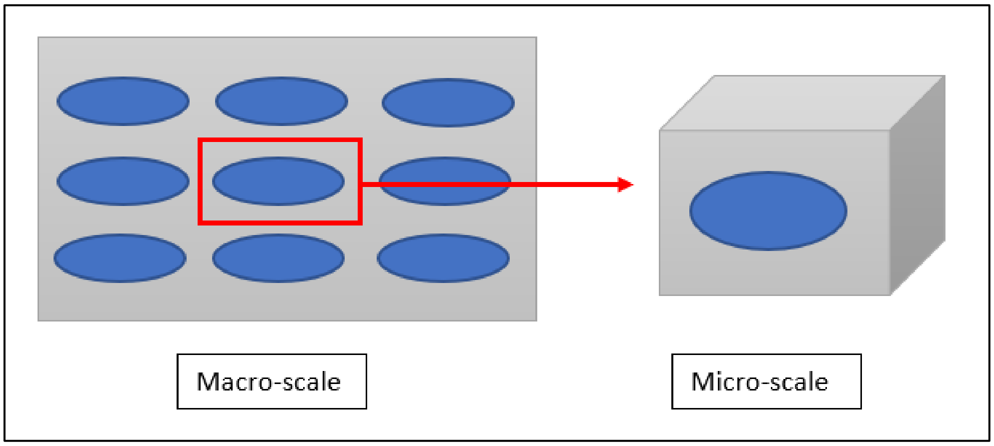

Figure 2. 1 Macroscale of fiber arrays and its corresponding unit cell

2.2 Unit Cell Modeling

Each lamina consists of multiple in-plane tows that are embedded in a matrix. The properties of a lamina are predicted through the use of unit cell models. The unit cell model represents the microstructure of a single ply of unidirectional composites as shown in Figure 2.1. The unit cell is a rectangular shape with a single tow through the thickness. The procedure of predicting the elastic properties is called a homogenization process. The effective properties predicted, which depend on the fiber and matrix properties as well as the fiber volume fraction and tow geometry, are referred to as the homogenized or smeared properties.

2.2.1 Generation of Unit Cell

A non-crimp fabric (NCF) composite is investigated experimentally and presented by McDermott (2019), and the purpose of this study is to investigate the NCF composite numerically. A representative microstructure of the actual NCF composite is shown in Figure 2.2. As can be seen from the image, the tows have an elliptical shape. Accordingly, the unit cell is modeled with a rectangular shape consisting of one elliptical tow that is surrounded by the matrix material. The unit cell models are constructed using TexGen software. The parameters required for modeling the unit cell are the tow width a, tow height b, tow spacing w and ply/unit cell thickness h. The dimensions are approximated based on the experimentally obtained microstructure image of the actual non-crimp fabric specimen, shown in Figure 2.2. The microstructure image was analyzed in an image processing program to approximate the needed parameters. The tow spacing is approximated by measuring the distance between the centers of 5 adjacent tows, calculating the average distance between the neighboring tows. The tow width is determined by measuring the width of multiple tows and taking the average. The ply thickness is obtained by dividing the total specimen thickness by the number of layers. Lastly, the tow height is difficult to be approximated from the microstructure image; therefore, it was assumed to be $b = 0.98*h$. Figure 2.3 shows a sketch of the cross section of the unit cell model along with the tow cross-section. The corresponding unit cell parameters are listed in Table 2.1.

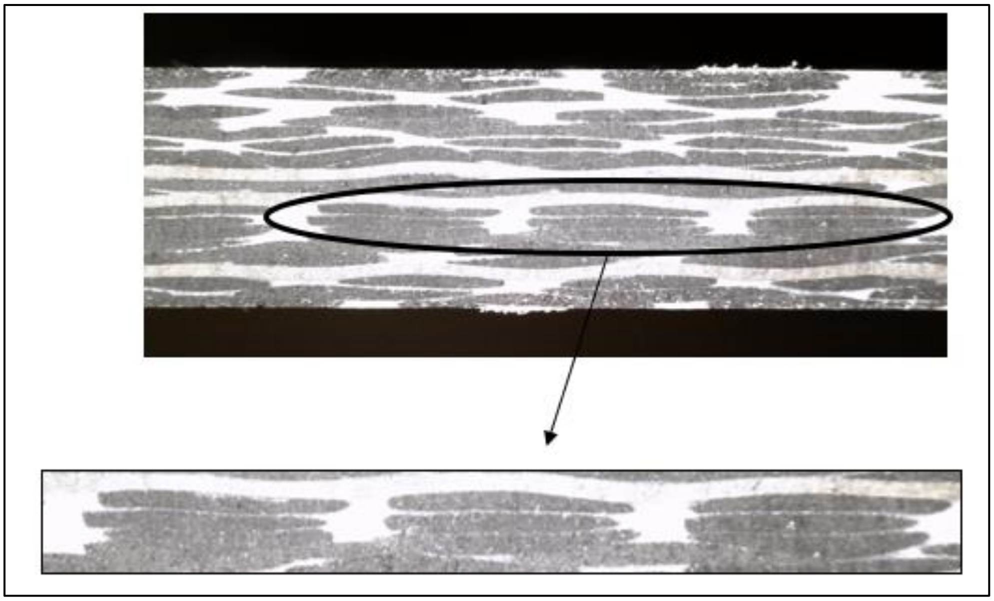

Figure 2. 2 A microstructure image of the NCF specimen

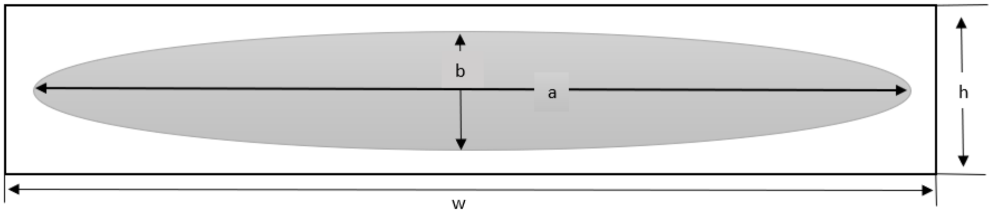

Figure 2. 3 Unit cell and tow cross section

Table 2. 1 The tow parameters used for the unit-cell

Unit-cell Parameters	
Tow width *a* (mm)	2.345
Tow spacing *w* (mm)	2.355
Tow height *b* (mm)	0.1823
Ply thickness *h* (mm)	0.186

The unit cell models are generated through a Python script which takes as an input the unit cell parameters. Additionally, through the use of the available built-in functions/libraries within TexGen, the developer can specify the tow's cross section, tow's path, tow repetition in the X-Y space, tow resolution and assign unit cell domain. TexGen modeling flow chart is illustrated in

Figure 2.4. This script can be run through TexGen and visualize the model within TexGen GUI. A 3D unit cell model generated in TexGen is shown in Figure 2.5.

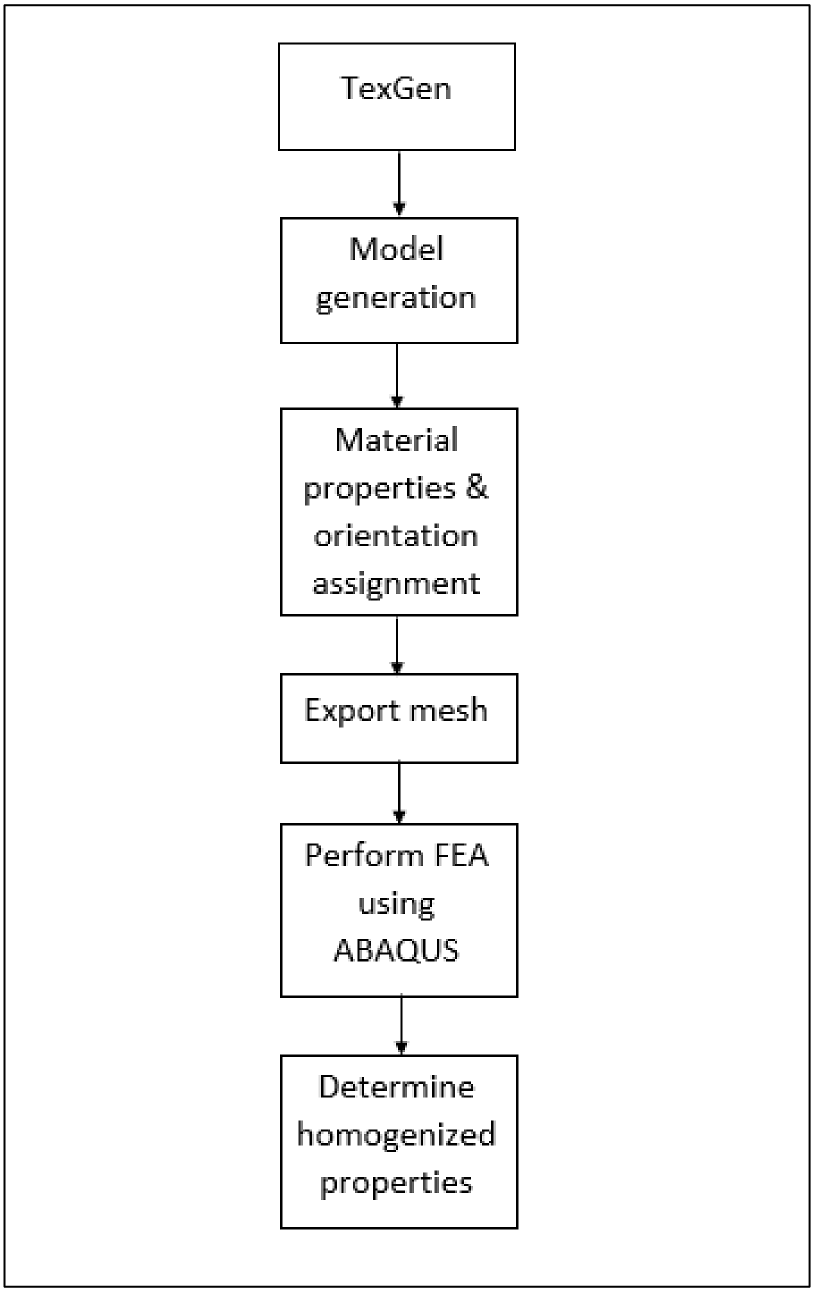

Figure 2.4 TexGen modeling flow chart

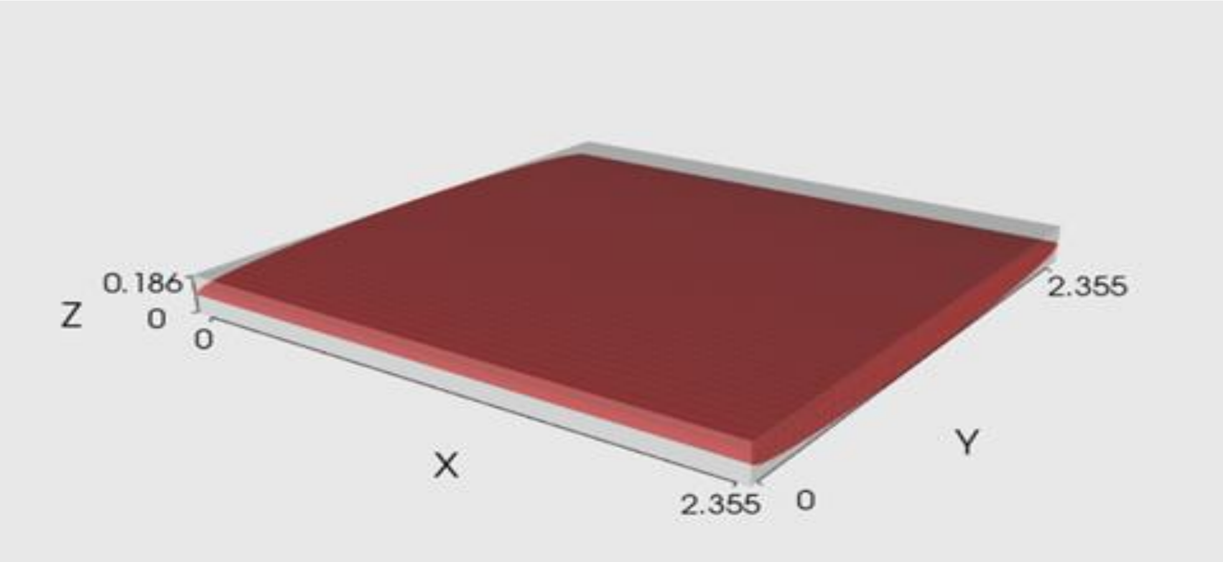

Figure 2.5 Unit-cell model generated in TexGen

The NCF composite is fabricated using 12K fiber filament count tows. The fiber volume fraction V_f is found to be 57.2 % experimentally by performing acid digestion test. The unit cell is modeled using the tow's parameters listed in Table 2.1 to predict the V_f that is approximately close to the experimental value. TexGen has the capability to predict the total fiber volume fraction which the fiber density and tow linear density need to be assigned to the tows in order to predict the total V_f accurately. The fiber volume fraction V_f of the composite is the product of the fiber volume fraction within the tows and the volume fraction of the tows:

$$V_f = V_f^{tow} * V_{tow} \tag{2.1}$$

where V_f is the composite fiber volume fraction, V_f^{tow} is the fiber volume fraction within the tow and V_{tow} is the tow volume fraction . The carbon fiber properties used in this study are the IM7 carbon fiber properties from HEXCEL. The fiber density, fiber linear density and a comparison of V_f between the experimental and predicted values are listed in Table 2.2.

Table 2.2 IM7 carbon fiber properties and fiber volume fraction V_f comparison.

IM7 Carbon Fiber Properties (12K)	
Linear density (g/m)	0.446
Fiber Density (g/cm^3)	1.78
TexGen Prediction of V_f (%)	
V_f^{tow}	74.68
V_{tow}	76.44
Unit cell V_f	57.09
Experimental V_f	57.2
% Difference	0.19

The predicted fiber volume fraction within the tow V_f^{tow} and the tow volume fraction V_{tow} are found to be 74.68 % and 76.44 % respectively. The product of the V_f^{tow} and V_{tow} give a unit cell fiber volume fraction V_f to be 57.09 % with a difference of 0.19 % compared with experiment. The predicted unit cell fiber volume fraction V_f is in good agreement with the experimental fiber volume fraction. This small percentage difference of 0.19 % gives confidence in the unit cell models for homogenization studies.

2.2.2 Voxel Mesh Technique

Generating a mesoscale model for a composite material can be challenging due to the complex architecture of the tow and the surrounding resin. In this study, a voxel mesh technique is used to mesh the geometry of the mesoscale model. However, conformal mesh technique has also been investigated in this study. The conformal mesh technique is based on the use of tetrahedral elements, and the use of conformal mesh technique in FE analysis results in element distortion specifically in the tow region due to the mesoscale's structure complexity. A solution is proposed by TexGen developers to address mesh distortion that uses an artificial gap between the tow's surface and the matrix elements surrounding the tow . This artificial gap strategy is done through TexGen and it introduces a contact area to eliminate the tow's surface/elements from interfering with the surrounding matrix elements which in this way reduce the elements' distortion. However, this strategy can be questioned if it has an influence on the end goal results accuracy and therefore it requires more investigation to validate this method. Additionally, another strategy to reduce element distortion for the conformal mesh technique is to increase the number of elements. However, this approach is not efficient because it would be computationally expensive. A unit cell model is generated with a conformal mesh technique as shown in Figure 2.6. The model shown in the left side is generated with a coarse mesh and the model shown in the right side is generated with a fine mesh. The elements that have severe distortion are shown in yellow. As shown in Figure 2.6, the coarse mesh has severe element distortion and as the number of elements increases, the element distortion decreases but the element quality is still poor especially in the boundaries of the tow (the straight yellow band of elements in the fine mesh).

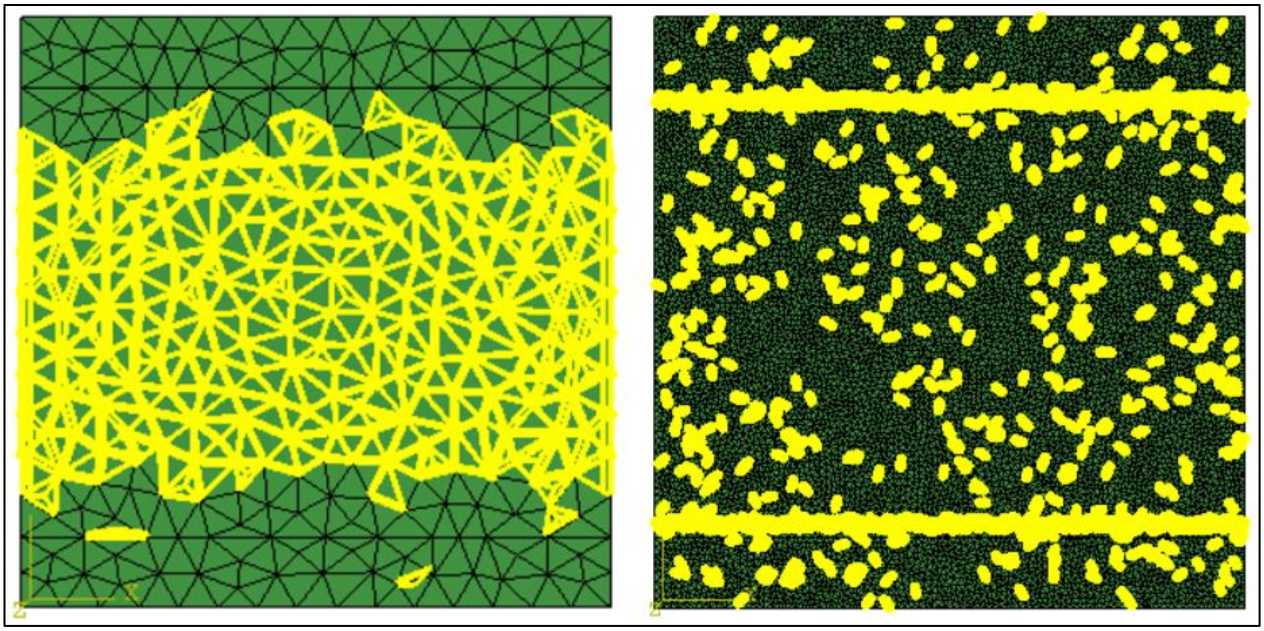

Figure 2.6 Unit cell with conformal mesh technique

The voxel mesh consists of square/rectangular hexahedral elements (C3D8, eight-node brick element). The voxel mesh can be generated without any artificial changes in the composite geometry. However, due to the type of element used in the voxel meshing technique, it is difficult to capture the mesoscale model geometries very well. The mesh quality is improved by using a large number of elements which enhances the resolution of the mesh and also captures the mesoscale geometry (tow's geometry) very well. The mesh for the mesoscale/unit cell model for this study is generated in TexGen. Figure 2.7 shows a tow cross-section and FE unit cell model with a voxel mesh technique generated within TexGen.

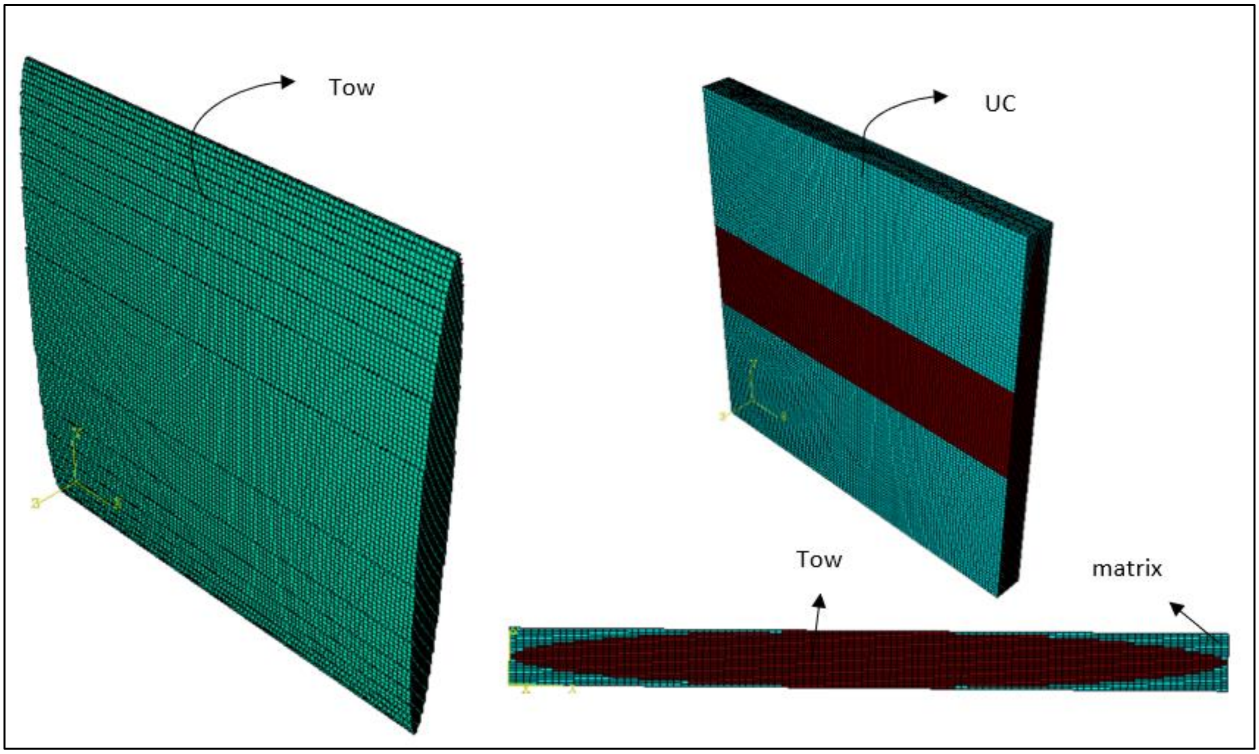

Figure 2.7 Tow cross section and unit cell model generated in TexGen with voxel mesh technique

2.2.3 Boundary Conditions

The unit cell models are constrained by implementing periodic boundary conditions. The periodic boundary conditions can be easily applied within TexGen. The periodic boundary conditions are implemented by creating node-to-node equation constraints in which the nodes from one side (e.g. left side) are tied to the corresponding nodes in the other side (e.g. right side). The nodes on opposite sides are constrained to a reference point so that the displacement of the nodes on the opposite sides are equal to the displacement applied to the reference point. More details on the periodic boundary conditions and its application, can be found in Li et al. (2001). The periodic boundary conditions used in this study is to ensure the displacement in opposite sides of the unit cell models move the same displacement and also to ensure stress continuity.

As mentioned previously, TexGen has the ability to apply periodic boundary conditions and generate the mesh of the unit cell models. These unit cell models are exported as an ABAQUS input file from TexGen along with its mesh and boundary conditions. Subsequently, the unit cell models are imported into ABAQUS to perform a convergence study and estimate the effective elastic properties of the composite.

2.2.4 Convergence Study

Mesh density is an important factor when it comes to accuracy of the results. Capturing the geometry of the tows of the mesoscale/unit cell models require high mesh density. As the mesh gets finer, the finite element analysis gets more computationally expensive. Thus, it is important to determine the appropriate mesh size to obtain converged results within a reasonable time. To perform the convergence study, several unit cell models are generated using TexGen as described in section 2.2.1 with different mesh sizes to perform the convergence study. The ABAQUS input files are exported from TexGen, and each ABAQUS file has the model information with its voxel mesh and boundary conditions. Before post processing the input file, a small modification to the material definition is made in ABAQUS input file to define the proper epoxy matrix properties and impregnated tow elastic properties. The properties of the impregnated tow and epoxy matrix are listed in Table 2.3 and 2.4. The impregnated tow elastic properties are obtained based on an experimental investigation reported by Warren et al. (2016).

Table 2.3 Impregnated tow elastic properties

Tow Elastic Properties			
E_{1t}	180 GPa	X_T (MPa)	1810
E_{2t}	9.45 GPa	X_c (MPa)	669
E_{3t}	9.45 GPa	Y_T (MPa)	64.0
v_{12t}	0.433	Y_c (MPa)	174
v_{13t}	0.433	S_{12} (MPa)	105
v_{23t}	0.465	S_{13} (MPa)	105
G_{12t}	6.67 GPa	S_{23} (MPa)	105
G_{13t}	6.67 GPa		
G_{23t}	3.23 GPa		

Table 2. 4 Isotropic epoxy matrix properties (PR-520)

Matrix Properties			
E_m	4 GPa	Tensile Strength (MPa)	82.1
v_m	0.398	Compressive Strength (MPa)	128
		Shear Strength (MPa)	61.4

2.2.4.1 Convergence Study Results

A total of 21-unit cell models are generated in TexGen with different mesh sizes to determine the converged homogenized elastic properties. Three parameters, namely the voxels in the X, Y and Z directions, need to be chosen for the mesh generation. The convergence study is divided into four different studies. In each study, the number of voxels in the axial (X) and thickness (Z) directions are held fixed and the number of voxels in the transverse (Y) direction is varied. This approach is to minimize the number of voxels in Y and Z directions and still obtain converged elastic properties. The Y and Z voxels are important parameters which they have a huge influence on capturing the unit cell geometry (i.g. the tow's geometry). The number of voxels in X direction is fixed to be 5 voxels for all unit cell models since it does not influence the unit cell geometry and the accuracy of the results. The number of voxels in Y direction vary from 50 to 6000 voxels in each study. The number of voxels in Z direction are selected to be 12, 14, 20 and 30 voxels for the first, second, third and fourth study, respectively.

The effective elastic properties are post-processed in ABAQUS by using a Python script. This script is developed to calculate the stresses and strains from the reaction forces and the prescribed displacements. The average composite normal stress σ_i is calculated by taking the reaction force and dividing it by the surface area. Additionally, the axial strain ε_i is calculated by dividing the prescribed displacement by the length of the unit cell along the corresponding direction. Thereafter, the Young's modulus E_i is obtained by dividing the average normal stress by the axial strain as illustrated in equation (2.2). Furthermore, the Poisson's ratio v_{ij} is obtained by dividing the transverse strain by the axial strain as illustrated in equation (2.3).

$$E_i = \frac{\sigma_i}{\varepsilon_i} \tag{2.2}$$

$$v_{ij} = \frac{-\,\varepsilon_j}{\varepsilon_i} \tag{2.3}$$

The shear modulus G_{ij} is obtained by dividing the shear stress τ_{ij} by the shear strain Υ_{ij} in a similar approach as the Young's modulus. The shear modulus is calculated as illustrated in equation (2.4).

$$G_{ij} = \frac{\tau_{ij}}{\gamma_{ij}} \tag{2.4}$$

The results of the FE converged effective properties are obtained for the four convergence studies. The FE results of E_1 and G_{12} are compared with the Mori-Tanaka approach and illustrated in Figures 2.8 - 2.11. In Figure 2.8, the properties start to converge around 2000 voxels in the Y direction whereas in Figure 2.9, the properties start to converge around 1500 voxels in the Y direction. This indicates that as the number of voxels in Z direction increases, the smaller number of voxels in Y direction is needed to obtain the converged effective properties. This results in a smaller number of elements required to obtain converged results as seen in Figures 2.10 and 2.11, the properties start to converge around 950 voxels in the Y direction.

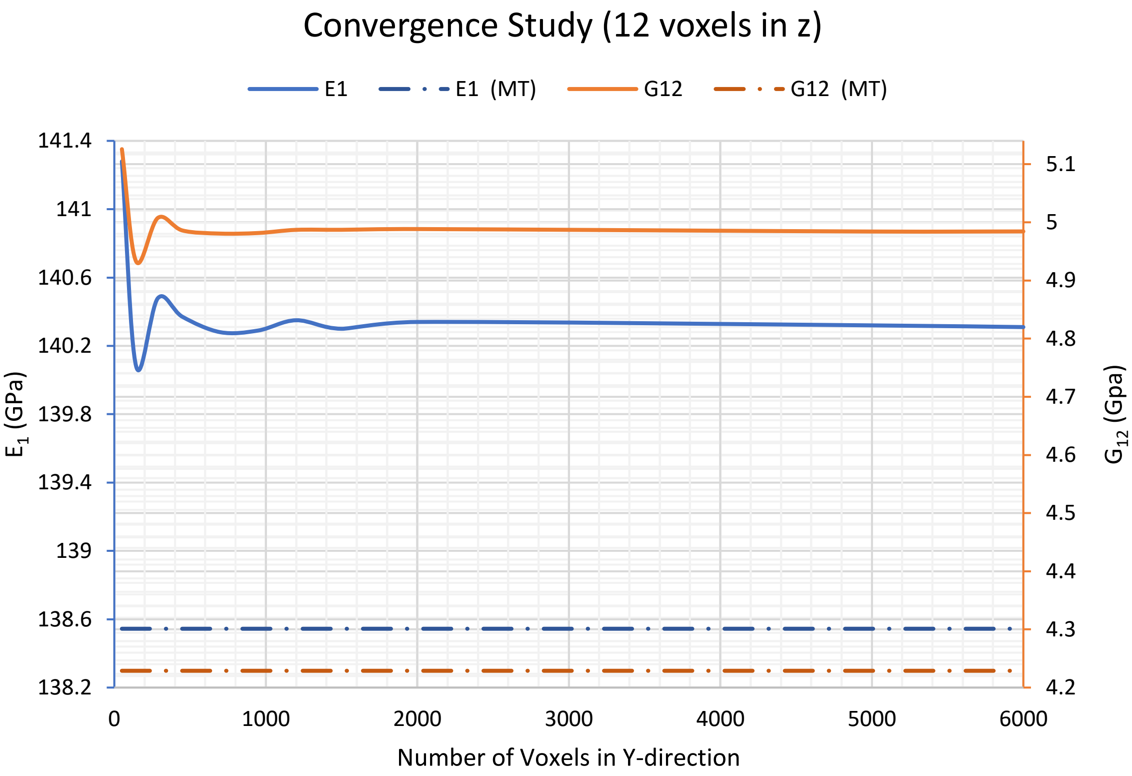

Figure 2.8 Plot of E_1 and G_{12} versus the number of voxels in Y direction with Z voxels is held fixed to 12 voxels

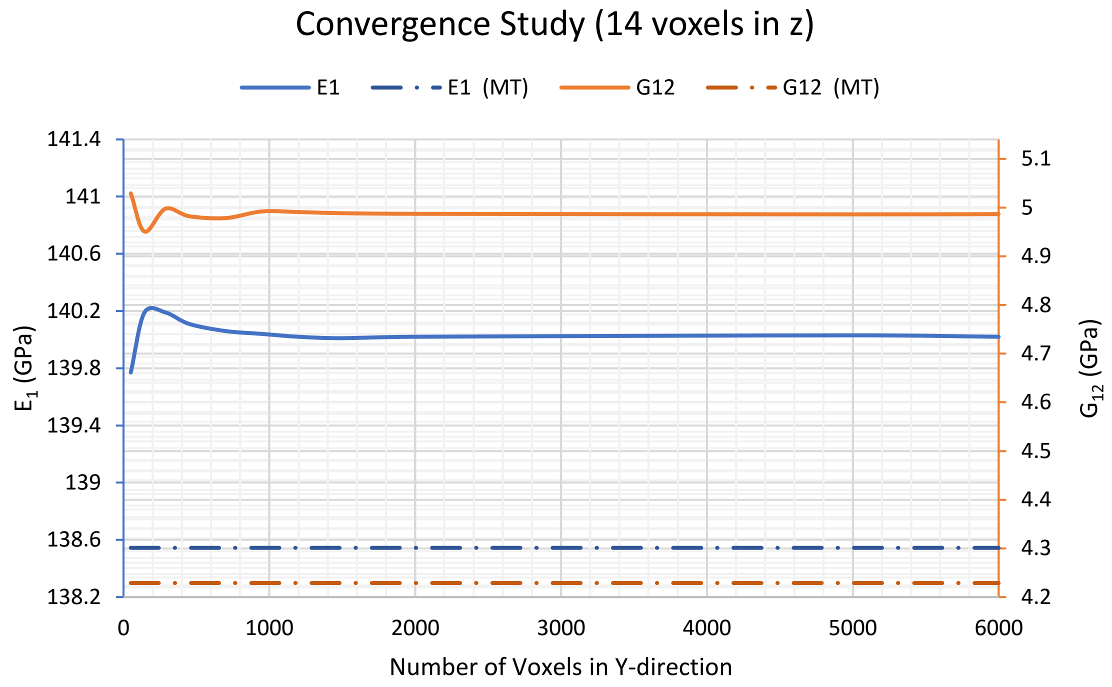

Figure 2.9 Plot of E_1 and G_{12} versus the number of voxels in Y direction with Z voxels is held fixed to 14 voxels

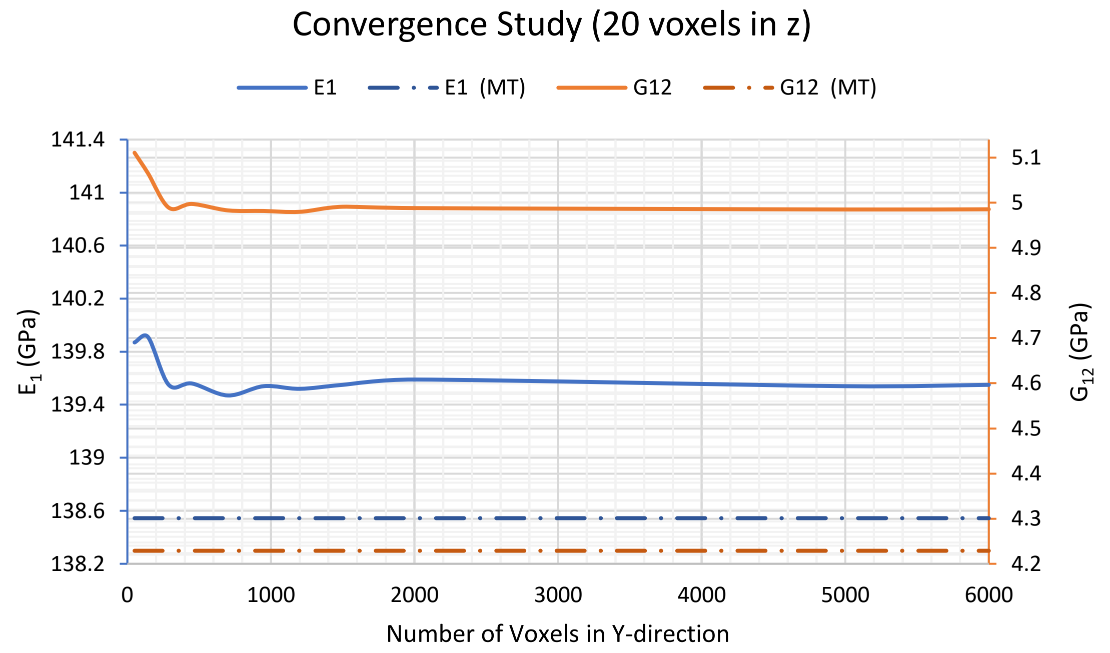

Figure 2.10 Plot of E_1 and G_{12} versus the number of voxels in Y direction with Z voxels is held fixed to 20 voxels

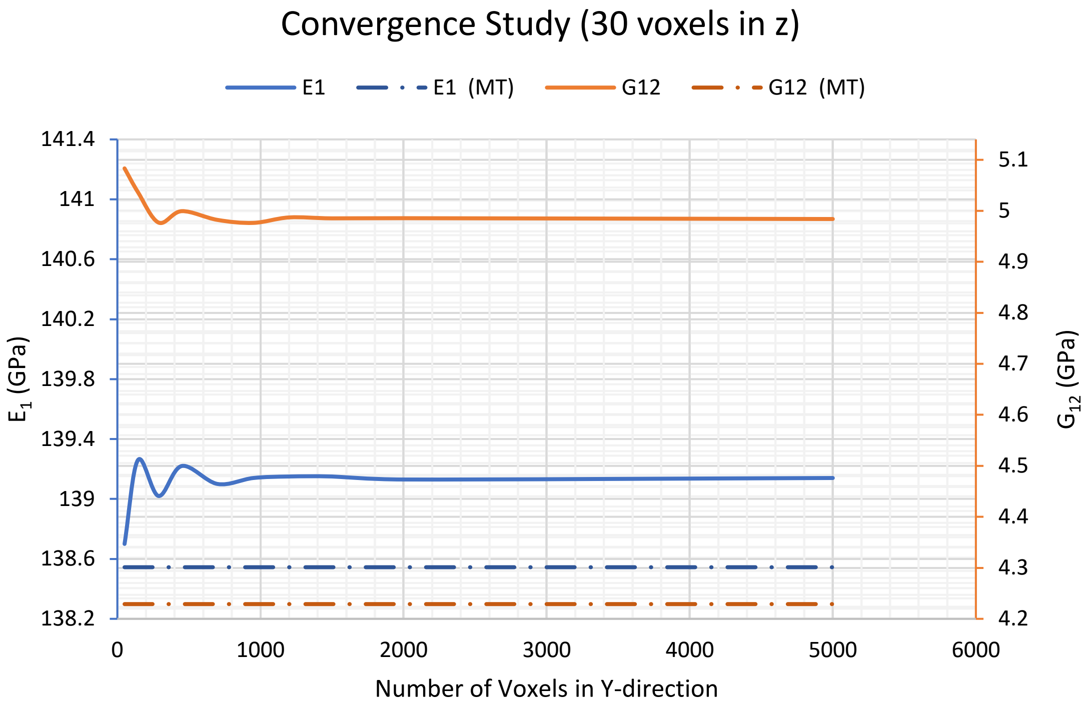

Figure 2.11 Plot of E_1 and G_{12} versus the number of voxels in Y direction with Z voxels is fixed to 30 voxels

The convergence study is used to determine the number of elements required to obtain accurate FE results. As seen in Figure 2.11, the effective elastic properties converge around 950 voxels in the Y-direction and the computed properties correlate well compared with the Mori-Tanaka approach. Comparing the results presented in Figures 2.10 and 2.11, there is no significant difference in both moduli E_1 and G_{12}. Therefore, a small number of voxels in Z direction is used, 20 voxels, since there is no significant difference to the results of using 30 voxels in Z direction. A comparison between the converged FE elastic properties with Mori-Tanaka method is shown in Table 2.5. overall, the FE results found to be close to the approximated properties using the Mori-Tanaka method. The shear modulus G_{12} has a large percentage difference between FE approach and Mori-Tanaka method. This is because the Mori-Tanaka method approximates the elastic properties based on the assumption that the tow has a circular cross-section whereas in this study the tow has more of an elliptical cross-section.

Table 2.5 Comparison of FE effective properties and Mori-Tanaka approach

Effective Properties	**FE Approach**	**Mori-Tanaka Method**	**FE and Mori-Tanaka %Difference**
E_1 (GPa)	139.54	138.5443	0.7161
E_2 (GPa)	8.276	7.8981	4.6729
E_3 (GPa)	8.2018	7.8981	3.7727
ν_{12}	0.4265	0.42501	0.3500
ν_{13}	0.4242	0.42501	0.1908
ν_{23}	0.5013	0.51708	3.0990
G_{12} (GPa)	4.9818	4.2289	16.3484
G_{13} (GPa)	4.3491	4.2289	2.8025
G_{23} (GPa)	2.5168	2.6031	3.3712

2.3 Structural Analysis

A preliminary finite element analysis (FEA) is performed in ABAQUS using mesoscale models and homogeneous ply models. The mesoscale models of lamina and laminate are generated in TexGen using the impregnated tow elastic properties and matrix properties listed in Table 2.3 and Table 2.4, respectively. Whereas the homogeneous ply models of lamina and laminate are generated in ABAQUS using the converged FE elastic properties (homogenized properties) presented in Table 2.5. The structure response of both models is analyzed by performing static simulations of tensile and flexural tests.

Models of one ply with orientation of 0^{o} and 45^{o} and laminates with orientation of $[\pm 45^{o}]_s$ and $[0^{o}/90^{o}]_s$ are developed for the structural response analysis of both mesoscale and homogeneous ply models. The lamina and laminate dimensions used are 14.13 mm x 14.13 mm x 0.186 mm and 14.13 mm x 14.13 mm x 0.744 mm, respectively. Number of elements generated for lamina and laminate models are listed in Table 2.6. The mesoscale model is meshed using 8-node linear brick C3D8 and the homogeneous ply model is meshed using 8-node linear brick, reduced integration and hourglass control C3D8R. The use of C3D8R for the mesoscale would result in some element distortion. To eliminate the element distortion, the fully integrated element C3D8 must be used for the mesoscale models. Fully integrated elements have four integration points compared to the reduced integration elements which have only one integration point at the centroid of the element. Reduced integration elements take less time to solve due to the reduced order of integration, but it might not have the capabilities to detect strains at the integration point accurately for the mesoscale model since there two material properties are defined, for example, fiber and matrix material properties. Thus, fully integrated elements are required in order to capture an accurate structure response of the mesoscale that can be comparable to the structure response of the homogeneous ply model.

Table 2.6 Number of elements generated for lamina and laminate analysis

Lamina Models	Mesoscale	2,100,000
	Homogeneous	150,000
Laminate Models	Mesoscale	1,920,000
	Homogeneous	240,000

2.3.1 Tensile Loading Simulation

A lamina and laminate structure of mesoscale and homogeneous ply models are analyzed subjected to tensile loading. For tensile loading analysis, the boundary conditions and load used are shown in Figure 2.12. The load is applied to the models using displacement control. A prescribed displacement is applied using kinematic coupling constraint. The kinematic coupling constraint is very useful in this case since there are a large number of nodes. The kinematic coupling constrains the motion of the slave nodes to the motion of a single reference point which is the master node.

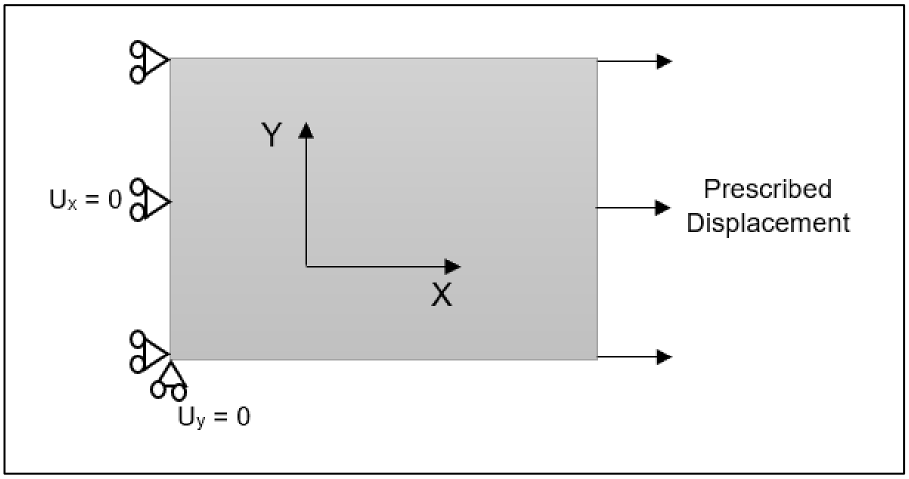

Figure 2.12 Tensile simulation load and boundary conditions

The Young's modulus E_x and Poisson ratio v_{xy} are calculated and compared between the mesoscale and homogeneous ply models. The results of the Young's modulus and Poisson's ratio are calculated using the average stress and strain as illustrated in equation (2.5). The average values of stress and strain are calculated by taking the summation of stress and strain of all elements and dividing them by the total number of elements.

$$E_x = \frac{\bar{\sigma}_x}{\bar{\varepsilon}_x} \qquad\qquad v_{xy} = -\frac{\bar{\varepsilon}_y}{\bar{\varepsilon}_x} \tag{2.5}$$

where $\bar{\sigma}_x$ is the average stress in X direction, $\bar{\varepsilon}_x$ is the average strain in X direction and $\bar{\varepsilon}_y$ is the average strain in Y direction. The results for a lamina with orientation of 0° and 45° under tensile loading are presented in Tables 2.7 and 2.8, respectively.

Table 2.7 Result for a lamina under tensile loading for tow oriented at 0 deg.

Models	E_x (GPa)	v_{xy}
Mesoscale	139.522	0.4274
Homogeneous	139.539	0.4265
% Difference	0.013	0.223

Table 2.8 Result for a lamina under tensile loading for tow oriented at 45 deg.

Models	E_x (GPa)	v_{xy}
Mesoscale	12.4703	0.2302
Homogeneous	12.3987	0.2444
% Difference	0.576	5.995

The results for a laminate with orientation of [± 45^o]$_s$ and [0^o/90^o]$_s$ under tensile loading are presented in Tables 2.9 and 2.10, respectively.

Table 2.9 Result for a laminate under tensile loading for layup of [± 45^o]$_s$

Models	E_x (GPa)	ν_{xy}
Mesoscale	18.416	0.7207
Homogeneous	17.425	0.7489
% Difference	5.531	3.834

Table 2.10 Result for a laminate under tensile loading for layup of [0^o/90^o]$_s$

Models	E_x (GPa)	ν_{xy}
Mesoscale	75.422	0.0569
Homogeneous	74.518	0.0550
% Difference	1.207	3.303

The results for tensile simulation of a lamina of mesoscale model and homogeneous ply model are in good agreement. The percentage difference of the Young's modulus E_x between the mesoscale model and the homogeneous ply model of a lamina with orientation of 0^o and 45^o are 0.013 % and 0.576 %, respectively. Also, the percentage difference of the Poisson ratio ν_{xy} between the mesoscale model and the homogeneous ply model of a lamina with orientation of 0^o and 45^o are 0.223 % and 5.995 %, respectively. However, there is a difference between the results for the laminate models of [±45^o]s and [0^o/90^o]$_s$. For [±45^o]$_s$ laminates, the percentage difference of the Young's modulus E_x and Poisson ratio ν_{xy} between mesoscale and homogeneous ply models are 5.531 % and 3.834 %, respectively. In the case of [0^o/90^o]$_s$ laminates, the percentage difference of the Young's modulus E_x and Poisson ratio v_{xy} between mesoscale and homogeneous ply models are 1.207 % and 3.303 %, respectively. This difference is because the geometry of the mesoscale models was not captured accurately; therefore, the results are under/over predicted. When the tows in the mesoscale models are oriented with orientation other than 0^o, it gets very complex to capture the tows' geometry with the use of the hexahedral solid element that is aligned with the coordinate axes. Due to the nature of the hexahedral solid element, some of the tow's elements are taken as matrix elements which lead to over/under predicting the results of the mesoscale models.

2.3.2 Transverse Loading Simulation

Mesoscale and homogeneous ply models of composite laminate are analyzed under transverse loading. Mesoscale and homogeneous laminates, with orientation of $[\pm 45^o]_s$, are developed to analyze the flexural response of the composite models. Two studies are performed. In the first study, the composite plate is analyzed under a concentrated force applied in the center of the plate. While the second study, the composite plate is analyzed under uniform distributed load. The composite plate is simply supported for both studies as shown in Figure 2.13(a). A concentrated force of 0.001 N is applied in the first study whereas a uniform distributed load of 0.01 Pa is applied in the second study as illustrated in Figure 2.13 (b) and (c), respectively.

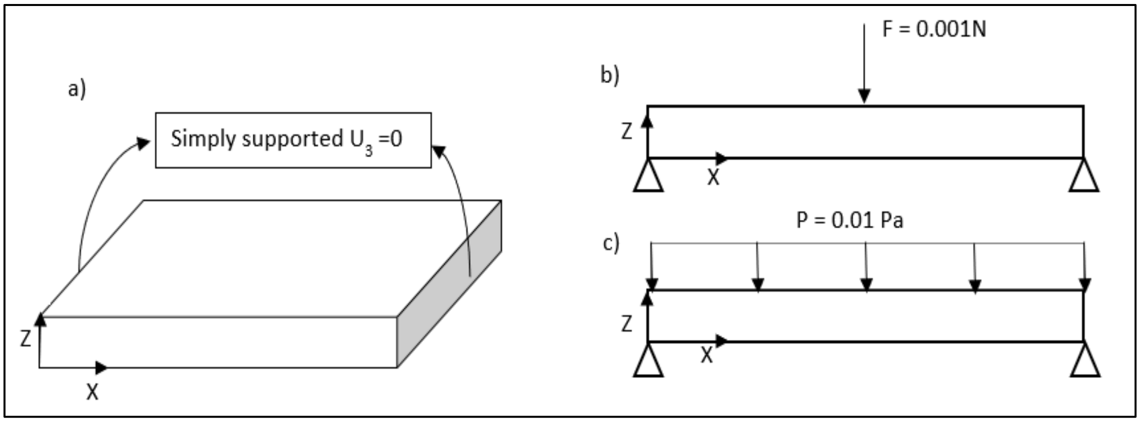

Figure 2.13 Transverse loads and boundary conditions for b) concentrated load and c) distributed load

The flexural response for the concentrated force and distributed load cases are summarized in Tables 2.11 and 2.12, respectively. The maximum deflection of the composite plates is compared. The mesoscale and homogeneous ply models correlate well in the case of the concentrated force as well as in the case of the distributed load with a percentage difference of 0.75 % and 0.086 %, respectively.

Table 2.11 Flexural response of $[\pm 45]_s$ laminate of concentrated force of 0.001 N

	Mesoscale Model	Homogenized Model
Deflection (mm)	$- 3.9949 \times 10^{-6}$ mm	$- 3.9652 \times 10^{-6}$ mm
% Difference: 0.75 %		

Table 2.12 Flexural response of $[\pm 45]_s$ laminate of distributed load of 0.01 Pa

	Mesoscale Model	Homogenized Model
Deflection (mm)	$- 4.5937 \times 10^{-3}$ mm	$- 4.5898 \times 10^{-3}$ mm
% Difference: 0.086 %		

2.3.3 Edge Bending Simulation

Mesoscale and homogeneous laminates, with orientation of $[\pm 45^o]_S$, are developed to analyze their response under concentrated force applied along an edge of the laminates. The composite laminates are simply supported and a concentrated force of 0.01 N is applied along one of the laminate edges as illustrated in Figure 2.14.

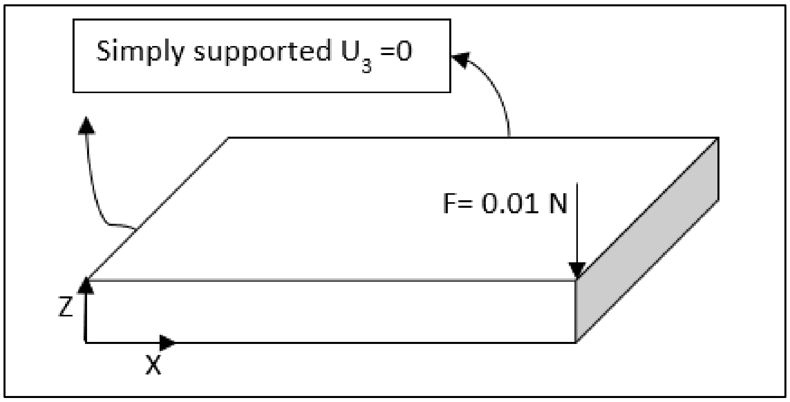

Figure 2.14 Edge Bending simulation load and boundary conditions

The structural response of the edge bending test is summarized in Table 2.13. The maximum displacement of the mesoscale and homogeneous ply models is compared. About 6% difference between the mesoscale and homogeneous ply models. The difference is due to the mesoscale tow geometries were not captured very well. Due to the nature of the voxel mesh, some of the tow's elements are taken as matrix elements in the mesoscale model which results in larger deflection in the mesoscale model compared to the homogenous model.

Table 2.13 Laminate result of edge bending simulation for layup of [± 45]s

	Mesoscale Model	Homogenized Model
Deflection (mm)	-2.84106×10^{-2}	-2.67756×10^{-2}
% Difference: 5.9 %		

2.3.4 Structural Analysis Conclusion

A preliminary finite element analysis has been performed to study the structural response of a composite lamina as well as laminates under tensile loading and flexural loading. A mesoscale model and a homogeneous ply model are used for the structural analysis of the composite lamina and laminates. For composite lamina analysis, the structural response comparison between the mesoscale models and the homogeneous ply models is in good agreement. However, there are discrepancies in the structural response of the composite laminates between the mesoscale and homogeneous ply models. The difference in the laminates analysis is due to how the tows geometries are captured in the mesoscale models. The tow elements in the $[\pm 45^{o}]_{s}$ laminate are taken as matrix elements which results in under/over predicting the structural response of the mesoscale model. For the $[0^{o}/90^{o}]_{s}$ laminate, there is no issue when it comes to capture the geometry of the tows oriented at 0^{o}, but for 90^{o} orientation, the tows require more elements (or voxels) in the X direction to capture the tows accurately.

Overall, based on the preliminary finite element analysis, it can be concluded that the mesoscale finite element model and the homogeneous finite element model generate a similar structural response. However, the mesoscale model requires a large number of elements to give a comparable structural response to the homogeneous ply model. Therefore, both models can be used in this study to generate the composite laminates for the impact and compression after impact simulations.

2.4 Modeling of the Non-Crimp Fabric Composite

NCF composite laminates are developed to analyze their behavior under impact loading and predict the compressive residual strength after impact. A mesoscale finite element model and a homogeneous finite element model are developed to assess the damage resistance and tolerance of the laminated composites. Both models are generated based on the non-crimp fabric specimen that has been investigated experimentally by McDermott (2019). The NCF specimen is fabricated with a multidirectional 24 plies and each ply consists of one tow through the thickness. The NCF model is generated to be consistent with the specimen used in the experiment. The modeling parameters for the mesoscale model such as the tow width, tow spacing, tow height and ply thickness are obtained based on experimental investigation as discussed in Section 2.2.1. Since the mesoscale model has tow geometries and matrix geometries, it provides the ability to evaluate the fiber and matrix damage separately for the impact analysis. The response of the impact and compression after impact of the mesoscale and homogeneous ply models is used to be compared with experimental data obtained from McDermott (2019).

2.4.1 Mesoscale Model

A finite element mesoscale model is generated to investigate the behavior of the model subjected to impact loading and predict the compressive residual strength after impact. As previously mentioned, the finite element mesoscale model is developed where the model captures the individual constituents of the composite (i.e., the tows and matrix). This modeling approach helps to evaluate the damage during impact and after impact events in more detail such that a separate investigation of the fiber and matrix failure. The modeling parameters for the mesoscale model are listed in Table 2.1. The mesoscale model is generated as a multidirectional symmetric NCF laminate with 24 layers. The NCF laminate schedule is shown in Table 2.14. Four plies with orientation of -45°, 45°, 0° and 90° are generated separately in TexGen with one tow through the thickness. Each ply is generated with 64 in-plane tows and one tow through the thickness. The four plies are imported into ABAQUS for further assembly of the composite mesoscale laminate. The mesoscale model dimensions are 150.72 mm x 100 mm x 4.464 mm. The impregnated tow elastic properties and epoxy matrix properties used for the mesoscale model are listed in Tables 2.3 and 2.4, respectively.

Table 2.14 The laminate schedule [-45/45/0/90/0/±45/03/90/45]s of the non-crimp fabric

Midplane	
12	45
11	90
10	0
9	0
8	0
7	-45
6	45
5	0
4	90
3	0
2	45
1	-45

A Python script is developed for the mesoscale generation and processed in TexGen. As mentioned, the plies are generated with one tow through the thickness. Four plies are developed with different tow's orientation 0°, 45°, -45° and 90°. For simplicity, the script generates the plies and exports an ABAQUS input file with the ply's information. The element type used is C3D8 solid element. All four plies are imported into ABAQUS with their proper tow's orientation and mesh. The assembly of the mesoscale model can be done through TexGen but to implement the interlaminar failure criteria between the plies, it is easier to assemble the model and implement the failure criteria in ABAQUS. A sample mesoscale ply generated in TexGen with the tows oriented 45° is shown in Figure 2.15. A Python script of the ply generation is attached in Appendix A.

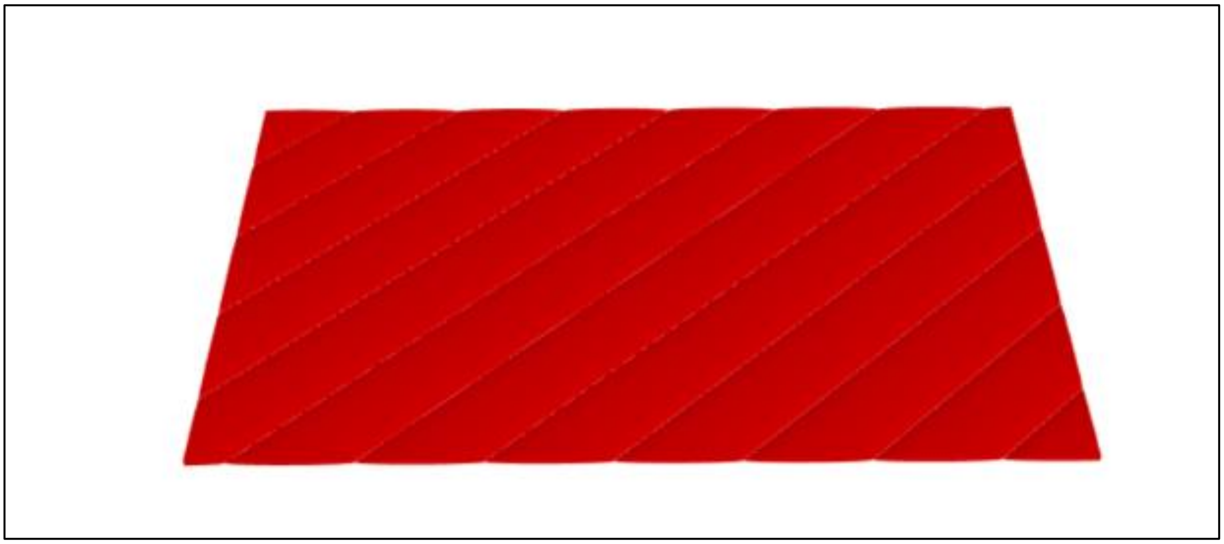

Figure 2.15 A mesoscale model generated in TexGen with the tows oriented 45°.

2.4.2 Homogeneous ply model

A finite element homogeneous ply model is developed in ABAQUS to analyze the behavior of the model under impact loading and predict the compressive strength of the laminate after impact. The finite element homogeneous ply model is generated wherein the heterogeneous plies are replaced by equivalent homogeneous anisotropic plies. The plies of the homogeneous model are created using 3D deformable solid elements. Plies with orientation of 45°, -45°, 0° and 90° are created separately and then used to assemble the laminate based on the composite layup in

Table 2.14. The homogeneous ply model dimensions are 150 mm x 100 mm x 4.464 mm. The material orientation is defined using the available tool in ABAQUS. A local coordinate system is defined for each ply. Then, each ply is assigned a material orientation based on the local coordinate system of the ply. The homogenized properties listed in Table 2.5 are used for this model.

2.4.3 Mesh Generation

The composite laminates for the impact and compression after impact events are meshed using the voxel mesh technique. The mesoscale model is meshed within TexGen. The element type used for the mesoscale is the 8-node brick element C3D8. This element type is a general-purpose linear brick element and it is fully integrated. However, the homogeneous ply model is meshed within ABAQUS with fully integrated 8-node brick element C3D8. The fully integrated elements are used for the homogeneous ply model with fewer number of elements compared to the mesoscale model. Based upon the structural response analysis presented in Section 2.3, the mesoscale model requires high mesh density (large number of elements) to capture the tows geometries accurately. The total number of elements generated for the mesoscale model as well as the homogeneous ply model is listed in Table 2.15.

Table 2. 15 Number of elements generated for the mesoscale and homogeneous ply models

Model	Element Type	Number of Elements
Homogeneous ply model	C3D8	460,800
Mesoscale Model	C3D8	1,920,000

2.4.4 Experiment Comparison

In this section, the homogenized properties are validated with experimental data by predicting the laminate Young's modulus E_x and E_y. This validation is performed to ensure that the homogenized properties estimate the laminate modulus close to the experimental values. The experiment is presented in McDermott (2019). The Young's modulus E_x and E_y are obtained experimentally by performing tension tests. The experimental results are the average value of seven to eight specimens. The specimens are loaded in tension in the 0^o and 90^o orientation. To predict the Young's modulus E_x and E_y, the extensional stiffness matrix [A] was computed using the classical laminate theory. The inverse of [A], the compliance matrix [a], is calculated to predict the Young's modulus E_x and E_y using equation (2.6).

$$E_x = \frac{1}{a_{11}H} \qquad\qquad E_y = \frac{1}{a_{22}H} \tag{2.6}$$

where a_{11} and a_{22} are the extensional terms and H is the laminate thickness. Table 2.16 summarizes the results of both experimental and predicted results of the laminate moduli. As shown in the results, there is no significant difference between the experimental and predicted results. A 0.71 % and a 2.48 % difference for E_x and E_y, respectively. The predicted and experimental results correlate well which demonstrate confidence in the composite laminate model.

Table 2.16 Experiment and prediction comparison of laminate moduli

V_f (%)	**Laminate Moduli (GPa)**					
	E_x			E_y		
	Experimental	Predicted	Diff. (%)	Experimental	Predicted	Diff. (%)
57.2 – Expt. 57.09 –Pred.	72.2	72.511	0.71	40.7	41.72	2.48

Chapter 3 Damage Analysis during Low Velocity Impact Loading of Multidirectional Fiber-Reinforced Laminate

3.1 Introduction

Unidirectional fiber-reinforced composites are being increasingly used in automobiles, aerospace, and many other industries due to their higher structural strength, low weight and impact tolerance compared to those of metallic parts. One of the objectives of this research is to perform computational simulations of carbon fiber-reinforced composites subjected to low velocity impact loading using finite element analysis. Two finite element models are developed to analyze the behavior of composite laminates made of non-crimp fabric under impact loading. The finite element models are developed as symmetric laminates of 24 multidirectional plies. The first model is a homogeneous ply finite element model which is generated within the finite element package ABAQUS. The second model is a mesoscale finite element model where its plies are generated using textile generation software called TexGen. The mesoscale plies are imported into ABAQUS for the mesoscale laminate assembly. The modeling details of the non-crimp fabric models are presented in Chapter 2. The impact simulations of the homogeneous ply and mesoscale models are setup and performed using ABAQUS/Explicit.

The 3D Hashin failure criteria is used to evaluate the intralaminar damage initiation of the composite laminates during impact event. The Hashin failure criteria has four failure modes/indicators. Two modes are for fiber tension and compression failure initiation and the other two modes are for matrix tension and compression failure initiation. In addition, a damage evolution law is adopted to determine the damage variables for each failure mode. These damage variables are used to modify or degrade the elastic properties based on the induced damage mode.

Additionally, the interlaminar failure is evaluated using a surface-based cohesive behavior. This approach implements cohesive contact behavior between the plies to predict delamination. The damage initiation is evaluated using the quadratic stress criterion. A damage evolution law is implemented to describe the rate at which the cohesive stiffness is degraded once the corresponding initiation criterion is reached. Mixed mode failure criterion based upon energies is used for interlaminar damage propagation.

The proposed progressive intralaminar damage models are implemented in ABAQUS using a Fortran user defined subroutine. This subroutine checks for failure initiation at every integration point using the Hashin failure criteria and computes the damage variables using the exponential law. It then returns the damage variables to ABAQUS using the field variable tool for material properties assignment. A look up table is defined in ABAQUS input file to relate the field variables to the original elastic material properties as well as the degraded material properties. The impact results of both homogeneous ply and mesoscale models are compared with each other and validated with experimental data. All experimental data used to validate the finite element models presented in this chapter are obtained from McDermott (2019).

This chapter is organized as follows, Section 3.2 describes the explicit finite element simulation algorithm, and Section 3.3 describes the intralaminar damage models. Section 3.4 summarizes the modeling of delamination using cohesive behavior. Section 3.5 contains an outline of the implementation of the Fortran user subroutine and its interaction with ABAQUS. The material model validation using ABAQUS subroutine is summarized in Section 3.6. Sections 3.7 and 3.8 summarize the impact simulations with damage followed by the results of the impact simulations section, respectively.

3.2 Explicit Finite Element Simulation

Impact simulations can be performed using ABAQUS/Implicit and ABAQUS/Explicit. In this thesis, ABAQUS/Explicit is used to evaluate the finite element models under impact loading. ABAQUS/Explicit is a finite element analysis product that is applicable to analyze many types of problems such as short duration dynamic, nonlinear, quasi-static analyses and many more. ABAQUS/Explicit has the ability to handle nonlinear behavior efficiently, which makes it a perfect candidate for the present study. Some of the advantages of using ABAQUS/Explicit in this study compared to ABAQUS/Implicit are as follows:

- It has been designed to solve highly discontinuous and high-speed dynamics problems.
- It has a robust contact algorithm that does not require additional degrees of freedom.
- It does not require large disk space for analyzing large problems.

ABAQUS/Explicit uses an explicit method that integrates through time. The explicit time integration used is the central difference method. The equations of motion are integrated through time. When the solver is initiated, it solves the discretized equation of motion (3.1) to obtain the nodal acceleration for each time increment (ABAQUS, 2017).

$$M\ddot{u} = P - I \tag{3.1}$$

where *M* is the nodal mass matrix, $\ddot{u}$ is the nodal acceleration, P is the external force applied and *I* is the internal element force.

Nodal velocities are calculated using the nodal accelerations. Nodal accelerations are integrated through time using the central difference approach. The change in velocity is calculated by assuming that the acceleration is constant. The velocity at the middle of the current increment is obtained using the acceleration and the velocity at the middle of the previous increment using equation (3.2) (ABAQUS, 2017).

$$\dot{u}|_{(t+\frac{\Delta t}{2})} = \dot{u}|_{(t-\frac{\Delta t}{2})} + \frac{\Delta t|_{(t+\Delta t)} + \Delta t|_{(t)}}{2}\, \ddot{u}|_{(t)} \tag{3.2}$$

Similarly, the nodal displacements are obtained by integrating the nodal velocities using equation (3.3).

$$u|_{(t+\Delta t)} = u|_{(t)} + \Delta t|_{(t+\Delta t)}\, \dot{u}|_{(t+\frac{\Delta t}{2})} \tag{3.3}$$

To obtain accurate results, sufficiently small-time increments must be used to have nearly constant accelerations. Since a small-time increment is used, a large number of increments is required to finish the analysis. However, each increment is computationally inexpensive since the equations are not solved at the same time. The element strain increments are computed from the strain rate. The computed strain increment makes it possible to compute the element stresses by applying the material constitutive relationships (ABAQUS, 2017).

The process described is performed for each time increment. When all the above stated steps are applied for the current increment, the process gets repeated for the next increment by setting a new time for the next increment (ABAQUS, 2017).

3.2.1 Impactor Modeling

The hemispherical impactor is modeled in ABAQUS as a 3D discrete rigid body. The impactor is modeled with a diameter of 16 mm and a spherical tip shape to be consistent with the experiment setup. It is meshed with linear quadrilateral elements of type R3D4 and linear triangular elements of type R3D3 with a total of 11,232 elements.

3.2.2 Material Definition

The material system used for the impact simulation study is Hexcel® 12K IM7 carbon fibers and Cycom® PR-520 toughened epoxy matrix. The mesoscale model is assigned the material properties of the impregnated tow elastic properties listed in Table 2.3 and matrix properties listed in Table 2.4. The material properties used for the homogeneous ply model are the effective elastic properties listed in Table 2.5, which are found based on the convergence study presented in Chapter 2.

The density cannot be assigned for the impactor since it is modeled as a rigid body. Instead, an inertia is assigned to it to account for the total drop weight. For the impact simulations, the impactor is assigned a mass corresponding to the impact energies and impact velocity.

Due to the lack of the material properties of the current investigated composite, the composite material strengths are used from previous study investigated by Warren et al. (2016). Warren used the same material system IM7/PR-520 for his study and he investigated a uni-ply panel of IM7 carbon fiber manufactured with 24K tows and injected with PR-520 epoxy resin. The fiber volume fraction of the panel is 61.4 %. The panel was evaluated experimentally to compute the material properties by loading the panel in tension, compression and shear directions. The material strengths obtained experimentally are listed in Table 3.1.

Table 3. 1 Uni-ply material strength properties

Load	Symbol	Strength (MPa)
Tensile strengths	X_T	1750
	Y_T	69.6
Compressive strengths	X_C	665
	Y_C	177
Shear strength	S	106

Mechanical properties validation is performed using computational simulations and compared to experimental investigation presented by McDermott (2019). The NCF model is generated in ABAQUS to validate the material strengths properties listed in Table 3.1. The FE model is a multidirectional NCF composite and consists of 24 layers. The layup schedule of the NCF composite is shown in Table 2.14. The FE model is evaluated in tensile loading oriented parallel to, perpendicular to and biased to (oriented at 45°) the fiber direction. For tensile testing, the FE model is generated with 3D solid elements and dimensions of 100 mm x 25 mm x 4.464 mm. It is meshed with C3D8 elements and assigned the homogenized properties listed in Table 2.5. The experiment is carried out with ASTM D3039. Seven to eight specimens were characterized experimentally at each load orientation 0°, 45° and 90°. The specimens tested experimentally of IM7 carbon fiber are manufactured with 12K tows and injected with PR-520 epoxy resin. The results of the tensile loading are presented in Figures 3.1a-c which shows the correlation between the finite element simulations and experimental results. The computational model predicted the mechanical behavior of the tensile tests very well. A summary of the tensile tests results is presented in Table 3.2. The experimental results presented in Table 3.2 are the average value of multiple specimens. It can be concluded that the tensile strength properties presented in Table 3.1 are valid to be used in this study with knowing that the tow size is different between Warren's work and this current study. The other strength properties for the compression and shear are assumed to be valid as well.

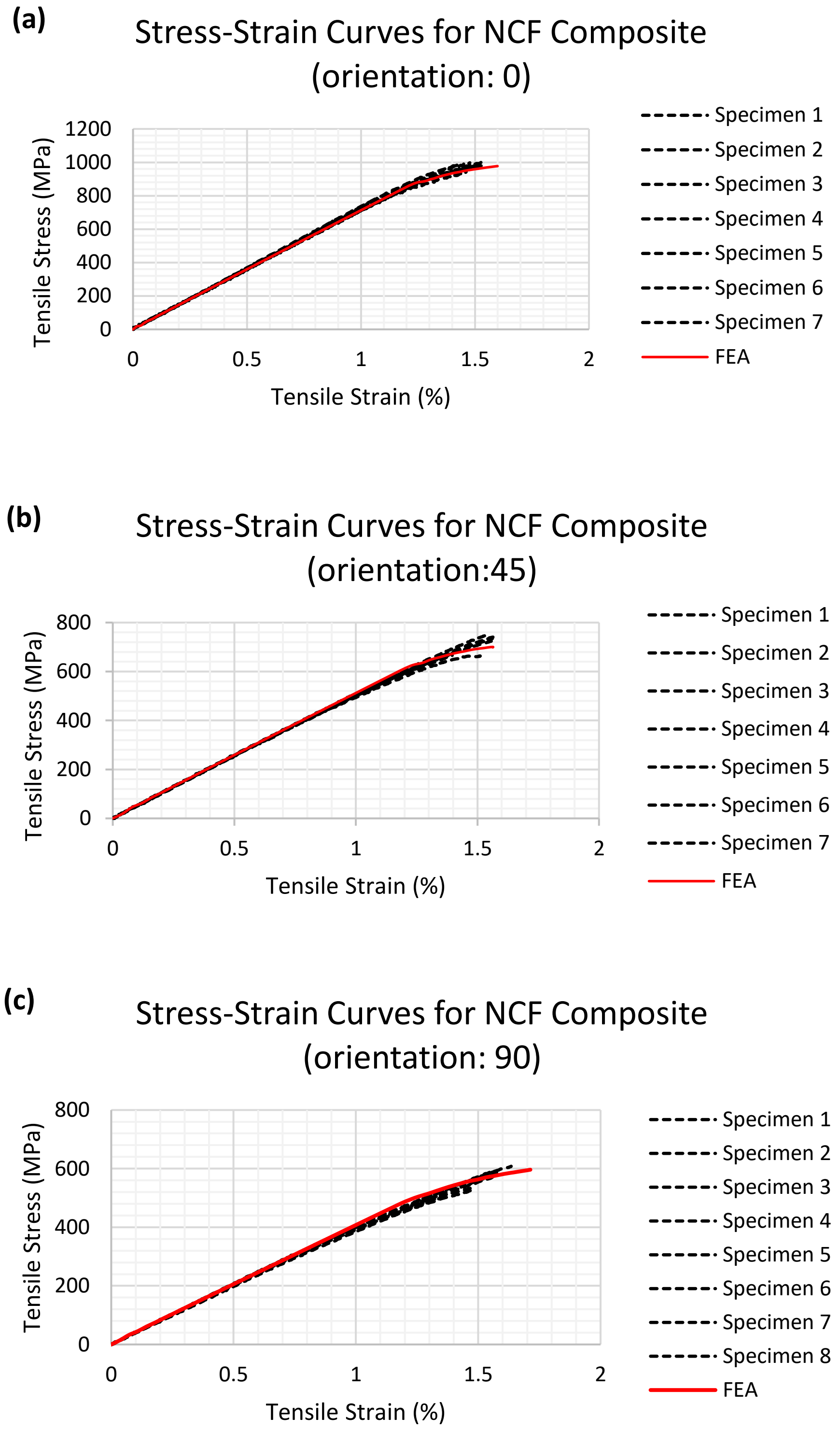

Figure 3. 1 Results of tensile loading of the NCF composites: (a) load orientation 0° (b) load orientation 45° (c) load orientation 90°

Table 3. 2 Summary of tensile test results

Load Orientation		Ultimate Strength (MPa)	Young's Modulus (GPa)
0°	Experiment	983	72.2
	FEA prediction	885	72
45°	Experiment	709	51.8
	FEA prediction	626.8	51.5
90°	Experiment	566	40.7
	FEA prediction	505.2	41.3

3.2.3 Analysis Step

The analysis step is created in the step module in ABAQUS, the procedure of the step is chosen to be Dynamic Explicit with a step time in the range of 5 to 9 milliseconds for the impact simulations. The geometric nonlinearity is toggled on in the basic tab. Automatic time incrementation is used with the stable increment estimator is selected to be global with a time scaling factor of 1. Since the density and the Young's modulus are known, the critical parameter for the stable time increment is the dimension of the smallest element. The composite laminates are modeled to have the smallest element dimension which limits the stable time increment for the whole model/assembly of the impact setup. Maximum time increment is kept to its default setting, unlimited. Mass scaling is not applied for any region of the model and the linear and quadratic bulk viscosity parameters are set to default values of 0.06 and 1.2, respectively.

3.2.4 Boundary Conditions and Load Applied

The boundary conditions used for the finite element laminated composite are a representation of the experimental setup used in the impact test. The drop weight test is carried out experimentally using Airbus Industries AITM 1-0010 standard. In order to represent the experiment setup, the laminated composite is simply supported in the entire inner perimeter, 75 mm x 125 mm, such that the displacement component $U_3=0$. Additionally, two constraints are included to prevent the laminate from translating and rotating in the other directions. The boundary conditions applied on the composite laminate for the impact simulations are shown in Figure 3.2.

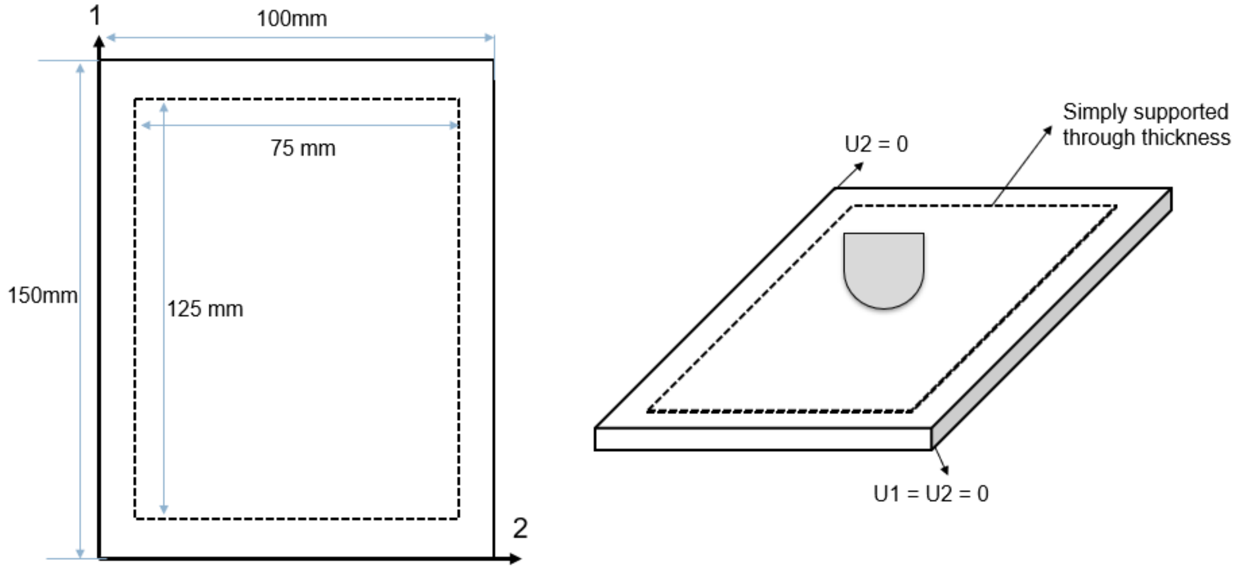

Figure 3. 2 The boundary conditions applied on the composite laminate for the impact simulation

The 16 mm hemispherical rigid impactor is modeled with a reference point at the impactor tip to be able to apply boundary conditions and load. The impactor's reference point is fixed in all directions except the impact translation direction. Additionally, an impact velocity is applied to the impactor in which this initial velocity accounts for the drop height of the impactor. The initial velocity is applied to the reference point of the impactor through the predefined field option in ABAQUS. Figure 3.3 illustrates the load and boundary conditions used for the impactor.

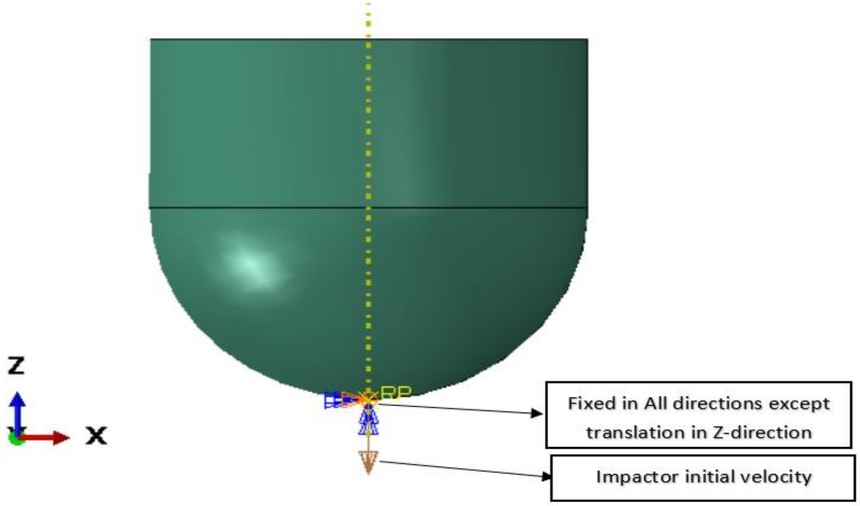

Figure 3. 3 Impactor's boundary conditions and load used for the impact simulations

3.2.5 Contact Definition

The general contact algorithm for ABAQUS/Explicit analysis is used for the impact simulations. ABAQUS/Explicit is a very robust FEA package with a proven contact algorithm. This contact method goes through the finite element model and defines contact between any two or more solid parts. The contact domain is set to “All with self” with the use of global contact properties. This contact algorithm definition is a necessity in order to prevent penetration between the parts that will be in contact. The contact properties definition is created in the contact property tool in ABAQUS. A mechanical tangential behavior is defined, and the penalty friction formulation is used with a small friction coefficient of 0.3. The value of the friction coefficient is used for the contact between the impactor and the top surface of the laminate.

Also, a normal behavior is used for the contact definition, with the ”Hard” contact as the pressure-over closure, which means that the friction is applied only when two surfaces are in contact. In addition, the constraint enforcement method is set to default and separation is allowed after contact.

3.3 Intralaminar Damage Model

In this study, the three-dimensional Hashin failure criterion is adopted to determine the damage initiation of the composite laminate during impact. It has been used successfully in numerous FEA studies of composite materials to evaluate failure initiation. The Hashin failure criteria is developed for unidirectional composites and derived based on the quadratic five stress invariants presented in Hashin et al. (1980). The stress invariants are presented in equation (3.4).

$$I_1 = \sigma_{11} \qquad I_2 = \sigma_{22} + \sigma_{33} \qquad I_3 = \sigma_{23}^2 - \sigma_{22}\sigma_{33} \tag{3.4}$$

$$I_4 = \sigma_{12}^2 + \sigma_{13}^2 \qquad I_5 = 2\sigma_{12}\sigma_{23}\sigma_{13} - \sigma_{22}\sigma_{13}^2 - \sigma_{33}\sigma_{12}^2$$

The failure criteria include four individual failure modes, fiber tension and compression modes and matrix tension and compression modes. The failure indicator variables are calculated to evaluate the failure initiation for each failure mode as seen in equations (3.5a-d). As can be seen in the Hashin failure indicator’s equations, the theory accounts for the interaction between shear and normal stress.

Fiber tension failure mode (FTF) ($\sigma_{11} > 0$)

$$f_1 = \left(\frac{\sigma_{11}}{X_T}\right)^2 + \frac{\sigma_{12}^2+\sigma_{13}^2}{S_L^2} \tag{3.5a}$$

Fiber compression failure mode (FCF) ($\sigma_{11} < 0$)

$$f_2 = \left(\frac{\sigma_{11}}{X_C}\right)^2 \tag{3.5b}$$

Matrix tension failure mode (MTF) ($\sigma_{22} + \sigma_{33} > 0$)

$$f_3 = \frac{1}{Y_T^2}(\sigma_{22} + \sigma_{33})^2 + \frac{1}{S_T^2}(\sigma_{23}^2 - \sigma_{22}\sigma_{33}) + \frac{\sigma_{12}^2+\sigma_{13}^2}{S_L^2} \tag{3.5c}$$

Matrix compression failure mode (MCF) ($\sigma_{22} + \sigma_{33} < 0$)

$$f_4 = \frac{1}{Y_C}\left[\left(\frac{Y_C}{2S_T}\right)^2 - 1\right](\sigma_{22} + \sigma_{33}) + \frac{1}{4S_T^2}(\sigma_{22} + \sigma_{33})^2 + \frac{1}{S_T^2}(\sigma_{23}^2 - \sigma_{22}\sigma_{33}) + \frac{\sigma_{12}^2+\sigma_{13}^2}{S_L^2} \tag{3.5d}$$

Where, f_i is the Hashin failure indicator for each failure mode. σ_{ij} are the stress components in the material coordinate system, X_T and X_C are the axial tensile and compressive strength, respectively. Y_T and Y_C are the transverse tensile and compressive strength, respectively and S_L and S_T are the axial shear strength and transverse shear strength, respectively. The strength values required for the failure initiation calculation used in equations (3.5a-d) are obtained from experimental investigation and presented in Table 3.1.

3.3.1 Damage Evolution

A damage evolution law is used in this study to evaluate the intralaminar failure propagation for each failure mode, i.e. fiber tension or compression failure mode and matrix tension or compression failure mode. The exponential damage evolution law is adopted from Warren et al. (2016) to calculate the damage variable for each failure mode. The damage evolution law utilizes equation (3.6) to calculate the damage variable.

$$d(f_i) = D_{i\,max}\left[1 - exp\left(-\frac{f_i^m}{m\,e}\right)\right] \tag{3.6}$$

Where D_{max} is the maximum degradation variable, f_i is the Hashin failure indicator, m is the material response parameter and e is the base of the natural logarithm. Equation (3.6) can be used to enforce different damage evolution law including instant failure or more of ductile failure. Using a small value of the material response m would generate a ductile response of the material damage. The damage becomes an instantaneous failure when m approaches an infinite value. Equation (3.7) describes the instantaneous failure using the exponential damage evolution law. The damage variable is computed for any value given by the Hashin failure indicator f.

$$d(f) = \begin{cases} 0, & if\ f = 0 \\ D_{max}, & if\ f > 0 \end{cases} \tag{3.7}$$

A plot of equation (3.6) is shown in Figure 3.4 with varying Hashin failure indicator f from 0 to 2.4 and specifying D_{max} to be 0.8. The plot of equation (3.6) is evaluated at different values of material response m. A value of 150 is used for the material response parameter m for the impact simulations throughout this study.

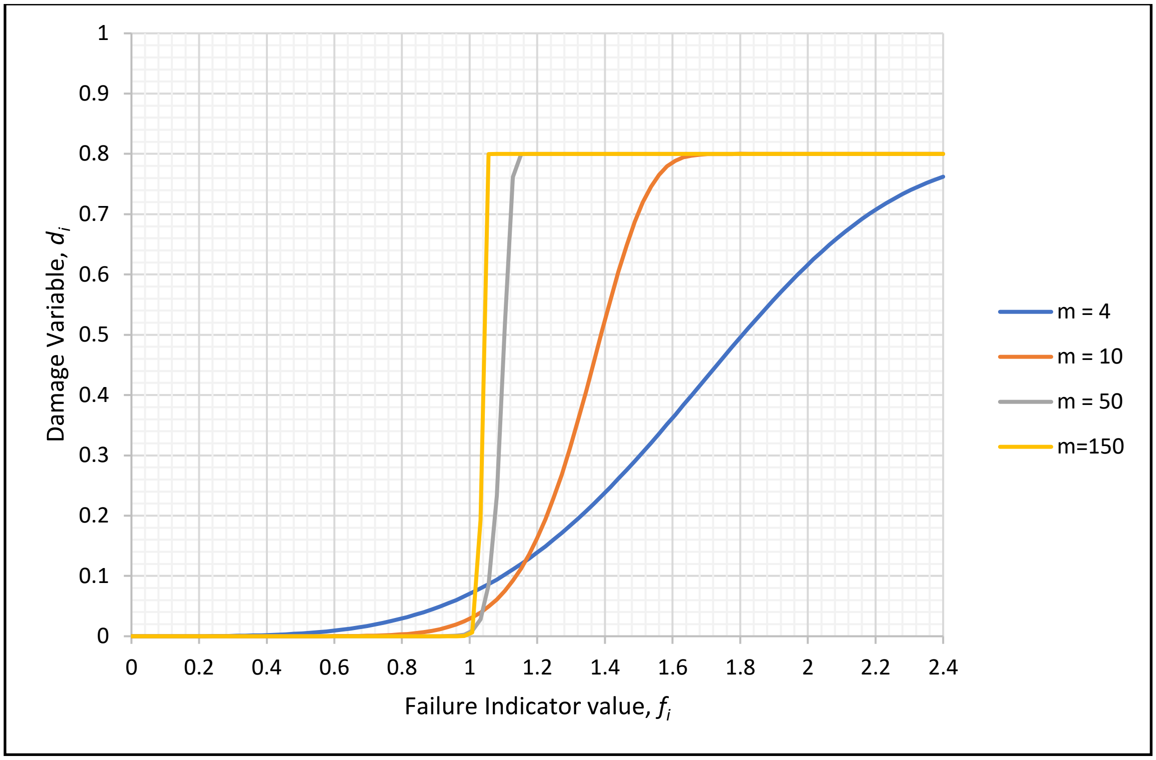

Figure 3. 4 Damage variable value d_i as a function of the failure indicator f_i using the exponential damage evolution law with $Dmax = 0.8$ evaluated at various values of the material parameter m

The maximum damage variable must be specified for each Hashin failure mode. In this study, the maximum damage variables for the tensile and compression damage modes in both fiber (D_{1max}) and transverse (D_{2max}) directions are listed in equations (3.8) and (3.9). The elastic material properties are degraded based on the maximum damage variable for each mode such that when $D_{max} = 0.93$, the elastic properties are degraded 7% of their original values. A property degradation rule, which shows the Hashin failure modes along with the property that is being degraded, is presented in Table 3.3.

$$D_{1\,max} = \begin{cases} 0.93, & if\ tension \\ 0.80, & if\ compression \end{cases} \tag{3.8}$$

$$D_{2\,max} = \begin{cases} 0.85, & if\ tension \\ 0.85, & if\ compression \end{cases} \tag{3.9}$$

Table 3. 3 Properties degradation rule

Elastic Property	Hashin Failure Modes			
	FTF	**FCF**	**MTF**	**MCF**
E_1	X	X	-	-
E_2	-	-	X	X
E_3	-	-	X	X
v_{12}	-	-	-	-
v_{13}	-	-	-	-
v_{23}	-	-	-	-
G_{12}	X	-	X	X
G_{13}	X	-	X	X
G_{23}	-	-	X	X

3.4 Interlaminar Damage model

Delamination is a major failure mode for composites under impact loading and it has been investigated by researchers both in experimental tests and numerical simulations. Sun et al. (2014), Liu et al. (2018) and other researchers have used and proposed methods in the literature to model delamination failure such as applying the three-dimensional delamination failure criteria in the composite laminates. Applying the three-dimensional delamination failure criteria in composites might lead to the inaccurate prediction of the interface properties because of the complexity of delamination modeling. Therefore, for this study, implementing a cohesive behavior between the interfaces becomes a better option to predict delamination between the plies. ABAQUS has the capability to model cohesive behavior for solid elements without the need to use subroutines to implement interlaminar failure.

3.4.1 Cohesive Behavior Modeling

The interlaminar failure implementation is based upon the surface-based cohesive behavior in ABAQUS. This method is intended for problems where the interface thickness is negligibly small. Delamination is captured by using a traction-separation relationship. This approach is convenient to model the cohesive behavior as an interaction without the need to model cohesive elements. A quadratic nominal stress criterion is adopted to evaluate the initiation of delamination:

$$\left\{\frac{\langle t_n \rangle}{t_n^o}\right\}^2 + \left\{\frac{t_s}{t_s^o}\right\}^2 + \left\{\frac{t_t}{t_t^o}\right\}^2 = 1 \tag{3.10}$$

Where t_n^o, $t_{s,}^o$ and t_t^o represent the interface normal and first and second shear strengths, respectively. The symbol $\langle\ \rangle$ used in equation (3.10) represents the Macaulay bracket. The Macaulay bracket signifies a purely compressive displacement, or a purely compressive stress state does not initiate damage.

Once the quadratic nominal stress criterion is met, the delamination initiation phase is finished, and the delamination begins to propagate. The mixed-mode criterion is used to simulate the delamination propagation. This criterion is based on the fracture energy release rate and fracture toughness method. The mixed mode criterion proposed by Benzeggagh and Kenane et al. (1996) (BK criterion) is able to account for the variation of fracture toughness as a function of mode ratio in the epoxy composites. The BK criterion assumes the first and second shear directions are the same, i.e., $G_{IIc} = G_{IIIc}$. The BK criterion is used in this study to evaluate the delamination propagation, which its expression is as follows:

$$G_{IC} + (G_{IIC} - G_{IC})\left(\frac{G_{shear}}{G_T}\right)^{\eta} = G_{TC}$$

$$G_{shear} = G_{II} + G_{III} \qquad G_T = G_I + G_{shear} \tag{3.11}$$

Where G_{TC} is the mixed-mode fracture toughness under combined mode loading and G_T is the total fracture energy release rate. G_{Ic} and G_{IIc} denote the interfacial Mode I and II critical fracture energy corresponding to G_I and G_{II} respectively, and η is the cohesive property parameter. The BK criterion is activated once the total fracture energy release rate G_T is equal to or greater than the mixed-mode fracture toughness G_{TC}. When the ratio $\frac{G_{shear}}{G_T}$ in equation (3.11) is zero, the interlaminar failure becomes a mode I dominated. However, when the ratio $\frac{G_{shear}}{G_T}$ is one, the interlaminar failure becomes mode II dominated. In this research, the parameter η *is* assumed; however, the parameter η should be determined using a least square fit from a set of experimental data. A plot of equation (3.11) is shown in Figure 3.5 with varying the value of the cohesive property parameter, η.

The material properties used for the cohesive modeling are listed in Table 3.4. The strength properties of the interface are assumed to be the epoxy matrix strength properties of PR-520. The fracture energy of Mode I is found experimentally and presented in McDermott (2019). However, the fracture energies of Mode II and III are assumed to be $2.4*G_{Ic}$.

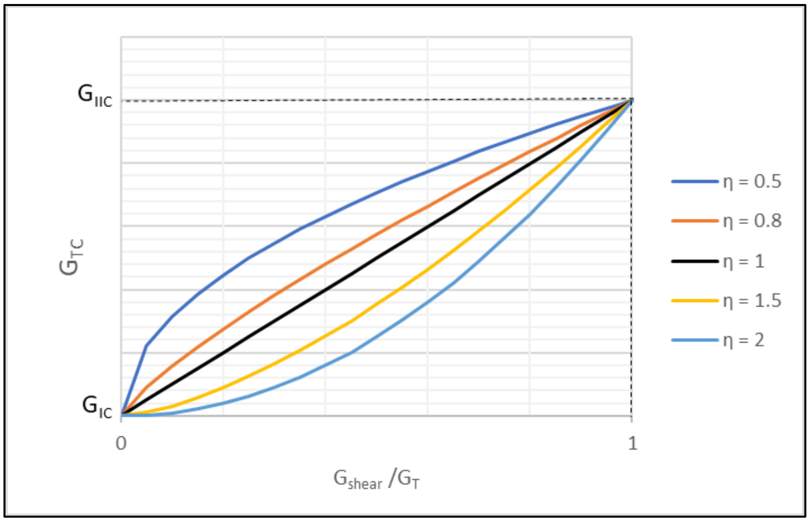

Figure 3. 5 Plot of the BK criterion with varying the value of the cohesive property parameter

Table 3. 4 Cohesive parameter used in this study

Property	*Value*
t_n^o (MPa)	82.1
t_s^o (MPa)	61.4
t_t^o (MPa)	61.4
G_{IC} (mJ/mm^2)	1.097
$G_{IIC} = G_{IIIc}$ (mJ/mm^2)	2.633
η	2.0

3.5 ABAQUS User Subroutine

A Fortran user subroutine (VUSDFLD) is developed to evaluate the intralaminar damage of the composite using the proposed Hashin failure criteria with the exponential damage evolution law. The user subroutine receives stresses from ABAQUS at every integration point and uses them to calculate the Hashin failure indicators for each failure mode. Next, the damage variable *d* for each mode is computed based on the exponential damage evolution law. The damage variables d_i are returned to ABAQUS using the field variables tool. A look up table is defined in ABAQUS input file to relate the field variables to the elastic material properties. Based on the returned field variable, the appropriate material properties are assigned to the FE model. A flowchart of the implementation of the progressive damage model corresponding to the VUSDFLD user subroutine in ABAQUS is shown in Figure 3.6. A copy of the VUSDFLD Fortran subroutine is attached in Appendix B.

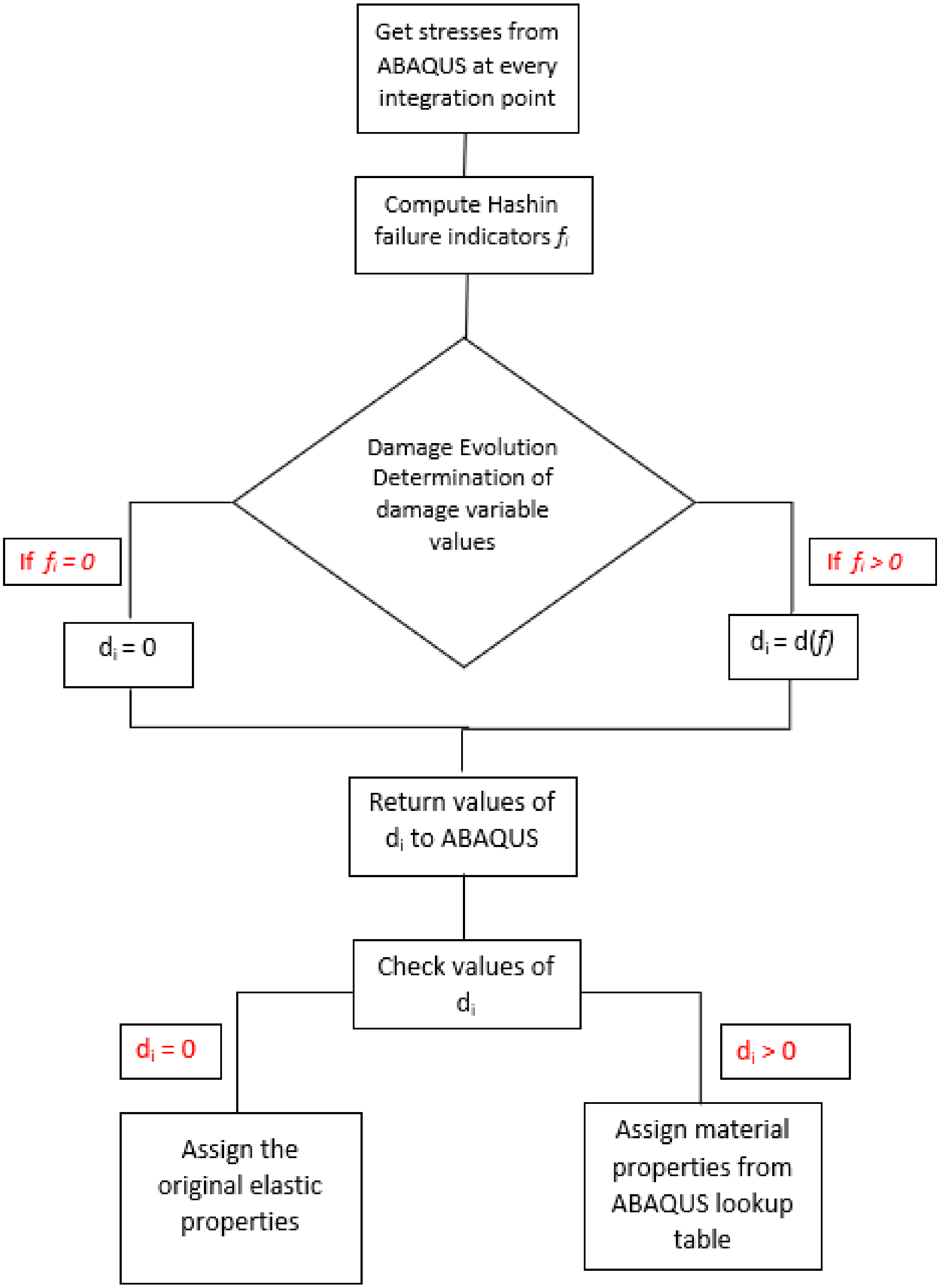

Figure 3. 6 Flowchart of the implementation of the progressive damage model corresponding to the user subroutine

3.6 Validation of Material Model

In this section, the model validation of a single element and coupon tests is presented. This validation is performed to ensure that the proposed progressive damage model produces physically realistic behavior while reducing the level of complexity. The simulation models consisted of loading for each failure mode individually and tested to verify the model response and the damage progression. The simulations are performed with the parameter response *m* of the intralaminar damage is set to be 100. The material properties used for the validation of the material model are the homogenized properties and they are listed in Table 2.5, and the material strengths are listed in Table 3.1.

For the single element simulations, an eight-node linear brick with dimensions of 2 mm x 2 mm x 2 mm is modeled in ABAQUS and loaded under displacement control in each direction with boundary conditions as shown in Figure 3.7. The stress responses of the solid element are evaluated in the fiber, transverse and shear directions.

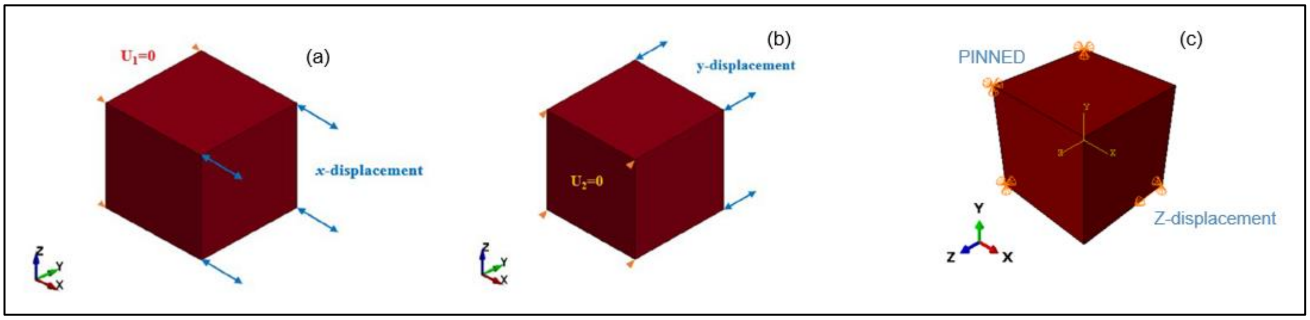

Figure 3. 7 Boundary conditions and loads of single element simulations: a) Fiber direction. b) Transverse direction. c) Shear direction.

For the simulation of the coupon tests, the FEA model is a rectangular plate generated in ABAQUS with dimensions of 70 mm x 15 mm x 2 mm. The plate models are generated with hexahedral solid elements and loaded in all directions, fiber, transverse and shear direction. The plate is meshed as C3D8 with 280 elements. The boundary conditions and loads applied for each test are shown in Figure 3.8.

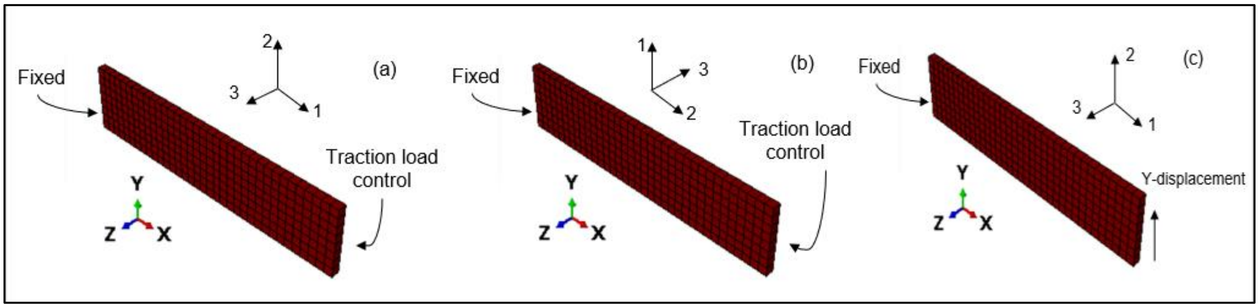

Figure 3. 8 Boundary conditions and loads of coupon simulations: a) Fiber direction. b) Transverse direction. c) Shear direction.

3.6.1 Results of Model Validation

The simulation results of the single element tests loaded in tension, compression and shear directions are illustrated in Figures 3.9. In the case of the tension in fiber direction, tension in transverse direction and shear direction, the stresses were gradually increased until the material reached its failure strength. Also, for the compression fiber and transverse directions, the magnitude of the compressive stresses is gradually increased until the material reaches its failure strength. Once the material failure occurs, the elastic properties get degraded based on the degradation rule presented in Table 3.3.

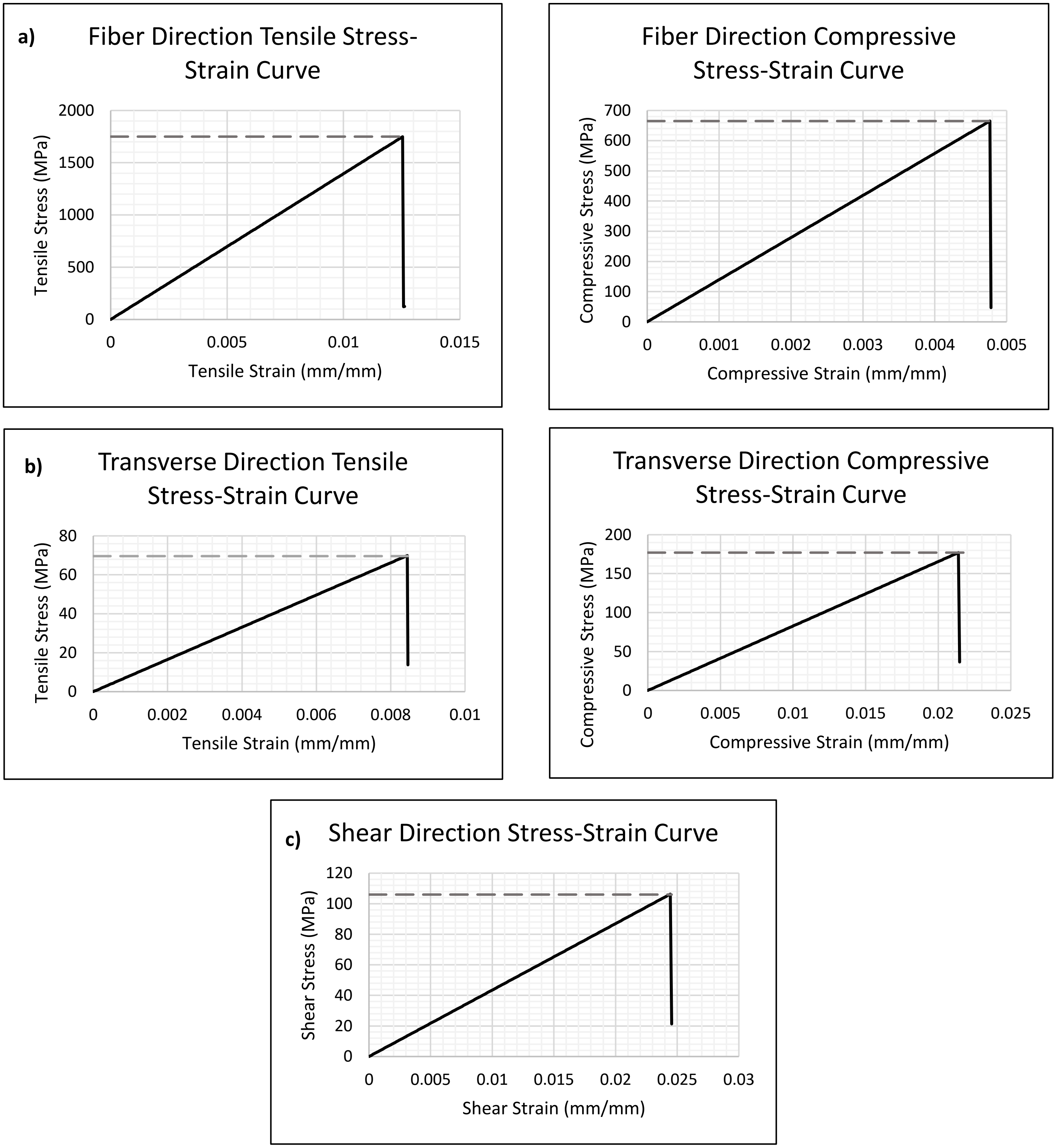

a) Fiber Direction Tensile Stress-Strain Curve

Fiber Direction Compressive Stress-Strain Curve

b) Transverse Direction Tensile Stress-Strain Curve

Transverse Direction Compressive Stress-Strain Curve

c) Shear Direction Stress-Strain Curve

Figure 3. 9 Results of single element test loaded in (a) fiber direction (b) transverse direction and (c) shear direction

The results of the coupon simulations are illustrated in Figures 3.10 for tension and compression in the fiber direction, tension and compression in the transverse direction and the shear direction. The coupon plate is loaded in tension, compression and shear directions like the single element simulations. The coupon simulations are performed to ensure that the developed ABAQUS user subroutine evaluates the intralaminar damage for larger models with several numbers of elements as well as to ensure the mechanical response of the coupons is accurate. The results of the coupon simulations are as expected. The coupons fail once the material reaches its failure strength. It could be concluded that the response of the progressive failure model is consistent with the expected mechanical behavior of the composite. Also, it could be concluded that ABAQUS user subroutine can be used for practical FEA simulations.

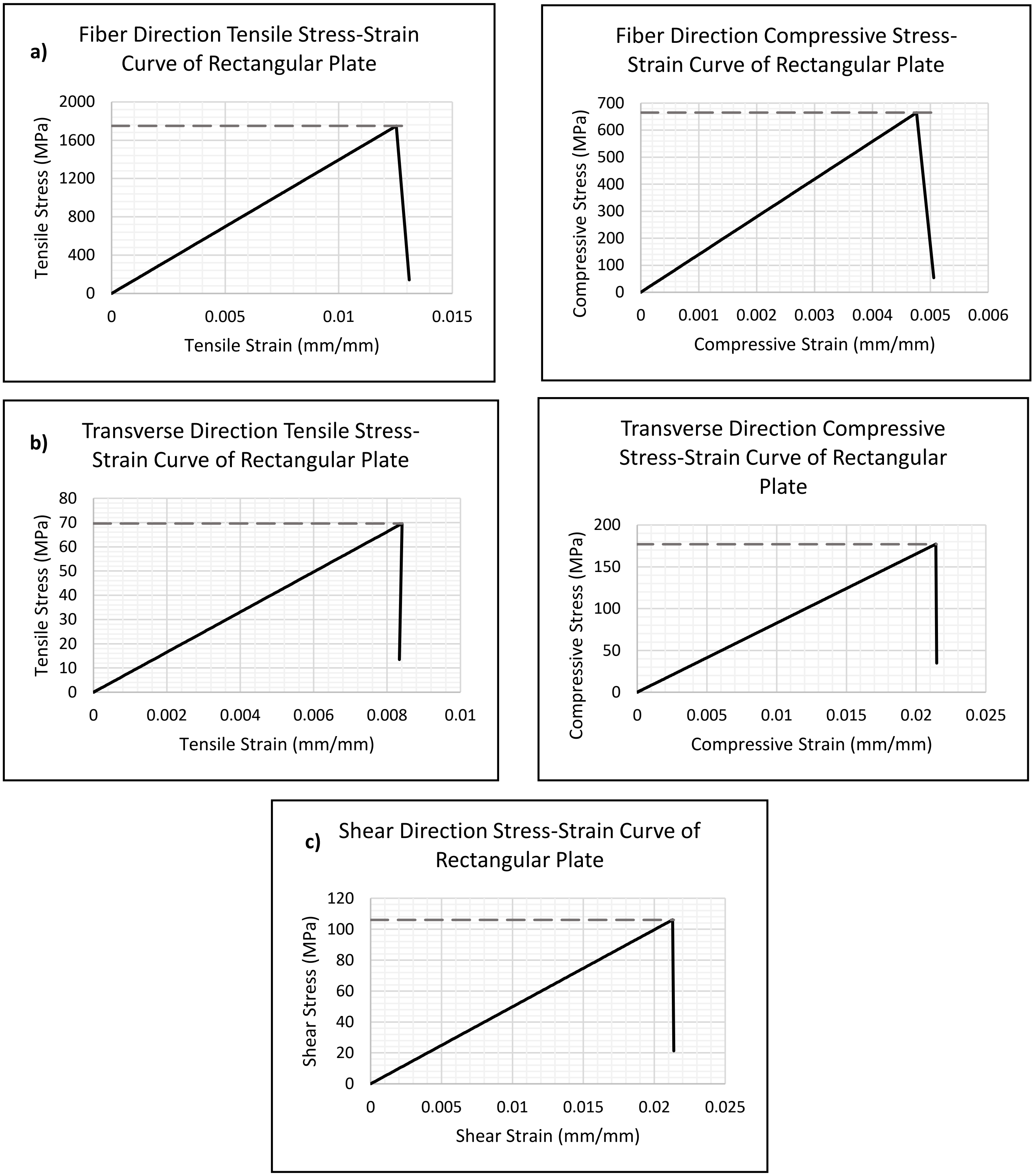

a) Fiber Direction Tensile Stress-Strain Curve of Rectangular Plate

Fiber Direction Compressive Stress-Strain Curve of Rectangular Plate

b) Transverse Direction Tensile Stress-Strain Curve of Rectangular Plate

Transverse Direction Compressive Stress-Strain Curve of Rectangular Plate

c) Shear Direction Stress-Strain Curve of Rectangular Plate

Figure 3. 10 Results of coupon plate test loaded in (a) fiber direction (b) transverse direction and (c) shear direction

3.7 Impact Simulations with Damage

The FEA simulations are performed to investigate the NCF laminated composites under low velocity impact loading. The NCF laminates are impacted at three different energy levels, 30 J, 50 J and 60 J. The parameters used for the impact simulations are listed in Table 3.5. The finite element homogeneous ply model is subjected to the three different energy levels. While the finite element mesoscale model is investigated under one energy level, 30 J. The numerical impact response of the homogeneous ply model and the mesoscale model are presented and validated with experimental data.

Table 3. 5 Impact parameters used in simulations

Impact energy (J)	Drop mass (kg)	Impact velocity (m/s)
30	5.498	3.303
50	9.498	3.245
60	10.498	3.381

3.8 Impact Results and Discussion

The low velocity impact simulations are performed using homogeneous ply model and mesoscale model. This section presents a characterization of the impact simulations in terms of the force histories, absorbed energy and damage area for low and high energy impacts.

3.8.1 Contact Force and Displacement Histories and Absorbed Energy

3.8.1.1 Low Energy Impact

For 30 J impact, the numerical force-time and force-displacement curves for the homogeneous laminate are shown in Figure 3.11(a-b). The homogeneous laminate exhibits a similar impact response with experiment, characterized by an increase in the contact force during the loading phase with no evidence of significant damage such as drop in the contact force or high frequency oscillations (Belingardi et al., 2002). Figure 3.11(a) shows the force-time curve, the predicted peak force of the homogeneous ply model correlates very well with experiment with a difference of 2.76 %. The irregular oscillating pattern is captured very well compared to experiment which indicates that no significant damage had occurred at 30 J impact. The oscillations in the force-time curve for the homogeneous ply model are mostly due to the plate vibration. The force-displacement curves of the homogeneous ply model and experiment are shown in Figure 3.11(b). The maximum deflection is under predicted by 3.09 % compared to experiment as shown in Figure 3.11(c). The transverse displacement (deflection) of the top and bottom surfaces of the homogeneous ply model is plotted against the in-plane X-coordinate as shown in Figure 3.12(a). Additionally, a contour plot of the top surface and through the thickness (X-Z plane) of the homogeneous ply model is shown in Figures 3.12(b) and (c), respectively, which illustrate the deflection of the laminate at the peak load. It can be observed from Figure 3.11 that the rebound response of the homogeneous ply model is slower than experiment. The total impact duration of the homogeneous ply model is about 4.93 ms while the experiment is about 4.5 ms. The slower rebound might be due to the accuracy of capturing the material behavior such as the model indentation damage mechanism. Also, it may be caused by the friction between the impactor and the top surface as well as the friction between the delaminated plies.

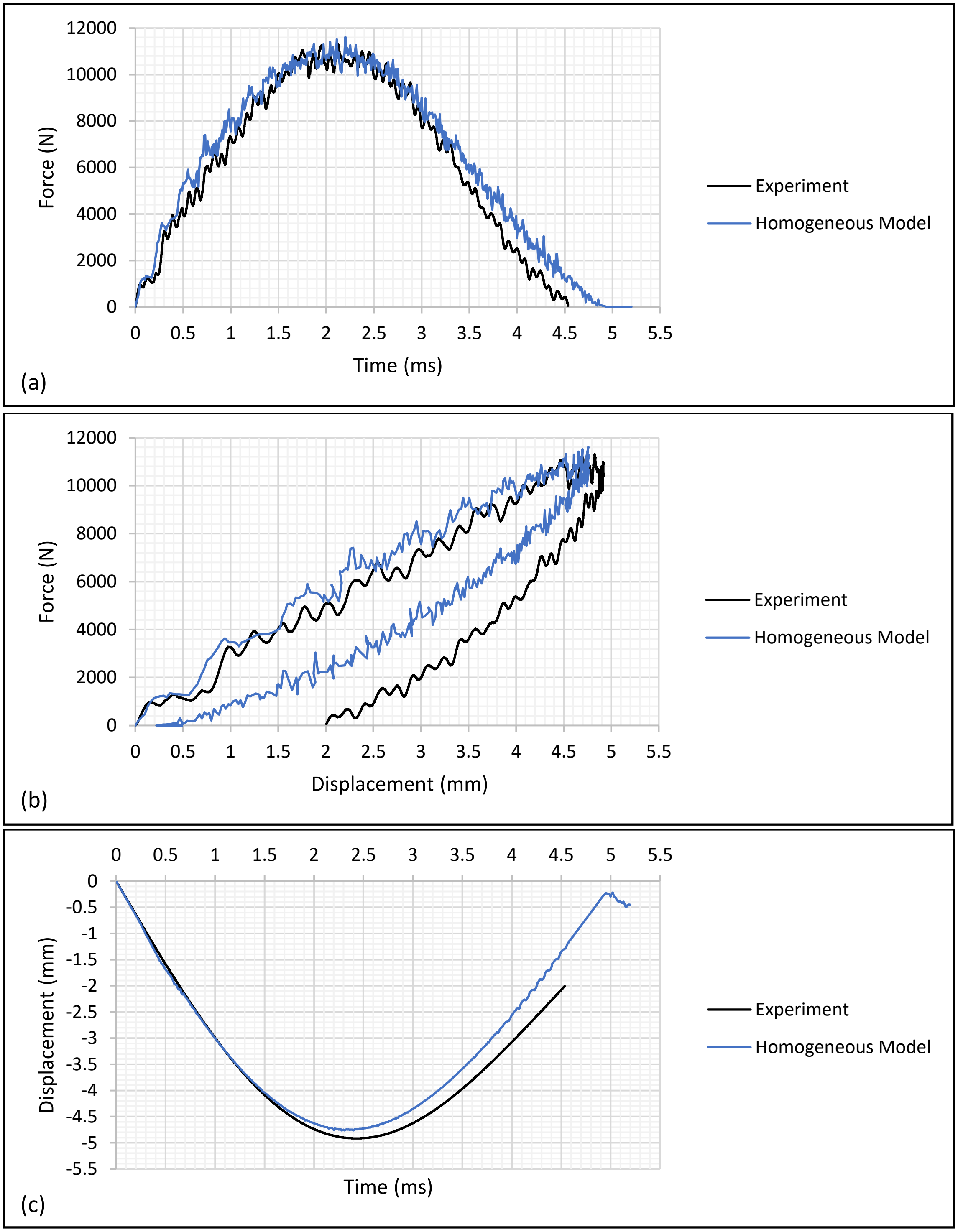

Figure 3. 11 Numerical results for the homogeneous laminate impacted at 30 J impact: (a) force-time (b) force-displacement and (c) deflection-time curves

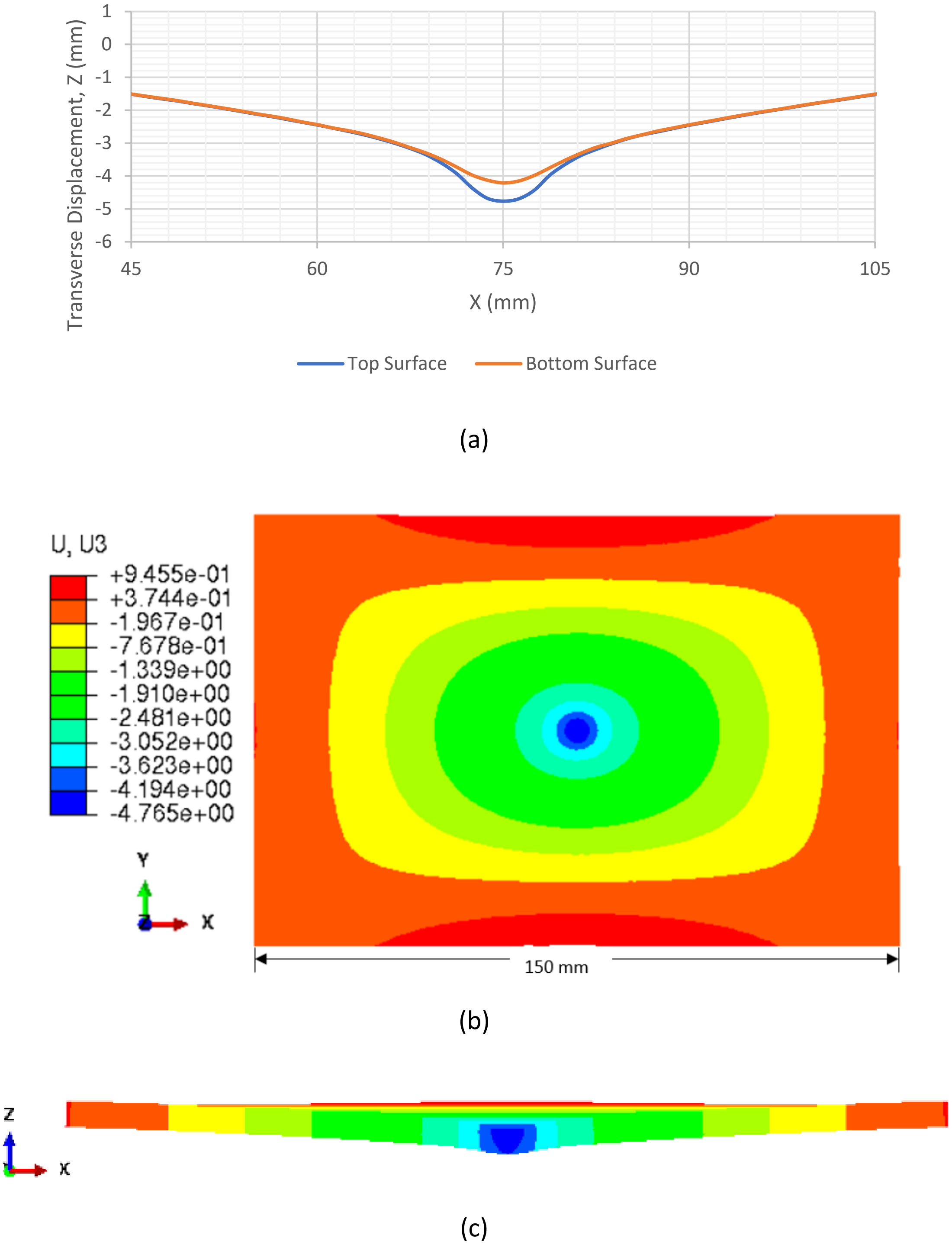

Figure 3. 12 Out of plane displacement of the homogeneous ply model: (a) plot of the transverse displacement of the top and bottom surfaces against the X-coordinate, (b) X-Y plane contour plot of the top surface and (c) X-Z plane contour plot.

The numerical force-time and force-displacement curves of the mesoscale model are illustrated in Figures 3.13(a) and 3.13(b), respectively and compared with the impact response of the homogeneous ply model and experiment. The mesoscale model has predicted a larger peak force than experiment by 21.51 %. The maximum deflection of the mesoscale model is lower than experiment by 14.38 % as shown in Figure 3.13(c). The numerical impact results of the mesoscale model differ from the results obtained from experiment. The difference is because the mesoscale model requires mesh refinement in order to improve the accuracy of the results. Based on the structural analysis presented in Section 2.3, the mesoscale model requires a large number of elements to capture the geometry of the tows accurately and predict the structural behavior more accurately. The current model is generated with 1,920,000 C3D8 elements and increasing the number of elements of the mesoscale model would be computationally expensive.

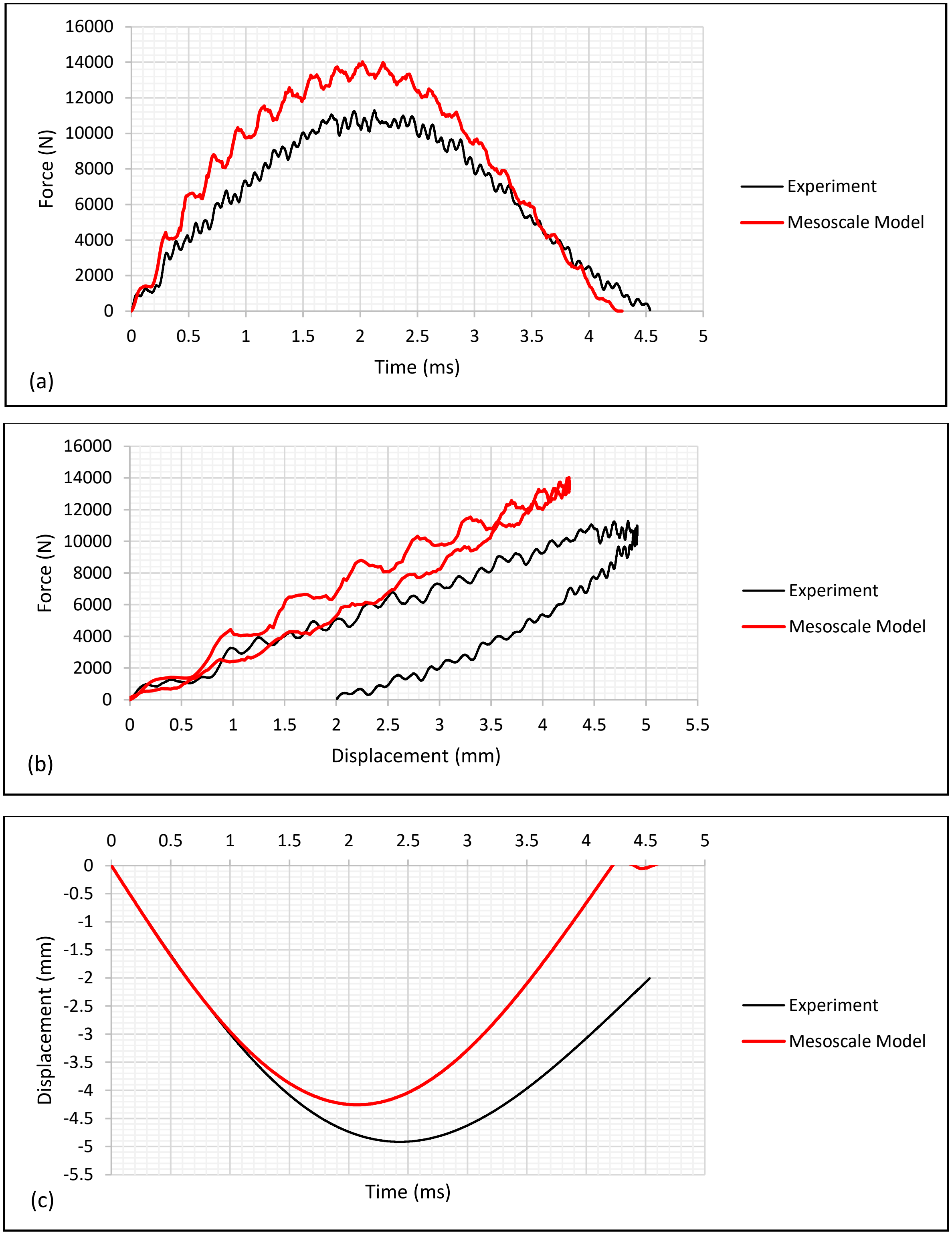

Figure 3. 13 Numerical results for the mesoscale laminate impacted at 30 J impact: (a) force-time, (b) force-displacement and (c) deflection-time curves

It is observed from the force-displacement curve of the homogeneous ply model for the low energy impact, 30 J shown in Figure 3.12(b), the homogeneous ply model does not have the capability to accurately predict the residual displacement. This is because the permanent deformation and the tow entanglement are not captured after impact as observed in the experiment. In addition, it is observed that the predicted force-displacement curve is almost enclosed by the experimental curve; this observation concludes that the predicted absorbed energies are lower than the experimental absorbed energy. However, the force-displacement curve of the mesoscale model is under predicted as shown in Figure 3.13(b). As previously stated, the mesoscale model is generated with low mesh density which results in under predicting the impact response. The plots of the absorbed energies are shown in Figure 3.14. As can be seen from the absorbed energies plots, the homogeneous ply model curve compares very well with experiment during the initial impact until the impactor reaches nearly zero velocity. The residual absorbed energies get released from the impact damage during the rebound of the impactor. Also, the under prediction of the absorbed energies is due to not capturing the residual strain effect in the model (Lin et al., 2019). Table 3.6 summarizes the peak force, maximum deflection and absorbed energy of the low energy impact simulations compared to experiment.

Table 3. 6 Summary of the peak force, maximum deflection and absorbed energy for the low impact energy

Impact Energy (J)/Model		Peak Force (N)	Maximum Deflection (mm)	Absorbed Energy (J)
30	Experiment	11300.74	4.92	17.6
	Homogeneous ply model	11617.20 (2.76%)	4.77 (3.09%)	10.69 (48.85%)
	Mesoscale Model	14024.80 (21.51%)	4.26 (14.38%)	4.72 (115.41%)

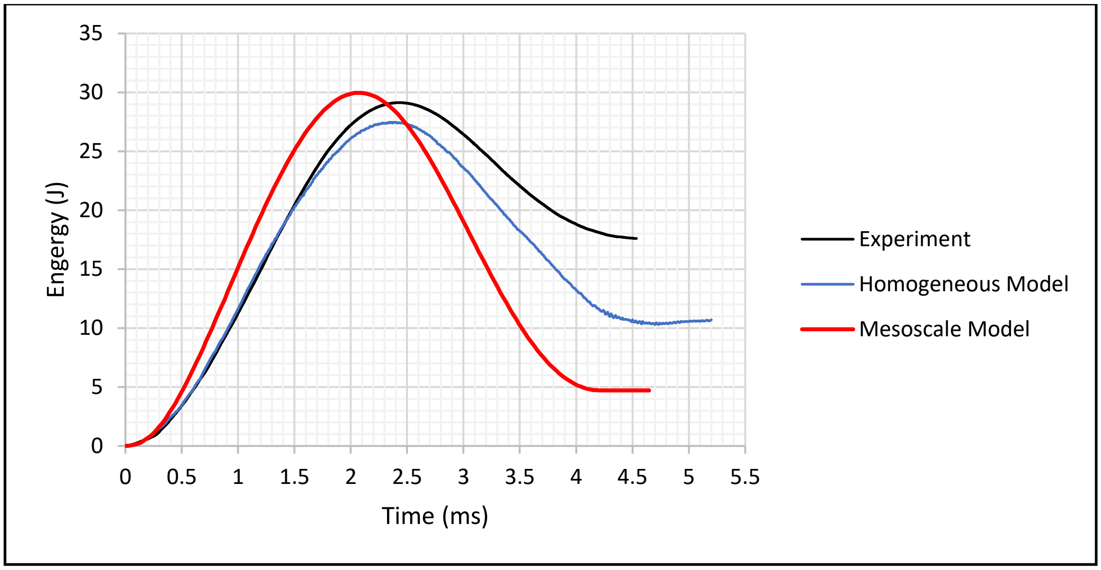

Figure 3. 14 Absorbed energy vs. time curves for low impact energy, 30 J

3.8.1.2 High Energy Impact

For 50 J and 60 J impacts, the numerical and experimental force-time and force-displacement curves are illustrated in Figure 3.15(a-b) and Figure 3.16(a-b), respectively. For the 50 J and 60 J impacts, the peak force of the homogeneous laminate is higher than experiment by 6.57 % and 19.59 %, respectively. The maximum deflection is however under predicted for both levels of impact energy as shown in Figures 3.15(c) and 3.16(c). Significant failure is observed experimentally when the contact force has reached about 14,000 N for 50 J and higher. From Figures 3.15(a) and 3.16(a), it is observed from the experimental curves that a force drop occurs especially in the 60 J impact when the contact force has reached about 14,000 N. Once the force drop occurs, the contact force has remained relatively constant in the range of 8000 – 12000 N until the impactor has reached zero velocity. However, the predicted contact force of the homogeneous ply model increases until the velocity of the impactor has reached zero. The reason for the drop in the contact force is because a significant diagonal tows failure has been observed experimentally in the back face (breaching of the back face) of the laminate. However, the impact simulation using the homogeneous ply model has not captured the tows failure mechanism in the back face of the model. This might be due to the modeling approach used to generate the homogeneous ply model. The homogeneous plies are modeled as smeared plies (no tow and matrix geometries involved). In addition, the interlaminar fracture energies of modes I, II and III are another factor that influence the accuracy of the predicted results. As mentioned previously in Section 3.2.2, the value of the interlaminar fracture energy for mode I G_{IC} is obtained from experiment. However, the values of the interlaminar fracture energy for modes II G_{IIC} and III G_{IIIC} are assumed to be $2.4*G_{IC}$. From the literature, it is found that an accurate prediction of an impact response is improved when an accurate value of the fracture properties is used (Tan and Falzon et al., 2016). The exact value of mode II fracture energy is required to accurately predict the impact response as well as the delamination/damage area (Francesconi and Aymerich et al., 2017).

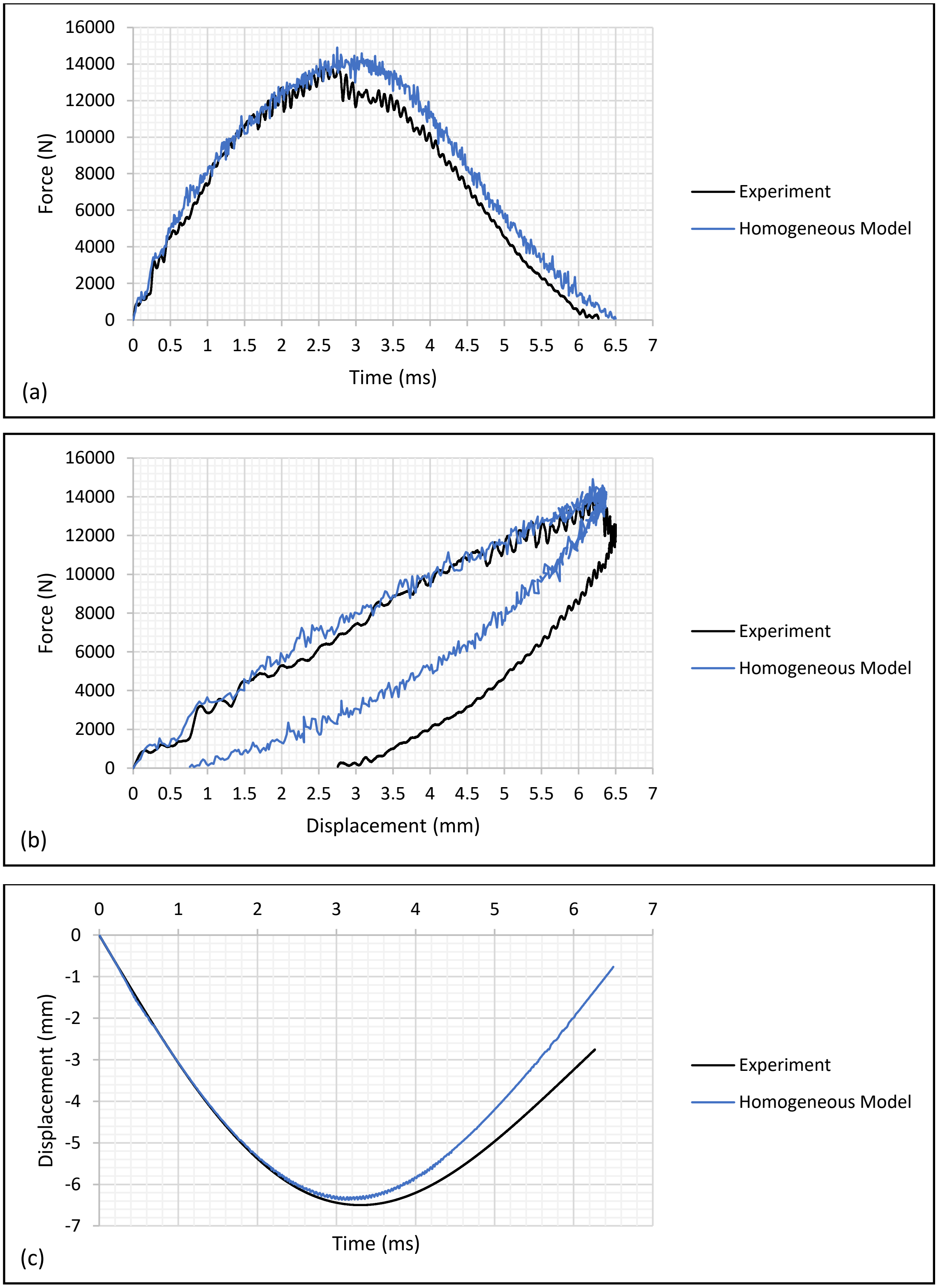

Figure 3. 15 Numerical results for homogeneous ply models impacted at 50 J impact: (a) force-time, (b) force-displacement and (c) deflection-time curves

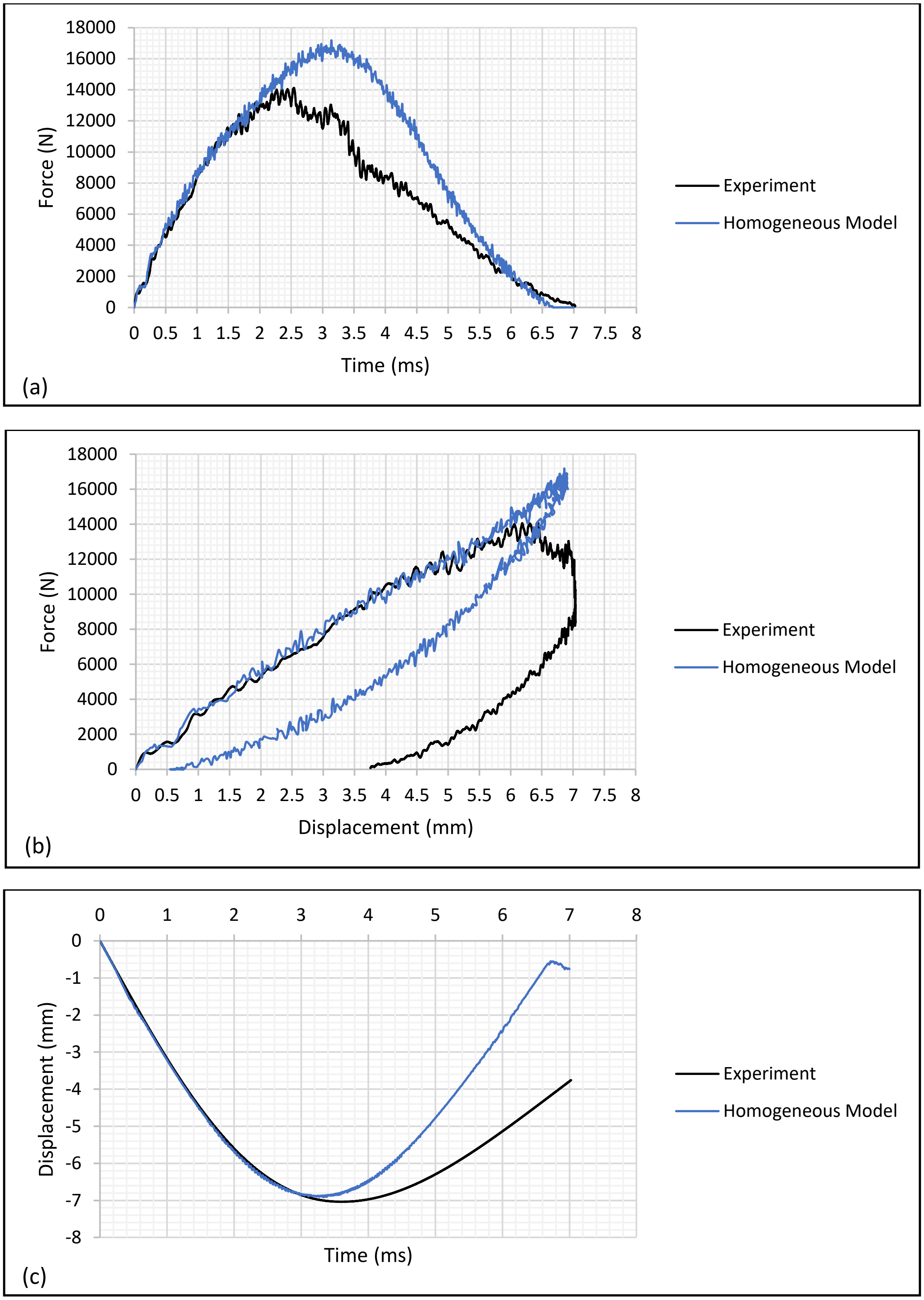

Figure 3. 16 Numerical results for homogeneous ply model impacted at 60 J impact: (a) force-time, (b) force-displacement and (c) deflection-time curves

It is observed from the force-displacement curves of the simulations for the high impact energy, 50 J and 60 J shown in Figures 3.15(b) and 3.16(b), the homogeneous ply model does not have the capability to accurately predict the residual displacement. This is because the permanent deformation and the tow entanglement are not captured after impact as observed in the experiment. In addition, it is observed that the predicted force-displacement curves are almost enclosed by the experimental curves; this observation concludes that the predicted absorbed energies are lower than the experimental absorbed energies. The plots of the absorbed energies are shown in Figure 3.17(a-b). As can be seen from the absorbed energies plots, the curves compare very well with experiment during the initial impact until the impactor reaches nearly zero velocity. The residual absorbed energies get released from the impact damage during the rebound of the impactor. Also, the under prediction of the absorbed energies is due to not capturing the residual strain effect in the model (Lin et al., 2019). As the impact energy increases, a significant discrepancy is found in terms of the peak force and the absorbed energy. Table 3.7 summarizes the peak force, maximum deflection and absorbed energy for high impact energy simulations compared to experiment.

Table 3. 7 Summary of the peak force, maximum deflection and absorbed energy for high impact energy

Impact Energy (J)/Model		Peak Force (N)	Maximum Deflection (mm)	Absorbed Energy (J)
50	Experiment	13959.73	6.49	33.86
	Homogeneous ply model	14907.70 (6.57%)	6.37 (1.87%)	20.41 (49.57%)
60	Experiment	14119.70	7.04	48.33
	Homogeneous ply model	17186.30 (19.59%)	6.92 (1.72%)	21.95 (75.07%)

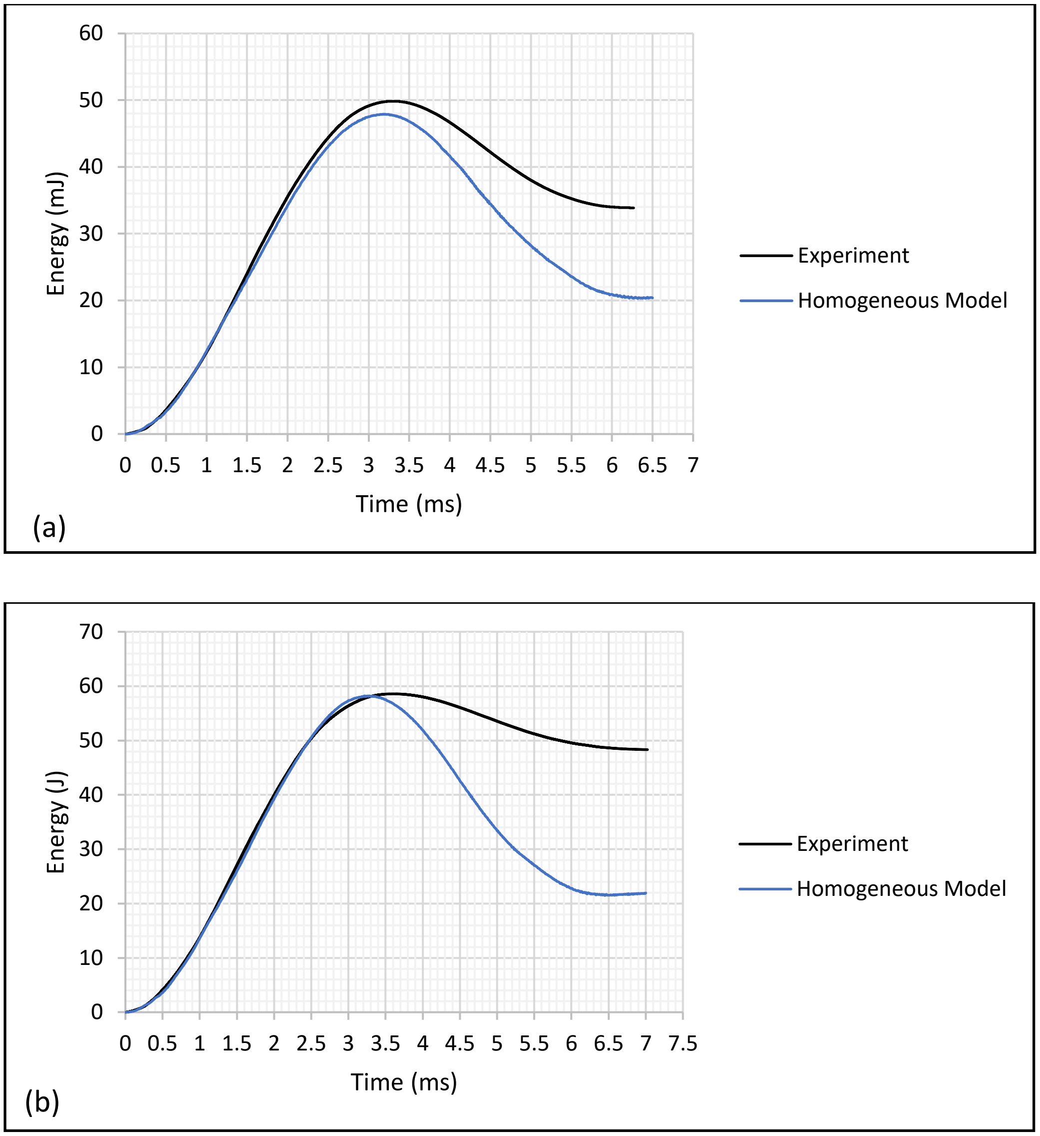

Figure 3. 17 Absorbed energies vs. time curves for high impact energy (a) 50 J impact and (b) 60 J impact

3.8.2 Impact Damage Area Prediction

As previously mentioned, there is a good agreement between the predicted results of the homogeneous ply model and experiment for the 30 J impact. While for higher levels of impact energies, 50 J and 60 J, there are some discrepancies in the numerical results of the homogeneous ply model compared to experimental results. The predicted damage envelopes compared to the experimental ultrasonic C-scan are shown in Figure 3.18(a-c). For 30 J, 50 J and 60 J impact, the predicted damage area is mostly an elliptical shape and as the incident impact energy increases, the damage area increases. However, the delamination area for the 50 J and 60 J impact is under predicted. From the experimental C-scan, the delamination growth is larger than the predicted damage. The failure mode is de-bonding in the tows of the back-face of the laminate which the homogeneous ply model has not captured. Figure 3.19 illustrates a comparison of the damage area between numerical and experiment. The predicted damage area measurements have been performed using ImageJ software. As shown in the plot, the experimental damage area increases linearly which indicates damage growth as the impact energy increases. As seen in Figure 3.19, there is a good agreement between predicted damage area for 30 J impact and experiment. While for 50 J and 60 J impact, a significant difference is observed in the predicted damage area compared to experiment. This difference is due to the release of the absorbed energy during the rebound stage of the impactor. Also, the discrepancy is because of the capability of the intralaminar failure criteria to predict an accurate damage at higher level of energy as well as the accuracy of the used values for the fracture energies.

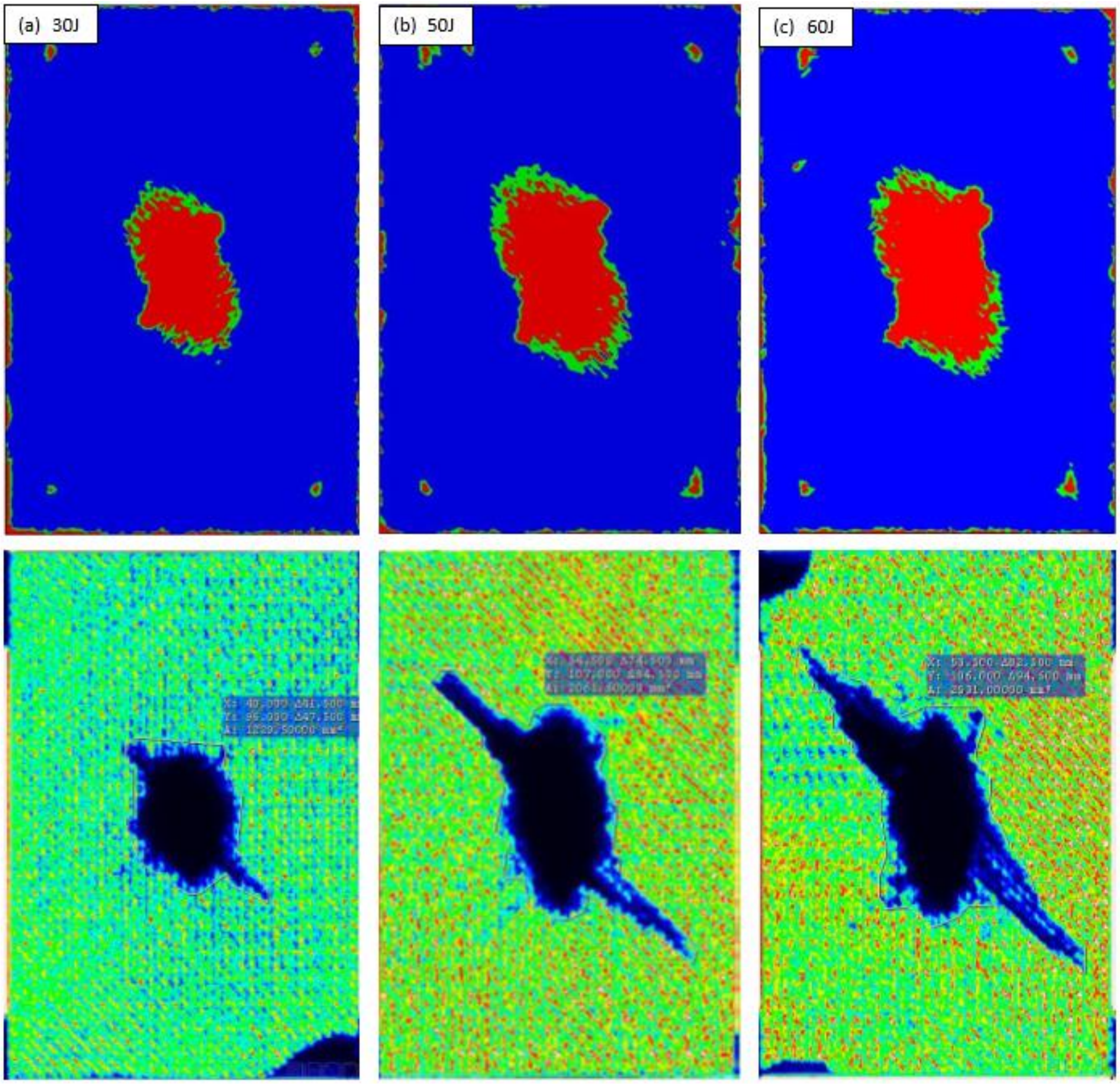

Figure 3. 18 Predicted damage envelope compared with experimental C-scan for laminates impacted at (a) 30 J, (b) 50 J and (c) 60 J

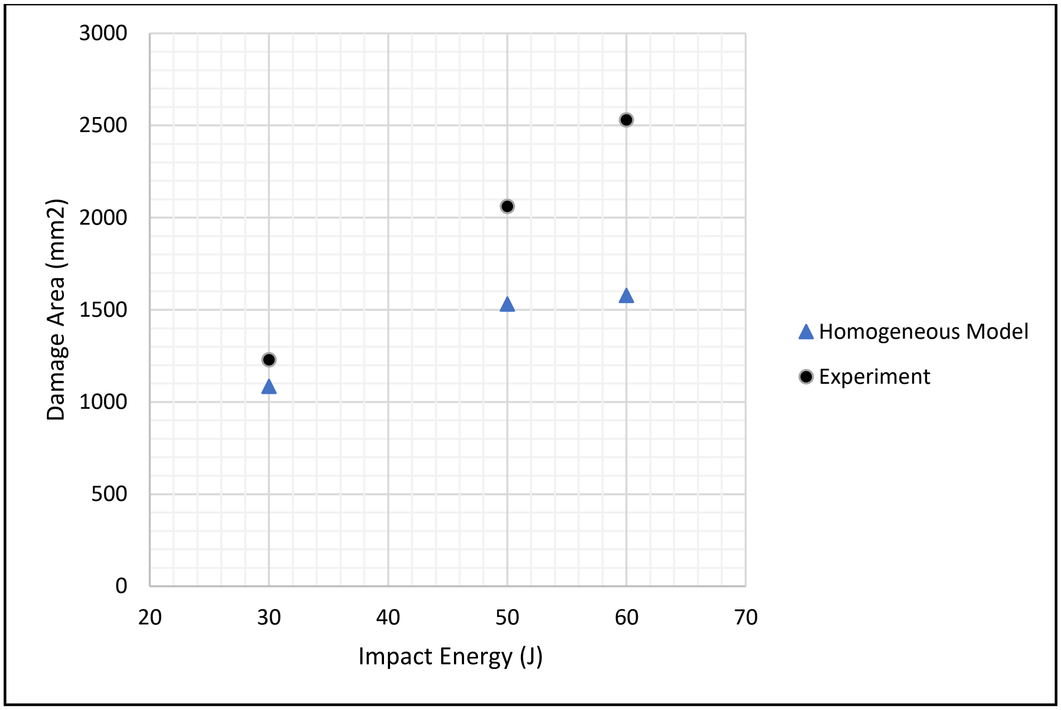

Figure 3. 19 Plot of the damage area vs. incident impact energy

During impact, damage occurs in the form of fiber failure, matrix failure and delamination between the plies. The predicted complete damage status (all failure modes) for 30 J impact in each lamina of the homogeneous ply model, starting from the top ply (impact region) to bottom ply is shown in Figure 3.20. The "rotating fan" damage pattern is predicted on the top few plies where the damage occurs perpendicular to the fiber direction as seen in Figure 3.20. The different damage modes for 30 J impact of the homogeneous ply model are shown in Figure 3.21. It is observed that most of the damage at the top plies are compression fiber failure as well as compression matrix failure. Whereas the tension failure modes, fiber and matrix, start to occur from the back surface of the laminate and progress toward the top surface. The topmost plies (impact region – under the impactor) have little fiber damage compared to matrix damage. A similar damage pattern of the rotating fan is predicted for the 50 J and 60 J impacts. Figures 3.22 and 3.23 illustrate the first eight plies as well as the through thickness damage for different damage modes of the laminate impacted at 50 J and 60 J, respectively. As can be seen from the figures, with increasing impact energy, the damage extent is larger for 50 J and 60 J impacts compared with 30 J impact.

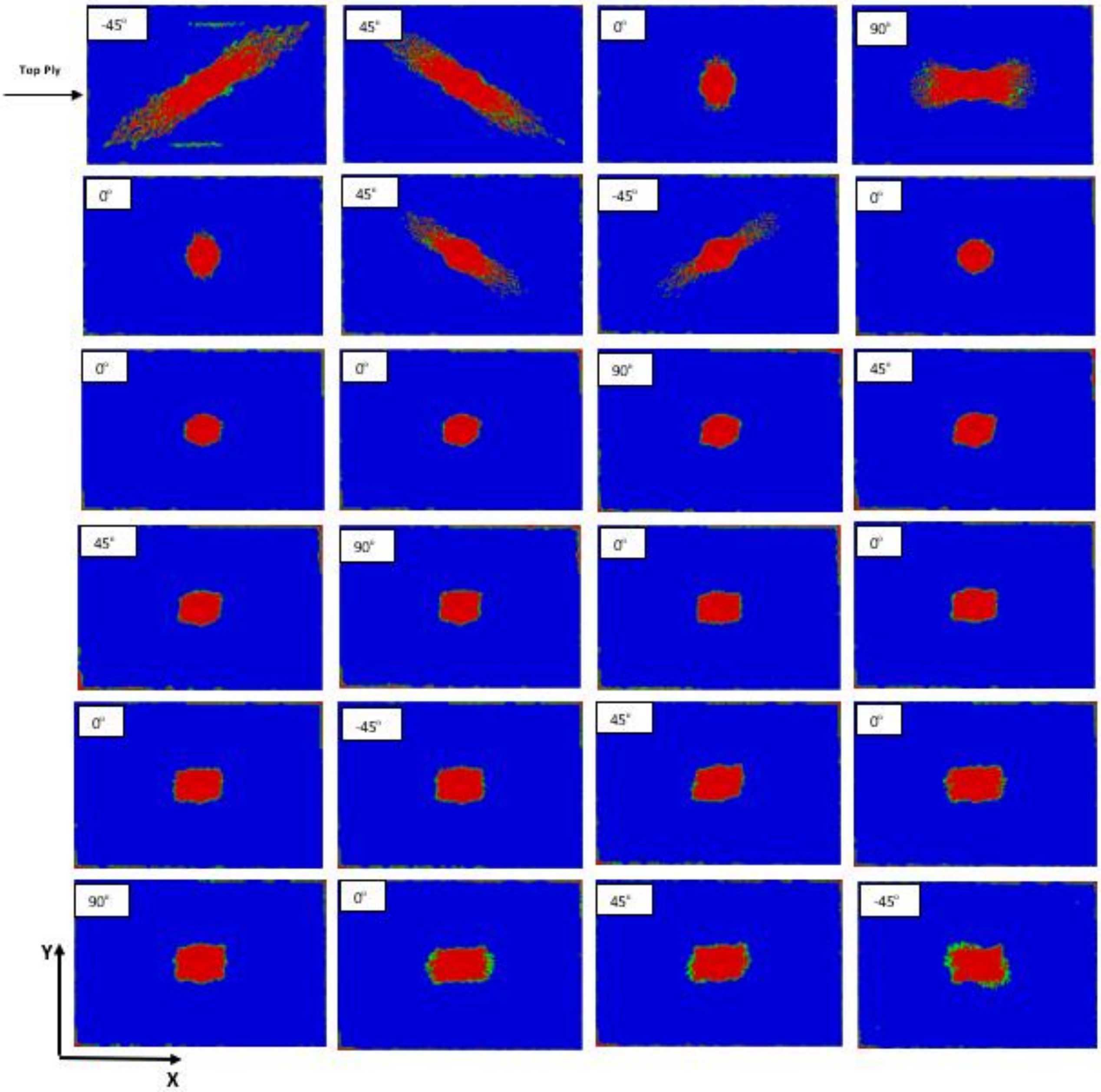

Figure 3. 20 The predicted damage extent in each ply for the 30 J impact

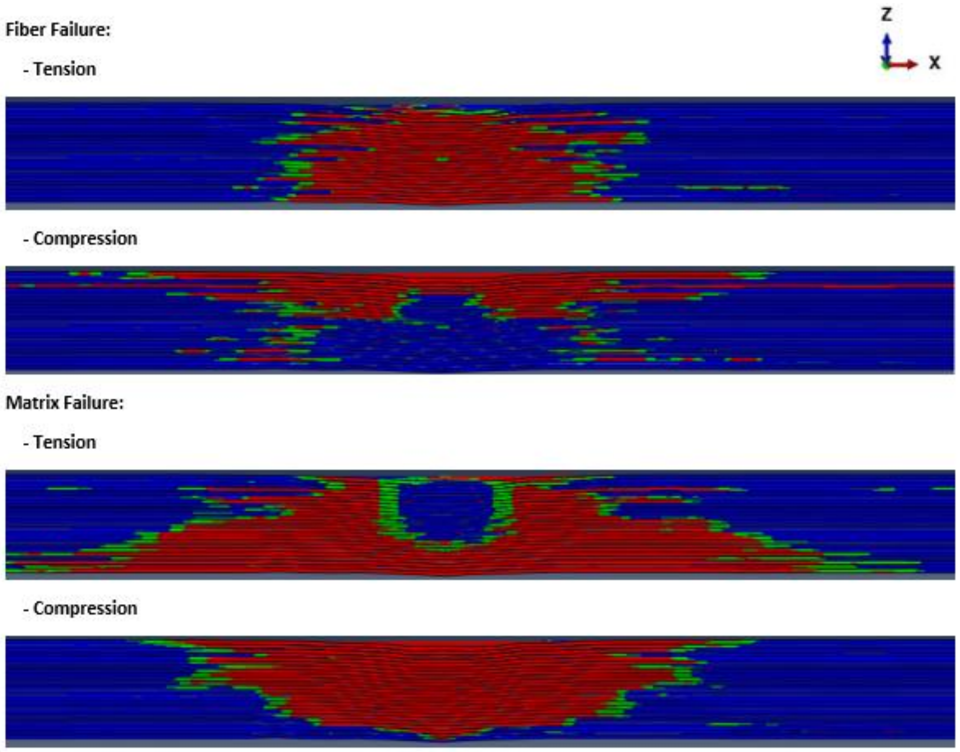

Figure 3. 21 Predicted through thickness damage contour for different damage modes for 30 J impact

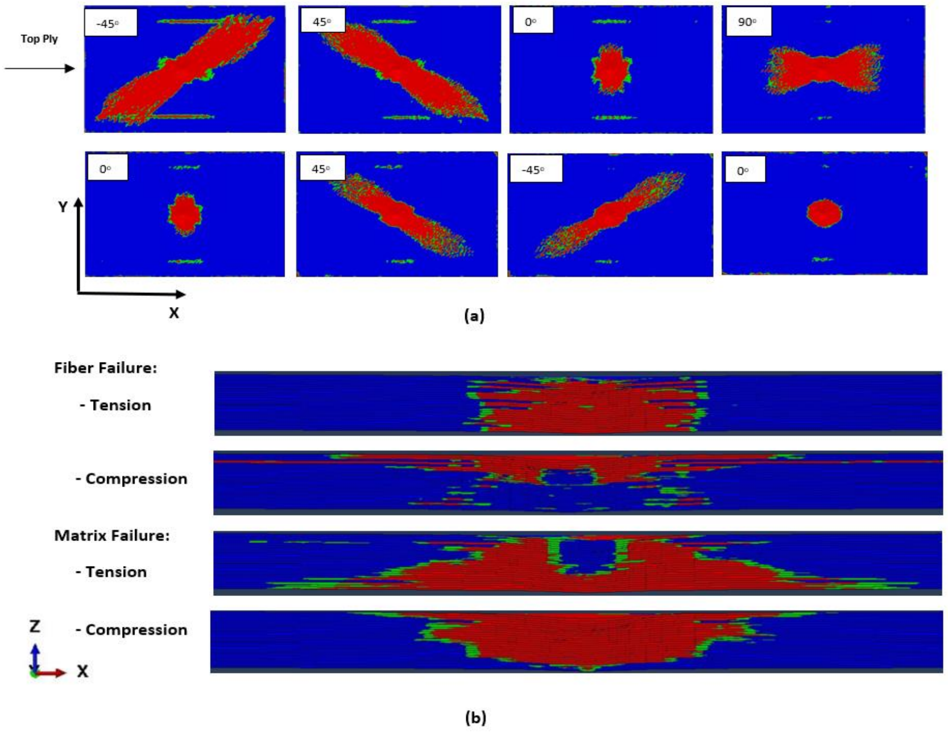

Figure 3. 22 Predicted damage contour of the laminate impacted at 50 J

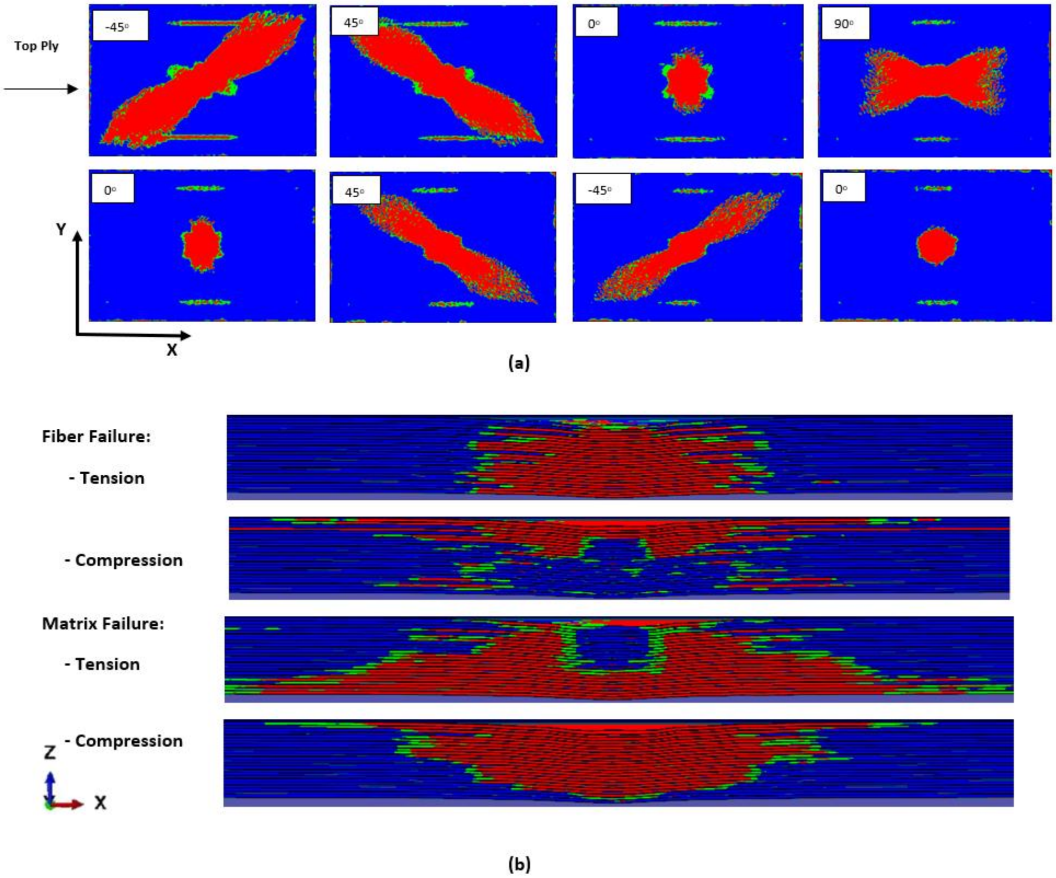

Figure 3. 23 Predicted damage contour of the laminate impacted at 60 J

The progressive damage of the homogeneous ply model during the 30 J impact event is shown in Figure 3.24. The time intervals are marked on the force-time curve and illustrated in Figure 3.24 (a). The progressive damage growth for different failure modes, fiber and matrix failure modes, of the homogeneous ply model is shown in Figures 3.24 (b) and (c). The damage of the homogeneous ply model grows steadily until the peak load, point (e). At the peak load (e) and beyond the peak load state, the extent of the damage is reached its final state, completely damaged.

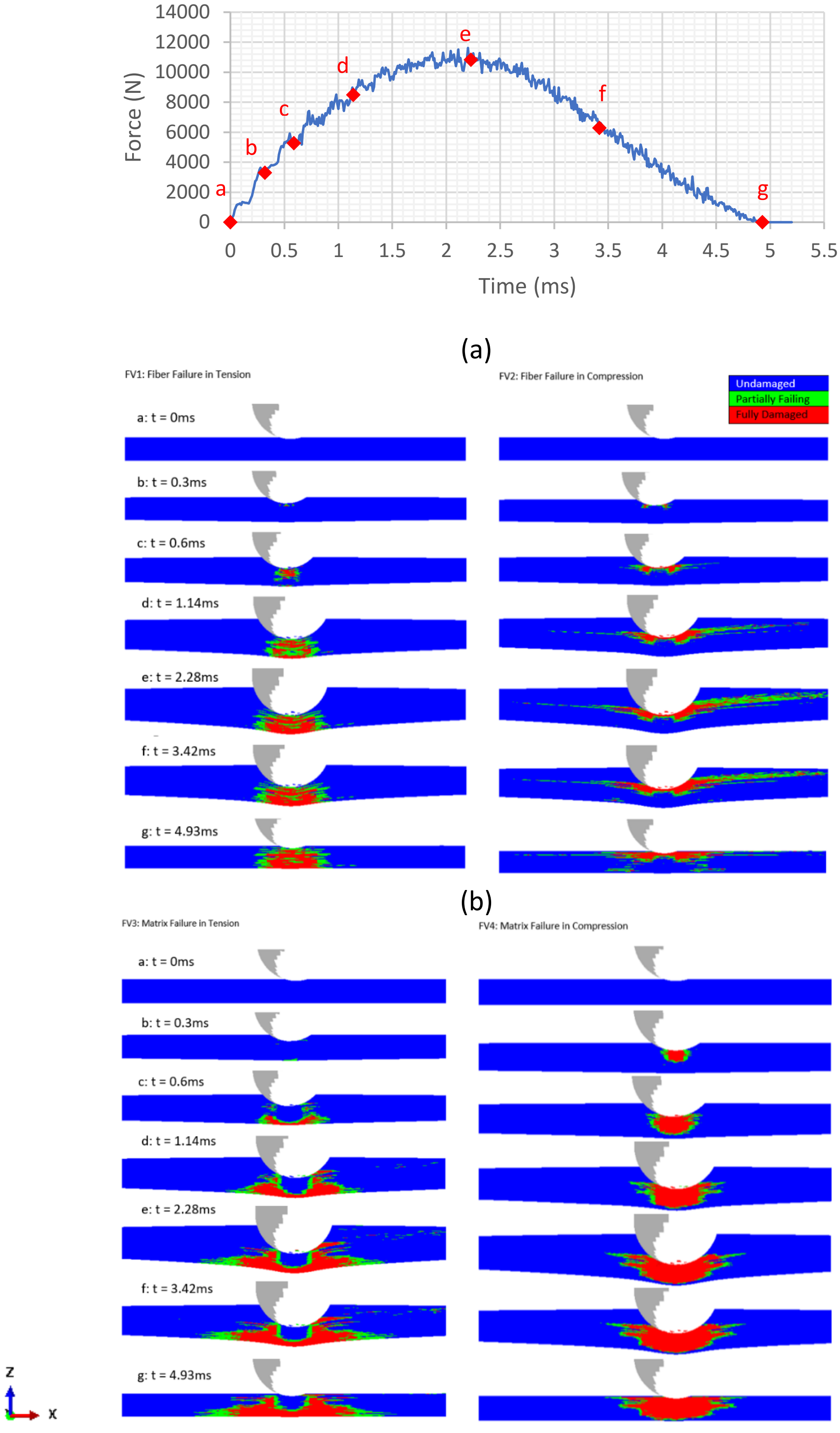

(a)

(b)

(c)

Figure 3. 24 The progressive damage growth of a homogeneous ply model impacted at 30J: (a) force-time curve, (b) fiber damage growth and (c) matrix damage growth

3.8.3 Conclusion

The NCF homogeneous ply laminate and mesoscale laminate are used to predict the low velocity impact response. The laminated composites are impacted at three different energy levels 30 J, 50 J and 60 J. The numerical results are validated with experimental results in terms of the force histories, absorbed energy and damage/delamination area. Excellent agreement is observed in terms of peak force, maximum deflection and damage area between homogeneous ply laminate and experiment for the 30 J impact with an overall error percentage less than 3 %. However, the mesoscale laminate is impacted at 30 J and the impact response is under predicted compared to experiment. The mesoscale laminate model requires mesh refinement to improve the accuracy of the impact response results. In the case of higher impact energies, 50 J and 60 J, the homogeneous ply model under predicts the impact response. It is observed that the level of accuracy decreases as the level of impact energy increases. The under prediction of the impact response is due to the accuracy of capturing the material behavior (damage) under impact loading. The fracture energies of mode II and III have to be determined experimentally in order to predict an accurate material behavior under the low velocity impact loading. In addition, the absorbed energies are under predicted in the case of low as well as high impact energy, and this is due to the released damage energy during the rebound phase of the impactor, and the residual strain effect is not captured in the models. Overall, based on the presented results of the low velocity impact, it can be concluded that the homogeneous ply model is reliable to predict the impact response up to 50 J impact energy.

Chapter 4 Predicting the Compression After Impact Performance of Multidirectional Fiber-Reinforced Laminate

4.1 Introduction

The accurate prediction of damage tolerance in fiber reinforced composite plays a significant role in reducing the weight of aerospace structures, especially in civil aircraft (Megat-Yusoff et al., 2019). The damage tolerance is studied to determine the effect of impact energies on the residual strength of the composites. The compression after impact (CAI) behavior of laminated structures is used/evaluated to measure the residual strength of composite structures (Tuo and Zhang et al., 2019). In this chapter, the proposed FE models for predicting the CAI response of the NCF composites are presented. The modeling of the FE NCF laminates is presented in Chapter 2. The CAI simulations are performed to measure the damage tolerance of the FE laminates after being damaged by low velocity impact. The composite laminates are subjected to an axial compression load to predict the compressive residual strength of the composites. The first step is to induce damage to the laminates using low velocity impact as presented in Chapter 3. This is then followed by a compression simulation of the damaged laminates. The CAI simulations utilize the progressive damage models detailed in Chapter 3 to predict the intralaminar and interlaminar failure. All experimental data presented in this Chapter are obtained from McDermott (2019) and used for the validation of the FE models for the CAI simulations.

4.2 Compression After Impact Methodology

The damage and failure models implemented to predict the intralaminar failure of the laminates utilize the 3D Hashin failure criteria to predict failure initiation and the exponential damage evolution law used to compute the damage variables for each failure mode. For the interlaminar failure, the quadratic stress criterion and the Benzeggagh and Kenane (BK) law are used to predict damage initiation and damage propagation, respectively. The damage models of the intralaminar and interlaminar failure are presented in detail in Chapter 3.

The CAI simulations are performed using ABAQUS/Explicit since it was used for the low velocity impact simulations. Instead of using ABAQUS/Implicit solver method for the CAI simulations (Quasi-static CAI), the ABAQUS/Explicit solver is implemented to avoid the complexity of converting the damaged model from the Explicit impact simulation to Implicit solver. In addition, the use of ABAQUS/Explicit would eliminate the conversion issue of ABAQUS/Implicit solver since there is non-linear behavior involved in the model.

As mentioned previously, the CAI simulation is carried out to study the effect of the impacted laminates on their residual strength. First, the damage of the laminates is induced using a low velocity impact as presented in Chapter 3. Once the impact simulations are completed, the composite laminates are subjected to axial compression to assess their damage tolerance. However, in order to predict an accurate response of the compression after impact, an intermediate process is performed to import the results from the impacted laminate to the CAI model as an initial state. The ABAQUS command “ *Import ” is used to import the results obtained from the impact simulations to the CAI model. The *Import command has the capability to import the stresses, strains and displacement to the CAI model. Additionally, this command is able to import the results of the intralaminar failure such as the field/damage variables and state variables (failure indicators) for each element as well as the delamination failure variable to the CAI model from the impacted laminate. To ensure that the results from the impacted laminate get imported accurately as an initial state to the CAI model, the CAI model has to be the same as the impacted laminate in terms of the number of elements, element type and part instances' name. Figure 4.1 illustrates a schematic of ABAQUS analysis steps.

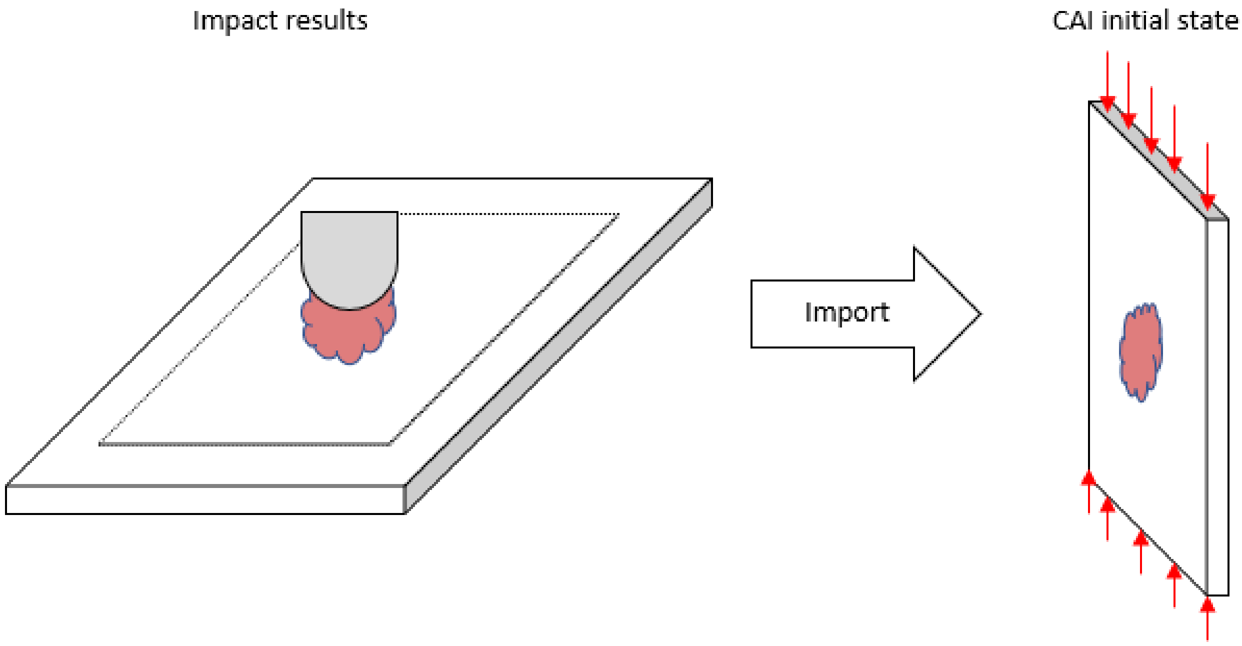

Figure 4. 1 A schematic of ABAQUS analysis steps

The laminated composite models are simulated in two sequential steps as follow:

1) Impact step: simulation of the impact loading and evaluation of the impact damage.
2) CAI step: the results from the impacted laminate are imported as an initial state to the CAI model and then the simulation of the CAI is performed until the model's failure.

In the second step, the results of the impacted laminate are imported on the CAI model where new boundary conditions are applied to perform the CAI simulations. The model dimensions, CAI setup and boundary conditions used for the simulations are shown in Figure 4.2. The dimensions of the composite plate used in the CAI simulations are 150 mm x 100 mm x 4.464 mm. The boundary conditions are applied based on the experiment setup where the Airbus test fixture (AITM 1-0010) is used to carry out the compression tests. The top and bottom regions are restrained in the thickness direction with the displacement component $U_3=0$. The bottom face is constrained such that there is no translation in 1-direction $U_1=0$ (vertical translation). One node at the bottom face is constrained in the horizontal translation such that $U_2=0$. The knife/side edges are simply supported through the thickness such that the displacement component $U_3=0$. The side edges are 115 mm long and they are 5 mm apart from the outer perimeter of the model. The prescribed load is applied as a displacement control at a constant load rate of 13.5 m/min in ABAQUS and it is applied on a reference point. The nodes of the top face are constrained to the motion of the reference point using the kinematic coupling constraint feature in ABAQUS.

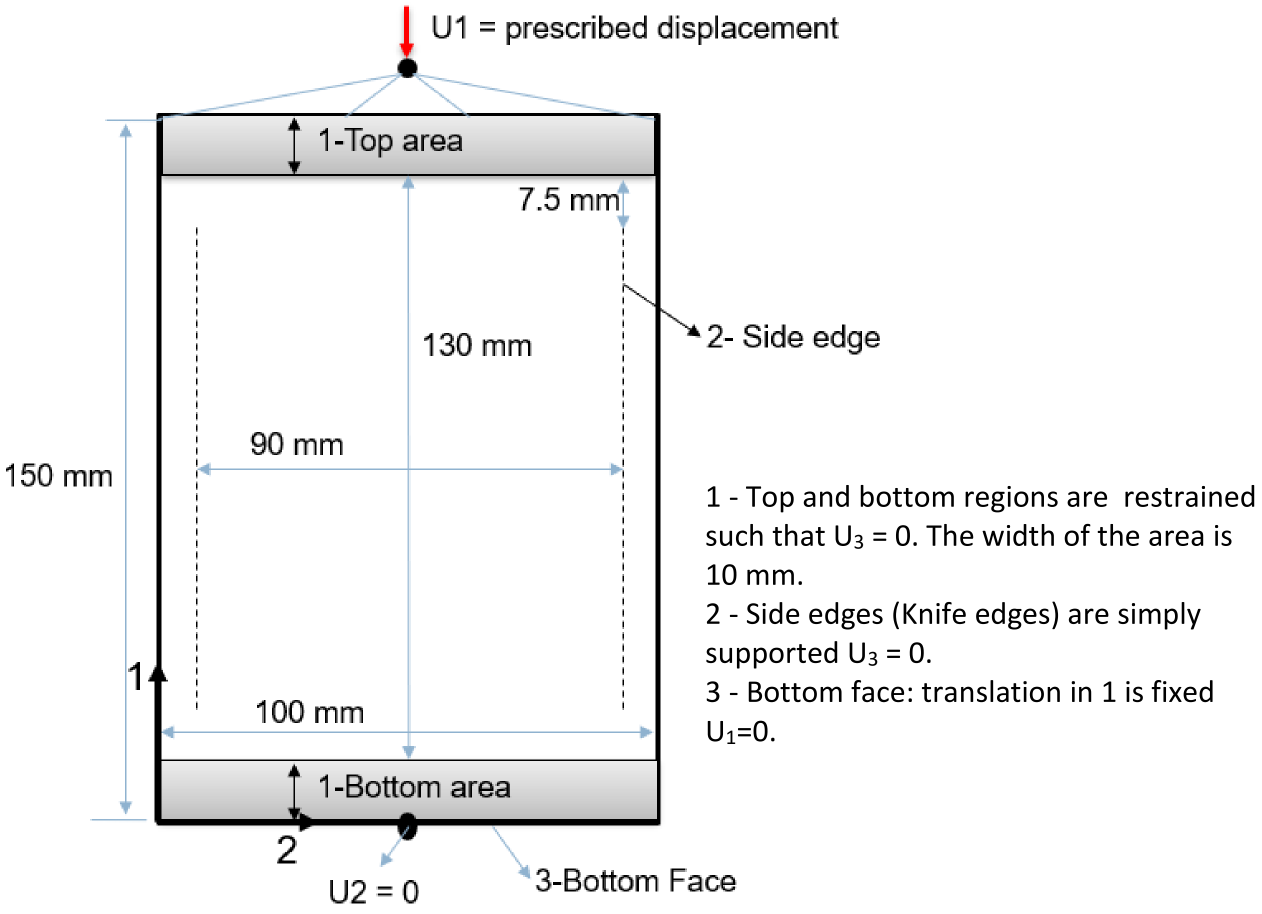

1 - Top and bottom regions are restrained such that $U_3 = 0$. The width of the area is 10 mm.
2 - Side edges (Knife edges) are simply supported $U_3 = 0$.
3 - Bottom face: translation in 1 is fixed $U_1=0$.

Figure 4. 2 Virtual CAI test setup of the FE model

4.3 Stress and Strain Calculations

The compressive stress-strain response for the composite laminates is calculated based on the reaction force and the displacement of the point load of the model. This approach is adopted so that an average stress and strain is determined for the whole model. The average stress and strain equations are shown in Equation (4.1) and (4.2), respectively.

$$\bar{\sigma} = \frac{RF}{A} \tag{4.1}$$

$$\bar{\varepsilon} = \frac{\delta}{L} \tag{4.2}$$

where RF is the reaction force of the load reference point, *A* is the cross-sectional area of the region where the load is applied, *δ* is the change in displacement and *L* is the length of the model. In the current model, the cross-sectional area $A = 446.4\ mm^2$and the length of the model $L = 130\ mm$.

4.4 Results and Discussion

The predicted compressive stress-strain responses for undamaged homogeneous ply and mesoscale models are shown in Figure 4.3 and summarized in Table 4.1. As seen in the figure and Table 4.1, the predicted moduli of the homogeneous ply model and mesoscale model are higher than the results obtained from experiment by 11.29 % and 12.57 %, respectively. The predicted compressive ultimate strength of the undamaged homogeneous ply laminate is higher than experiment by 2.69 %. However, for undamaged mesoscale laminate, the predicted ultimate strength is lower than experiment by 16.75 %. The under prediction of the ultimate strength for the mesoscale model is due to the inability of the mesoscale model to capture the tow geometries precisely, for more detail on the discussion of the mesoscale geometries is presented in Chapter 2 and 3.

As mentioned previously, in order to predict the compressive residual strength of the laminate accurately, it is important to first capture the impact response accurately. Based on the impact numerical results presented in Chapter 3, the impact response of the homogeneous ply laminate impacted at 30 J correlates very well with experiment in terms of peak force, maximum deflection, absorbed energy and damage area. Therefore, the homogeneous ply laminate impacted at 30 J is taken to a further step to measure the damage tolerance of the laminate after impact. The comparison of the compressive stress-strain response between numerical and experiment for 30 J CAI test is shown in Figure 4.4. The predicted stress-strain response of homogeneous laminate for 30 J CAI correlates very well with experiment. The predicted compressive residual strength, listed in Table 4.1, is lower than experiment by 4.75 %. The effect on the ultimate strength is shown in Figure 4.4 of the impacted laminate where a lower ultimate strength is predicted compared to the undamaged result of the homogeneous ply model illustrated in Figure 4.3. A summary of the predicted and experimental moduli is listed in Table 4.1 where the percentages are the difference between numerical and experiment. The moduli for the laminates are predicted and compared with experiment, the predicted and experimental moduli are computed in the range of 0.1 % to 0.3 % strain. The experimental values presented are the average value of four to five tested specimens. The predicted moduli are higher than experiment as seen in Table 4.1. The reason for obtaining low compressive modulus experimentally can be due to the difference between the setup of the test and the boundary conditions used for numerical simulations. Another reason for obtaining different moduli is because of the material behavior of the composite under compression test. For instance, there is a tendency for micro buckling of carbon fibers subjected to compression load which has been noticed experimentally (Mujika et al., 2006).

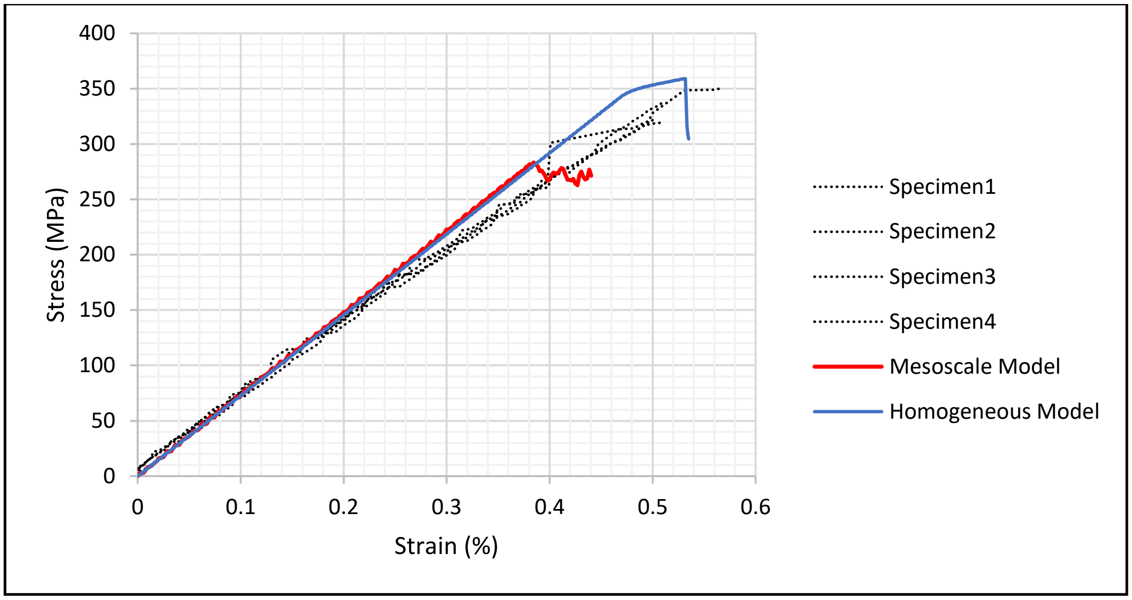

Figure 4. 3 Compressive stress-strain responses for undamaged homogenous model and mesoscale model

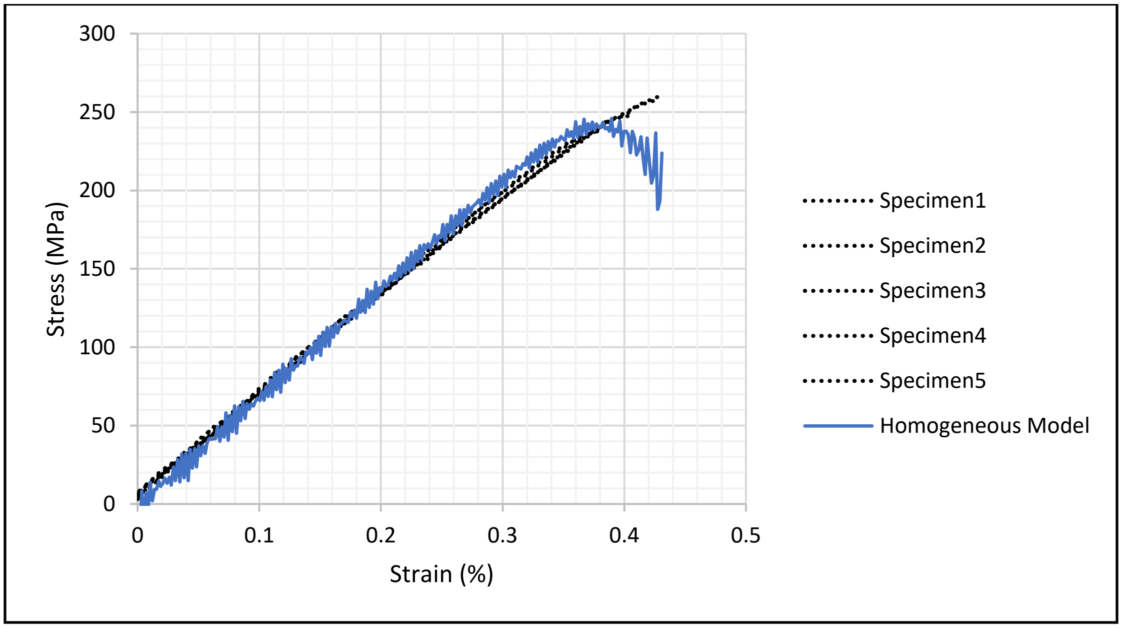

Figure 4. 4 Compressive stress-strain responses for 30 J CAI test of homogeneous ply model

Table 4. 1 Results summary of CAI

Energy Level / Model		Ultimate Strength (MPa)	Modulus (GPa)
0 J	Experiment	335	65
	Homogeneous ply model	344.12 (2.69%)	72.78 (11.29%)
	Mesoscale Model	283.21 (16.75%)	73.72 (12.57%)
30 J	Experiment	250	63.50
	Homogeneous ply model	238.39 (4.75%)	68.49 (5.0%)

4.5 Conclusions

The compressive residual strength of the homogeneous ply model impacted at 30 J is predicted. Good agreement is observed between the CAI of the homogeneous ply model and experiment. The predicted compressive residual strength of the homogeneous ply laminate impacted at 30 J is within 4.75 % of the averaged experimental value. For the undamaged CAI simulations, the homogeneous ply laminate demonstrates a better prediction of the ultimate strength compared to the mesoscale laminate. The predicted moduli of the laminates are higher than experiment. The difference between the numerical and experimental results is due to the application of the boundary conditions. In addition, the difference between the numerical and experimental moduli is because of the material behavior of the composite under compression test such that the composite laminate might experience a micro buckling of the fibers during the experiment and it was not captured numerically (Mujika et al., 2006). Overall, the homogeneous ply laminate showed excellent performance in terms of predicting the compressive residual strength for a laminate impacted at 30 J as well as the undamaged compressive strength.

Chapter 5 Conclusions and Future Work/Recommendations

5.1 Conclusions

In this thesis, numerical tools are used to investigate fiber-reinforced composites under low velocity impact loading and predict the compressive residual strength of the laminate after impact. Finite element NCF models are developed to study their mechanical behavior under impact loading. The NCF models are generated using two approaches. First approach, a finite element homogeneous ply laminate is generated where in this model there is no difference in the model's constituent. Second approach, a finite element mesoscale model as a plate which consists of tows geometries as well as matrix geometries where the constituents of the plate are considered as different parts.

Chapter 3 presents the modeling and results of the low velocity impact simulations. The finite element homogeneous ply laminate is impacted at three different levels of impact energy 30 J, 50 J and 60 J. While the finite element mesoscale laminate is impacted at only 30 J because it is computationally expensive due to the large number of elements used to generate the mesoscale model. The presented numerical results are validated with experimental data in terms of the peak force, absorbed energy, maximum deflection and damage area. It is observed that the predicted impact response of the mesoscale model does not correlate well with the experimental data. In order to have an accurate impact response of the mesoscale model, a mesh refinement has to be performed to the mesoscale model where a large number of elements is required to capture the geometries of the model, e.g. tow geometries and matrix geometries. Based on the convergence study presented in Chapter 2, the mesoscale model requires over 10,000,000 elements to produce accurate results whereas the current mesoscale model is generated with 1,920,000 elements. However, the homogeneous ply model showed excellent agreement with experimental data up to 50 J impact energy. In the case of higher impact energies, 50 J and 60 J, the homogeneous ply model over predicted the peak forces and under predicted the progressive damage of the laminate compared to experiment. The discrepancy between the numerical and experiment for higher levels of impact energy might be due to the inaccuracy of some of the assumed parameters such as the interlaminar material properties. Based on the literature presented in Chapter 1, it is found that the values of the fracture energies used in simulations play an important key to capture the overall impact response.

Chapter 4 presents the modeling and results of the compression after impact. The compressive ultimate strength is predicted for undamaged mesoscale model as well as undamaged homogeneous ply model. The predicted ultimate strength for the undamaged homogeneous ply model is in good agreement with experiment with a difference of 2.69 %. However, the mesoscale model under predicts the ultimate strength compared to experiment by 16.75 %. The compressive residual strength after impact is predicted for homogeneous ply laminate subjected to 30 J impact. The predicted compressive residual strength correlates well with experiment with a difference of 4.75 %. In addition, the laminates moduli are calculated and listed in Table 4.1. The predicted Young's moduli are higher than the experimental values. The difference in the numerical and experimental moduli may be due to the application of the boundary conditions. Also, the difference between the numerical and experimental moduli is because of the material behavior of the composite under compression test such that the carbon fibers of the specimen might experience a micro buckling during the experiment and it was not captured numerically (Mujika et al., 2006).

From the results presented in Chapters 3 and 4, it can be concluded that the homogeneous ply model can be used to perform low velocity impact simulations and predict the compressive residual strength of the laminate. It is computationally efficient to use a homogeneous ply model since it does not require a large number of elements to predict the impact response as well as the compressive residual strength. Based on the results presented, the homogeneous ply laminate can predict an accurate low velocity impact response up to 50 J impact energy. There are still more improvements that can be done to improve the accuracy of the results as well as to reduce the cost of the simulations.

5.2 Future Work/Recommendations

The finite element simulations require additional work to accurately predict the progressive damage of the laminates. Additional implementations are presented below that would be beneficial for improving the accuracy of the results.

1. The modeling technique used to generate the homogeneous ply model and the mesoscale model can be revised. A small impact region (homogeneous/mesoscale region) can be generated with fine mesh surrounded by a homogeneous region generated with coarse mesh. The impact region and the surrounded region is connected through a “tie constraint” to control the motion between the two regions. This approach would make the simulations more efficient which will lower the cost of running the simulations.

2. The accuracy of the finite element simulations depends on the values of fracture energy. To improve the interlaminar damage prediction, it is very important to measure the fracture energy experimentally and use the values in the modeling to simulate an accurate impact response as well as predict the compressive residual strength. In addition, the cohesive response parameter η should be obtained based on experimental data of fracture energy to predict delamination more accurately.
3. A criterion should be implemented to account for the residual strain that would capture the permanent deformation.
4. For predicting the compressive residual strength of the laminate after impact, it is recommended to stabilize the laminate (i.e. use Rayleigh damping) after impact and then import the damage from impact to the CAI model.

REFERENCES

ABAQUS. (2017). *ABAQUS User's Manual, Dassault Systemes Simulia Corp.*

Abir, M., Tay, T., Ridha, M., & Lee, H. (2017). Modelling Damage Growth in Composites Subjected to Impact and Compression after Impact. *Composite Structures, 168*, 13-25.

Abrate, S. (2011). *Impact Engineering of Composite Structures.*

Barbero, E. J. (2011). *Introduction to Composite Materials Design .*

Belingardi, G., & Vadori, R. (2002). Low Velocity Impact Tests of Laminate Glass-Fiber-Epoxy Matrix Composite Material Plates. *International Journal of Impact Engineering, 27*, 213-229.

Benzeggagh, M., & Kenane, M. (1996). Measurement of Mixed-Mode Delamination Fracture Toughness of Unidirectional Glass/Epoxy Composites with Mixedmode Bending Apparatus. *Composites Science and Technology, 56*(4), 439-449.

Breen, C., Guild, F., & Pavier, M. (2006). Impact Damage to Thick Carbon Fiber Reinforced Plastic Composite Laminates. *Journal of Materials Sience, 41*, 6718-6724.

Carruthers, J., Kettle, A., & Robinson, A. (1998). Energy Absorption Capability and Crashworthiness of Composite Material Structures: Review. *Applied Mechanics Review, 51*, 635-649.

CYCOM PR 520 RTM RESIN SYSTEM. (n.d.). Retrieved from https://www.e-aircraftsupply.com/MSDS/111329CYCOM%20PR520%20RTM%20tds.pdf

Dogan, F., Hadavinia, H., Donchev, T., & Bhonge, P. (2012). Delamination of Impacted Composite Structures by Cohesive Zone Interface Elements and Tiebreak Contact. *Central European Journal of Engineering, 2*(4), 612-626.

Falzon, B. G., Tan, W., Price, M., & Liu, H. (2016). The Role of Material Characterisation in the Crush Modelling of Thermoplastic Composite Structures. *Composite Structures, 153*, 914-927.

Findlay, S., & Harrison, N. (2002). Why Aircraft Fail. *Materials Today*, 18-25.

Francesconi, L., & Aymerich, F. (2017). Numerical simulation of the Effect of Stitching on the Delamination Resistance of Laminated Composites Subjected to Low-Velocity Impact. *Composite Structures, 159*, 110-120.

González, E., Maimí, P., Camanho, P., Turon, A., & Mayugo, J. (2012). Simulation of Drop-Weight Impact and Compression after Impact Tests on Composite Laminates. *Composite Structures, 94*, 3364–3378.

Guo, W., Xue, P., & Yang, J. (2013). Nonlinear Progressive Damage Model for Composite Laminates Used for Low-Velocity Impact. *Applied Mathematics and Mechanics, 34*, 1145-1154.

Hashin, Z. (1980). Failure Criteria for Unidirectional Fiber Composites. *Journal of Applied Mechanics, 47*, 329-334.

HEXCEL. (n.d.). *HexTow IM7 Carbon Fiber .* Retrieved from https://www.hexcel.com/user_area/content_media/raw/IM7_HexTow_DataSheet.pdf

Hirai, Y., Hamada, H., & Kim, J. (1998). Impact Response of Woven Glass Fabric Composites-I. Effect of Fiber Surface Treatment . *Composites Science and Technology*, 91-104.

Hou , J., Petrinic, N., Ruiz, C., & Hallett, S. (2000). Prediction of Impact Damage in Composite Plates. *Composites Science and Technology, 60*, 273-281.

Hull, D. (1991). Unified Approach to Progressive Crushing of Fiber-Reinforced Composite Tubes. *Composite Science and Technology, 40*, 377-421.

Li, S. (2001). General Unit Cells for Micromechanical Analyses of Unidirectional Composites . *Composites Part A, 32*(6), 815-826.

Lin, S., & Waas, A. M. (2019). Experimental and Numerical Study on the Low Velocity Impact Damage of a Shear Dominated Composite Laminate. *AIAA Scitech 2019 Forum.*

Liu, H., Falzon, B. G., & Tan, W. (2018). Predicting the Compression-After-Impact (CAI) Strength of Damage-Tolerant Hybrid Unidirectional/Woven Carbon-Fibre Reinforced Composite Laminates. *Composites Part A*, 189-202.

Long, A C and Brown, L P. (2011). Composite reinforcements for optimum performance: Modelling the geometry of textile reinforcements for composites: TexGen, edited by P. Boisse, Woodhead Publishing Ltd, ISBN: 978-1-84569-965-9.

Maio, L., Monaco, E., Ricci, F., & Lecce, L. (2013). Simulation of Low Velocity Impact on Composite Laminates with Progressive Failure Analysis. *Composite Structures, 103*, 75-85.

Mathivanan, N. R., & Jerald, J. (2010). Experimental Investigation of Low-Velocity Impact Characteristics of Woven Glass Fiber Epoxy Matrix Composite Laminates of EP3 Grade. *Materials and Design, 31*, 4553-4560.

Matzenmiller, A., Lubliner, J., & Taylor, R. (1995). A Constitutive Model for Anisotropic Damage in Fiber-Composites. *Mechanics of Materials*, 125-152.

McDermott, J. Damage Resistance and Tolerance of 3D Woven Composites. Master thesis, 2019.

Megat-Yusoff, P., Shah, S., Karuppanan,, S., & Sajid, Z. (2019). Impact Resistance and Damage Tolerance of Fiber Reinforced Composites: A Review. *Composite Structures, 217*, 100-121.

Mujika, F., Carbajal, N., Arrese, A., & Mondragon, I. (2006). Determination of Tensile and Compressive Moduli by Flexural Tests. *Polymer Testing, 25*, 766-771.

Naik, N. K., & Shrirao, P. (2004). Composite Structures under Ballistic Impact. *Composite Structures, 66*, 579-590.

Omairey, S. L., Dunning, P. D., & Sriramula, S. (2019). Development of an ABAQUS Plugin Tool for Periodic RVE Homogenisation. *Engineering with Computers, 35*, 567-577.

Perillo, G., & Jørgensen, J. K. (2016). Numerical/Experimental Study Of The Impact and Compression After Impact On GFRP Composite For Wind/Marine Applications. *Procedia Engineering, 167*, 129-137.

Pernas-Sánchez, J., Pedroche , D., Varas, D., López-Puente, J., & Zaera, R. (2012). Numerical Modeling of Ice Behavior under High Velocity Impacts. *International Journal of Solids and Structures, 49*, 1919-1927.

Prichard, J., & Hogg, P. (1990). The Role of Impact Damage in Post-Impact Compression Testing. *Composites, 21*, 503-511.

Safri, S., Sultan, M., Yidris, N., & Mustapha, F. (2014). Low Velocity and High Velocity Impact Test on Composite Materials – A review. *The International Journal of Engineering and Science, 3*(9), 50-60.

Sjoblom, P., HARTNESS, J., & CORDELL, T. (1998). On Low-Velocity Impact Testing of Composite Materials. *Journal of COMPOSITE MATERIALS, 22*, 30-52.

Sun, X., & Tong, M. (2015). Finite Element Analysis of Low-Velocity Impact Damage on Stiffened Composite Panels. *International Journal of Aerospace and Mechanical Engineering*, 1259-1263.

Topac, O., Gozluklu, B., Gurses, E., & Coker, D. (2017). Experimental and Computational Study of the Damage Process in CFRP Composite Beams under Low-Velocity Impact. *Composites: Part A, 92*, 167-182.

Tuo, H., Lu, Z., Ma, X., Xing, J., & Zhang, C. (2019). Damage and Failure Mechanism of Thin Composite Laminates under Low-Velocity Impact and Compression-after-Impact Loading Conditions. *Composites Part B, 163*, 642-654.

Vaidya, Uday K. (2011). Impact Response of Laminated and Sandwich Composites. [book auth.] Serge Abrate. Impact Engineering of Composite Structures . Brimingham : Springer Wien New York , 97-191.

Waas, A. M., Thorsson, S. I., & Rassaian, M. (2018). Low-Velocity Impact Predictions of Composite Laminates using a Continuum Shell Based Modeling Approach Part b: BVID Impact and Compression after Impact. *International Journal of Solids and Structures*, 201-212.

Warren, K., Lopez-Anid0, R., Vel, S., & Bayraktar, H. (2016). Progressive Failure Analysis of Three-Dimensional Woven Carbon Composites in Single-Bolt, Double-Shear Bearing . *Composites Part B, 84*, 266-276.

Zhang, C., Li, N., Wang, W., Binienda, W., & Fang, H. (2015). Progressive Damage Simulation of Triaxially Braided Composite using a 3D Meso-scale Finite Element Model. *Composite Structures, 125*, 104-116.

Zumpano, G., Stronge, W., & Sutcliffe, M. (2008). Impact Damage in Hybrid Braided Twill Composites. *Journal of Materials Science, 43*, 6668-6675.

APPENDICES

APPENDIX A: TexGen Scripts

A.1 A Python script to generate a unit cell model in TexGen

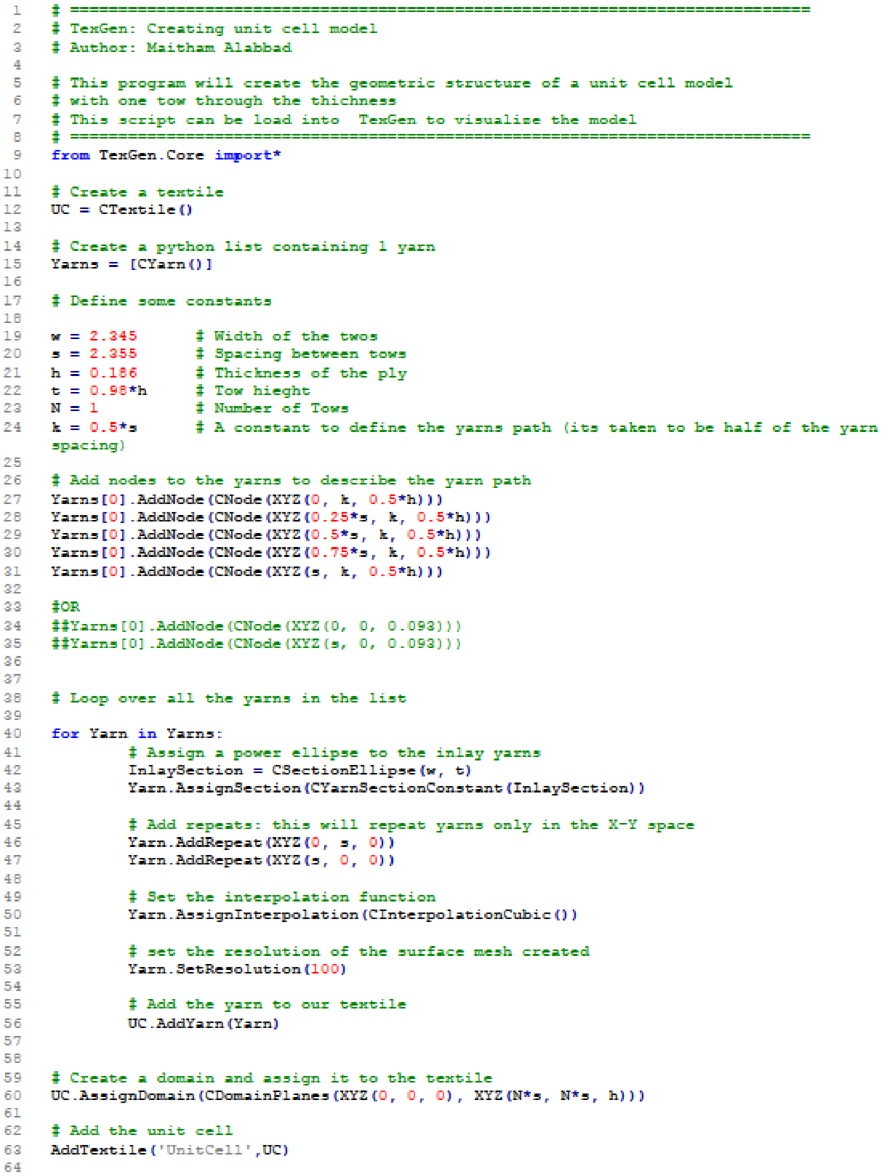

```
# =============================================================================
# TexGen: Creating unit cell model
# Author: Maitham Alabbad

# This program will create the geometric structure of a unit cell model
# with one tow through the thichness
# This script can be load into  TexGen to visualize the model
# =============================================================================
from TexGen.Core import*

# Create a textile
UC = CTextile()

# Create a python list containing 1 yarn
Yarns = [CYarn()]

# Define some constants

w = 2.345      # Width of the twos
s = 2.355      # Spacing between tows
h = 0.186      # Thickness of the ply
t = 0.98*h     # Tow hieght
N = 1          # Number of Tows
k = 0.5*s      # A constant to define the yarns path (its taken to be half of the yarn
spacing)

# Add nodes to the yarns to describe the yarn path
Yarns[0].AddNode(CNode(XYZ(0, k, 0.5*h)))
Yarns[0].AddNode(CNode(XYZ(0.25*s, k, 0.5*h)))
Yarns[0].AddNode(CNode(XYZ(0.5*s, k, 0.5*h)))
Yarns[0].AddNode(CNode(XYZ(0.75*s, k, 0.5*h)))
Yarns[0].AddNode(CNode(XYZ(s, k, 0.5*h)))

#OR
##Yarns[0].AddNode(CNode(XYZ(0, 0, 0.093)))
##Yarns[0].AddNode(CNode(XYZ(s, 0, 0.093)))


# Loop over all the yarns in the list

for Yarn in Yarns:
        # Assign a power ellipse to the inlay yarns
        InlaySection = CSectionEllipse(w, t)
        Yarn.AssignSection(CYarnSectionConstant(InlaySection))

        # Add repeats: this will repeat yarns only in the X-Y space
        Yarn.AddRepeat(XYZ(0, s, 0))
        Yarn.AddRepeat(XYZ(s, 0, 0))

        # Set the interpolation function
        Yarn.AssignInterpolation(CInterpolationCubic())

        # set the resolution of the surface mesh created
        Yarn.SetResolution(100)

        # Add the yarn to our textile
        UC.AddYarn(Yarn)


# Create a domain and assign it to the textile
UC.AssignDomain(CDomainPlanes(XYZ(0, 0, 0), XYZ(N*s, N*s, h)))

# Add the unit cell
AddTextile('UnitCell',UC)

```

A.2 A Python script to generate NCF mesoscale model in TexGen

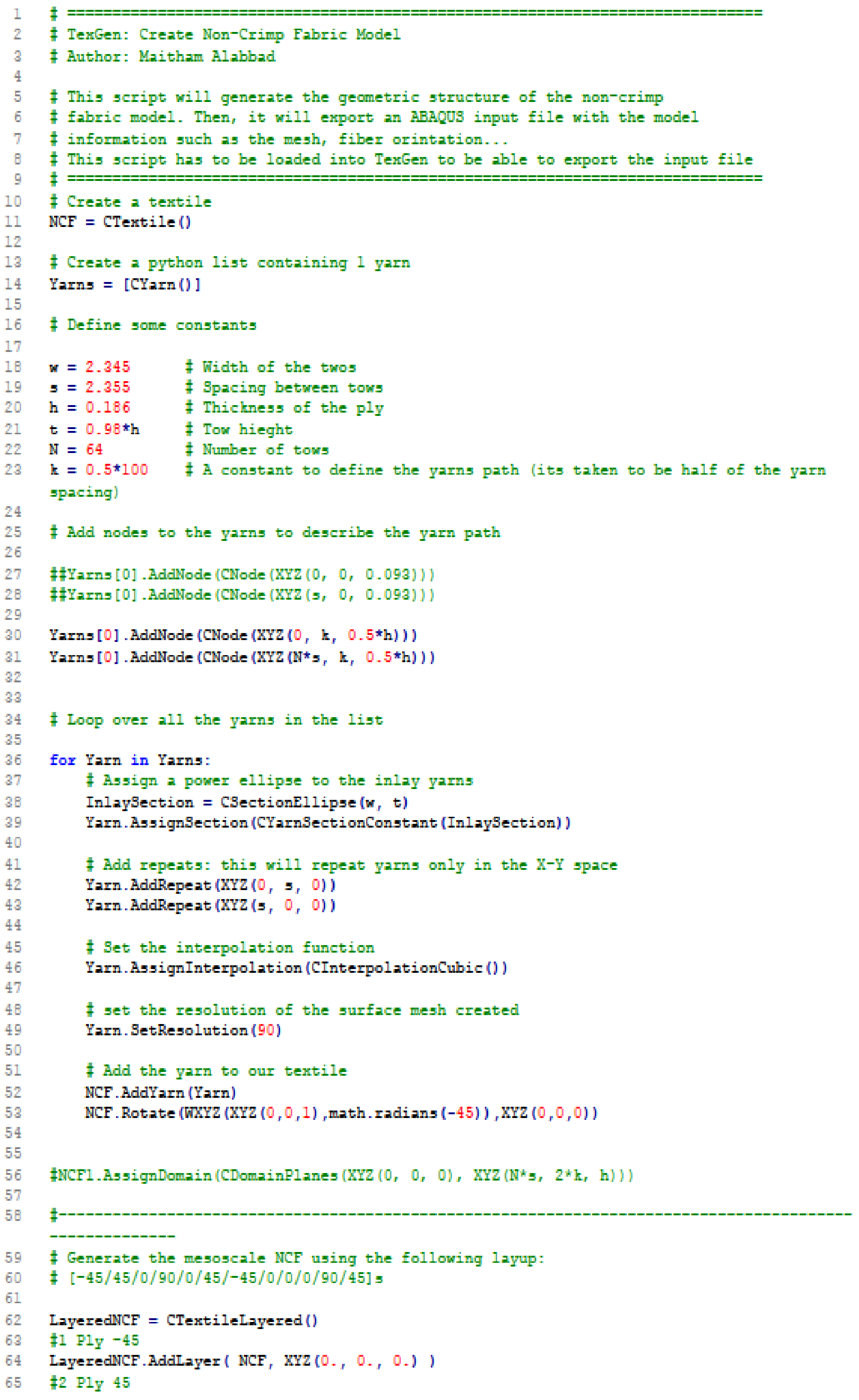

```
# ============================================================================
# TexGen: Create Non-Crimp Fabric Model
# Author: Maitham Alabbad

# This script will generate the geometric structure of the non-crimp
# fabric model. Then, it will export an ABAQUS input file with the model
# information such as the mesh, fiber orintation...
# This script has to be loaded into TexGen to be able to export the input file
# ============================================================================
# Create a textile
NCF = CTextile()

# Create a python list containing 1 yarn
Yarns = [CYarn()]

# Define some constants

w = 2.345       # Width of the twos
s = 2.355       # Spacing between tows
h = 0.186       # Thickness of the ply
t = 0.98*h      # Tow hieght
N = 64          # Number of tows
k = 0.5*100     # A constant to define the yarns path (its taken to be half of the yarn spacing)

# Add nodes to the yarns to describe the yarn path

##Yarns[0].AddNode(CNode(XYZ(0, 0, 0.093)))
##Yarns[0].AddNode(CNode(XYZ(s, 0, 0.093)))

Yarns[0].AddNode(CNode(XYZ(0, k, 0.5*h)))
Yarns[0].AddNode(CNode(XYZ(N*s, k, 0.5*h)))


# Loop over all the yarns in the list

for Yarn in Yarns:
    # Assign a power ellipse to the inlay yarns
    InlaySection = CSectionEllipse(w, t)
    Yarn.AssignSection(CYarnSectionConstant(InlaySection))

    # Add repeats: this will repeat yarns only in the X-Y space
    Yarn.AddRepeat(XYZ(0, s, 0))
    Yarn.AddRepeat(XYZ(s, 0, 0))

    # Set the interpolation function
    Yarn.AssignInterpolation(CInterpolationCubic())

    # set the resolution of the surface mesh created
    Yarn.SetResolution(90)

    # Add the yarn to our textile
    NCF.AddYarn(Yarn)
    NCF.Rotate(WXYZ(XYZ(0,0,1),math.radians(-45)),XYZ(0,0,0))


#NCF1.AssignDomain(CDomainPlanes(XYZ(0, 0, 0), XYZ(N*s, 2*k, h)))

#-----------------------------------------------------------------------------------------------------
# Generate the mesoscale NCF using the following layup:
# [-45/45/0/90/0/45/-45/0/0/0/90/45]s

LayeredNCF = CTextileLayered()
#1 Ply -45
LayeredNCF.AddLayer( NCF, XYZ(0., 0., 0.) )
#2 Ply 45
```

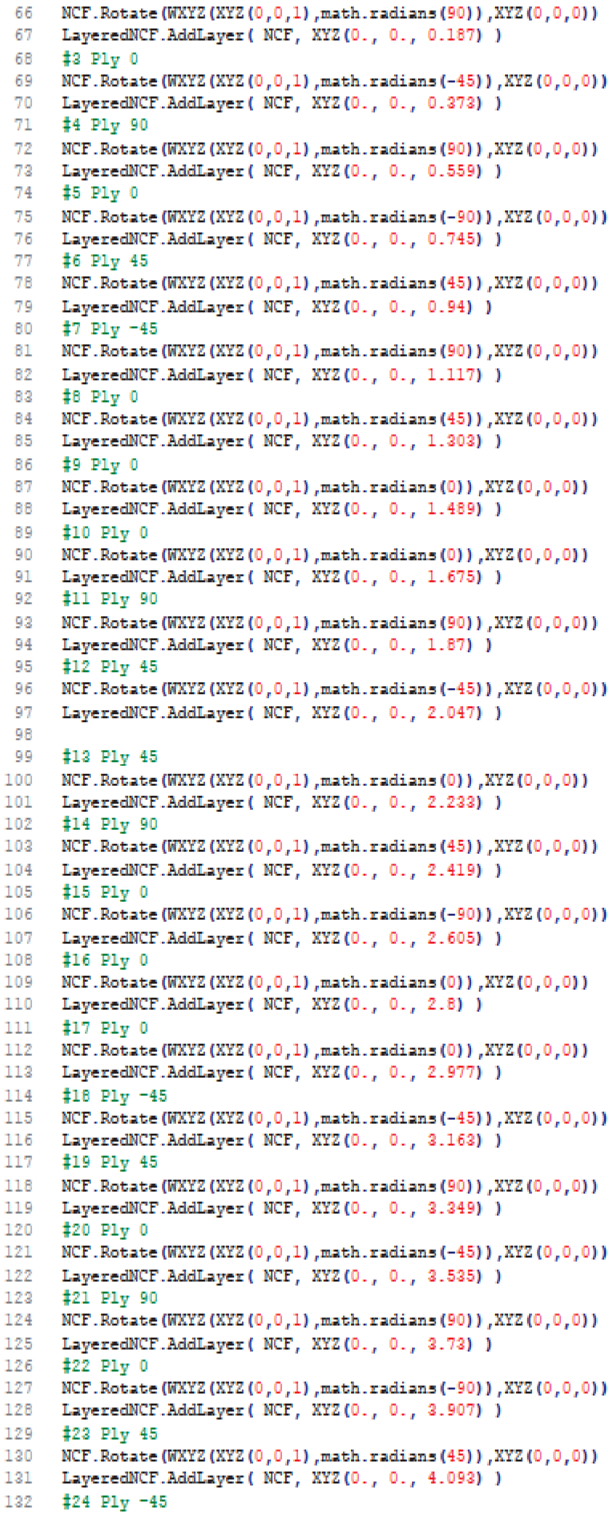

```
NCF.Rotate(WXYZ(XYZ(0,0,1),math.radians(90)),XYZ(0,0,0))
LayeredNCF.AddLayer( NCF, XYZ(0., 0., 0.187) )
#3 Ply 0
NCF.Rotate(WXYZ(XYZ(0,0,1),math.radians(-45)),XYZ(0,0,0))
LayeredNCF.AddLayer( NCF, XYZ(0., 0., 0.373) )
#4 Ply 90
NCF.Rotate(WXYZ(XYZ(0,0,1),math.radians(90)),XYZ(0,0,0))
LayeredNCF.AddLayer( NCF, XYZ(0., 0., 0.559) )
#5 Ply 0
NCF.Rotate(WXYZ(XYZ(0,0,1),math.radians(-90)),XYZ(0,0,0))
LayeredNCF.AddLayer( NCF, XYZ(0., 0., 0.745) )
#6 Ply 45
NCF.Rotate(WXYZ(XYZ(0,0,1),math.radians(45)),XYZ(0,0,0))
LayeredNCF.AddLayer( NCF, XYZ(0., 0., 0.94) )
#7 Ply -45
NCF.Rotate(WXYZ(XYZ(0,0,1),math.radians(90)),XYZ(0,0,0))
LayeredNCF.AddLayer( NCF, XYZ(0., 0., 1.117) )
#8 Ply 0
NCF.Rotate(WXYZ(XYZ(0,0,1),math.radians(45)),XYZ(0,0,0))
LayeredNCF.AddLayer( NCF, XYZ(0., 0., 1.303) )
#9 Ply 0
NCF.Rotate(WXYZ(XYZ(0,0,1),math.radians(0)),XYZ(0,0,0))
LayeredNCF.AddLayer( NCF, XYZ(0., 0., 1.489) )
#10 Ply 0
NCF.Rotate(WXYZ(XYZ(0,0,1),math.radians(0)),XYZ(0,0,0))
LayeredNCF.AddLayer( NCF, XYZ(0., 0., 1.675) )
#11 Ply 90
NCF.Rotate(WXYZ(XYZ(0,0,1),math.radians(90)),XYZ(0,0,0))
LayeredNCF.AddLayer( NCF, XYZ(0., 0., 1.87) )
#12 Ply 45
NCF.Rotate(WXYZ(XYZ(0,0,1),math.radians(-45)),XYZ(0,0,0))
LayeredNCF.AddLayer( NCF, XYZ(0., 0., 2.047) )

#13 Ply 45
NCF.Rotate(WXYZ(XYZ(0,0,1),math.radians(0)),XYZ(0,0,0))
LayeredNCF.AddLayer( NCF, XYZ(0., 0., 2.233) )
#14 Ply 90
NCF.Rotate(WXYZ(XYZ(0,0,1),math.radians(45)),XYZ(0,0,0))
LayeredNCF.AddLayer( NCF, XYZ(0., 0., 2.419) )
#15 Ply 0
NCF.Rotate(WXYZ(XYZ(0,0,1),math.radians(-90)),XYZ(0,0,0))
LayeredNCF.AddLayer( NCF, XYZ(0., 0., 2.605) )
#16 Ply 0
NCF.Rotate(WXYZ(XYZ(0,0,1),math.radians(0)),XYZ(0,0,0))
LayeredNCF.AddLayer( NCF, XYZ(0., 0., 2.8) )
#17 Ply 0
NCF.Rotate(WXYZ(XYZ(0,0,1),math.radians(0)),XYZ(0,0,0))
LayeredNCF.AddLayer( NCF, XYZ(0., 0., 2.977) )
#18 Ply -45
NCF.Rotate(WXYZ(XYZ(0,0,1),math.radians(-45)),XYZ(0,0,0))
LayeredNCF.AddLayer( NCF, XYZ(0., 0., 3.163) )
#19 Ply 45
NCF.Rotate(WXYZ(XYZ(0,0,1),math.radians(90)),XYZ(0,0,0))
LayeredNCF.AddLayer( NCF, XYZ(0., 0., 3.349) )
#20 Ply 0
NCF.Rotate(WXYZ(XYZ(0,0,1),math.radians(-45)),XYZ(0,0,0))
LayeredNCF.AddLayer( NCF, XYZ(0., 0., 3.535) )
#21 Ply 90
NCF.Rotate(WXYZ(XYZ(0,0,1),math.radians(90)),XYZ(0,0,0))
LayeredNCF.AddLayer( NCF, XYZ(0., 0., 3.73) )
#22 Ply 0
NCF.Rotate(WXYZ(XYZ(0,0,1),math.radians(-90)),XYZ(0,0,0))
LayeredNCF.AddLayer( NCF, XYZ(0., 0., 3.907) )
#23 Ply 45
NCF.Rotate(WXYZ(XYZ(0,0,1),math.radians(45)),XYZ(0,0,0))
LayeredNCF.AddLayer( NCF, XYZ(0., 0., 4.093) )
#24 Ply -45
```

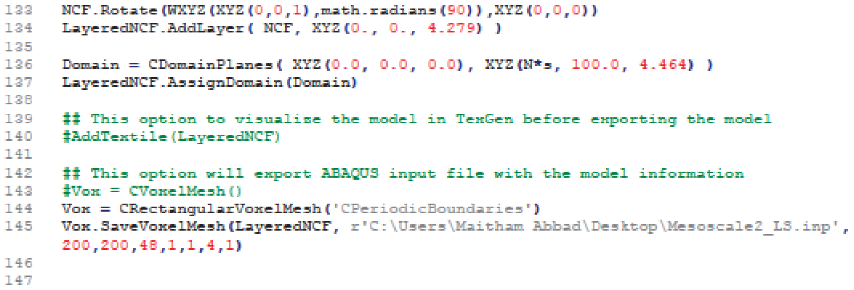

```
NCF.Rotate(WXYZ(XYZ(0,0,1),math.radians(90)),XYZ(0,0,0))
LayeredNCF.AddLayer( NCF, XYZ(0., 0., 4.279) )

Domain = CDomainPlanes( XYZ(0.0, 0.0, 0.0), XYZ(N*s, 100.0, 4.464) )
LayeredNCF.AssignDomain(Domain)

## This option to visualise the model in TexGen before exporting the model
#AddTextile(LayeredNCF)

## This option will export ABAQUS input file with the model information
#Vox = CVoxelMesh()
Vox = CRectangularVoxelMesh('CPeriodicBoundaries')
Vox.SaveVoxelMesh(LayeredNCF, r'C:\Users\Maitham Abbad\Desktop\Mesoscale2_LS.inp',
200,200,48,1,1,4,1)


```

APPENDIX B: ABAQUS (VUSDFLD) Subroutine

B.1 VUSDFLD subroutine used for a homogeneous ply model

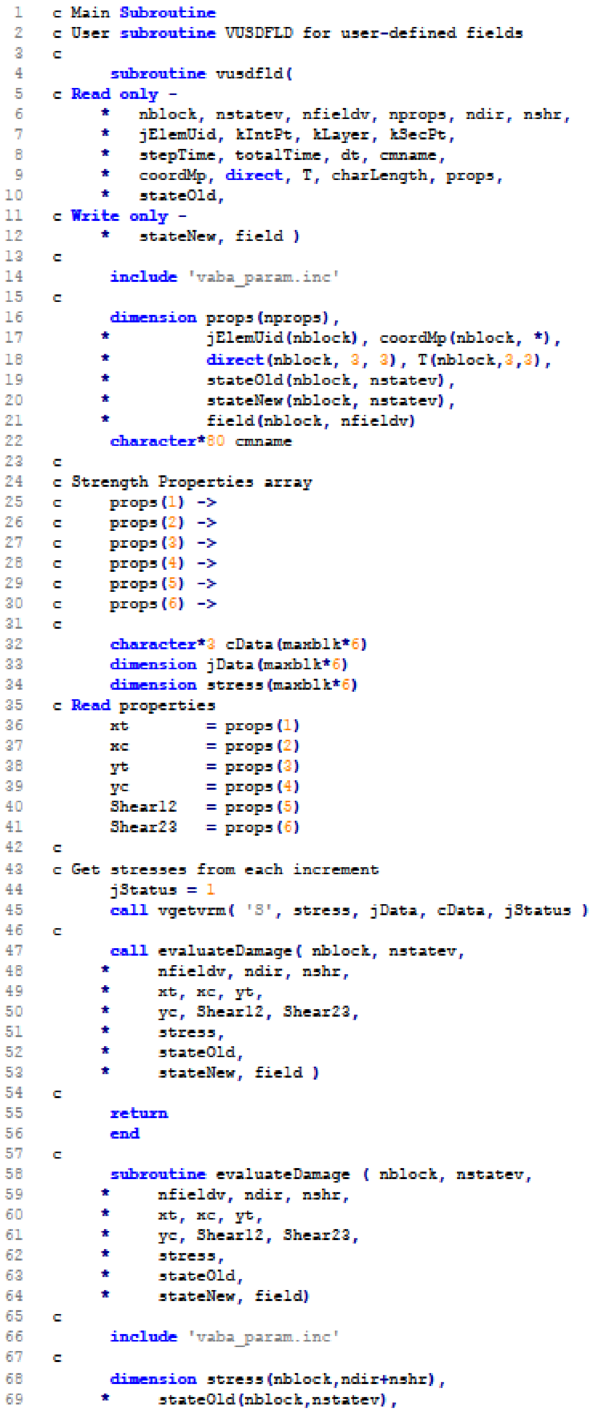

```
c Main Subroutine
c User subroutine VUSDFLD for user-defined fields
c
      subroutine vusdfld(
c Read only -
     *   nblock, nstatev, nfieldv, nprops, ndir, nshr,
     *   jElemUid, kIntPt, kLayer, kSecPt,
     *   stepTime, totalTime, dt, cmname,
     *   coordMp, direct, T, charLength, props,
     *   stateOld,
c Write only -
     *   stateNew, field )
c
      include 'vaba_param.inc'
c
      dimension props(nprops),
     *          jElemUid(nblock), coordMp(nblock, *),
     *          direct(nblock, 3, 3), T(nblock,3,3),
     *          stateOld(nblock, nstatev),
     *          stateNew(nblock, nstatev),
     *          field(nblock, nfieldv)
      character*80 cmname
c
c Strength Properties array
c     props(1) ->
c     props(2) ->
c     props(3) ->
c     props(4) ->
c     props(5) ->
c     props(6) ->
c
      character*3 cData(maxblk*6)
      dimension jData(maxblk*6)
      dimension stress(maxblk*6)
c Read properties
      xt         = props(1)
      xc         = props(2)
      yt         = props(3)
      yc         = props(4)
      Shear12    = props(5)
      Shear23    = props(6)
c
c Get stresses from each increment
      jStatus = 1
      call vgetvrm( 'S', stress, jData, cData, jStatus )
c
      call evaluateDamage( nblock, nstatev,
     *     nfieldv, ndir, nshr,
     *     xt, xc, yt,
     *     yc, Shear12, Shear23,
     *     stress,
     *     stateOld,
     *     stateNew, field )
c
      return
      end
c
      subroutine evaluateDamage ( nblock, nstatev,
     *     nfieldv, ndir, nshr,
     *     xt, xc, yt,
     *     yc, Shear12, Shear23,
     *     stress,
     *     stateOld,
     *     stateNew, field)
c
      include 'vaba_param.inc'
c
      dimension stress(nblock,ndir+nshr),
     *     stateOld(nblock,nstatev),
```

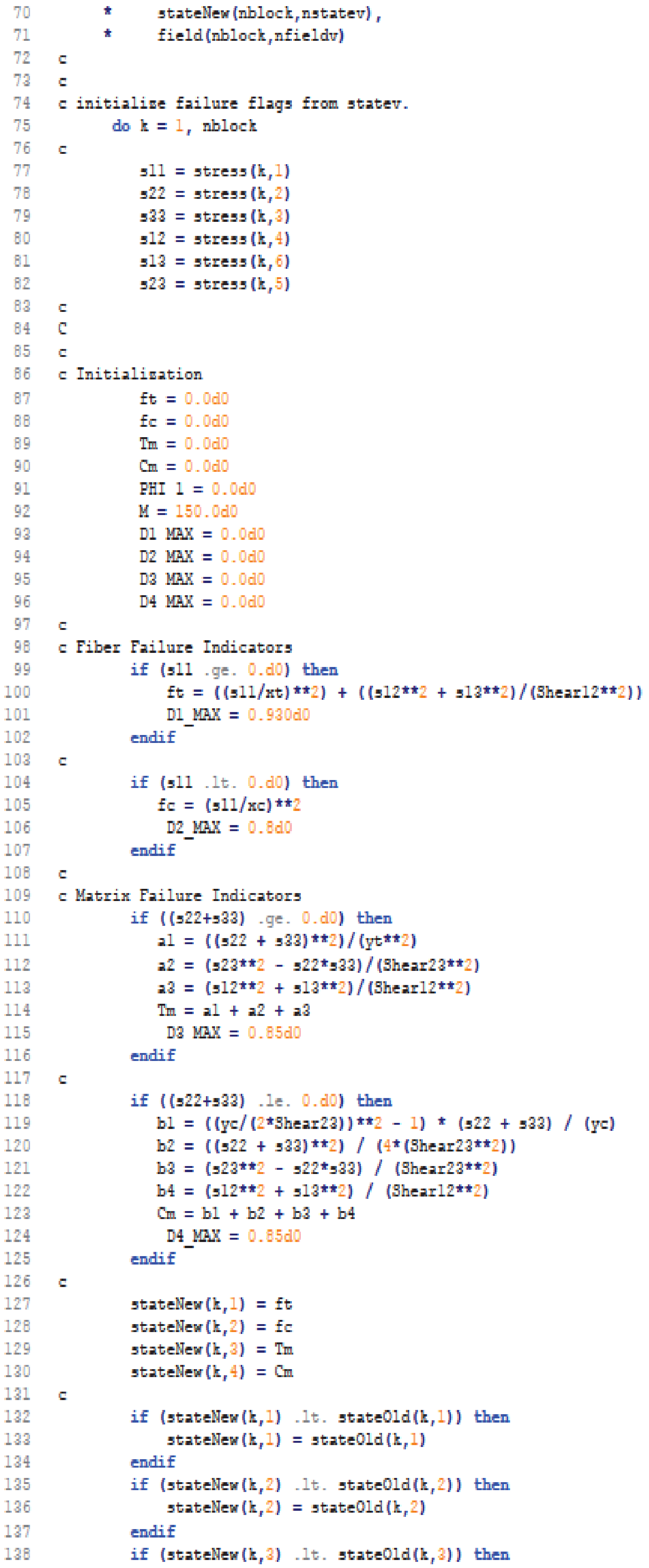

```
     *     stateNew(nblock,nstatev),
     *     field(nblock,nfieldv)
c
c
c initialize failure flags from statev.
      do k = 1, nblock
c
         s11 = stress(k,1)
         s22 = stress(k,2)
         s33 = stress(k,3)
         s12 = stress(k,4)
         s13 = stress(k,6)
         s23 = stress(k,5)
c
C
c
c Initialization
         ft = 0.0d0
         fc = 0.0d0
         Tm = 0.0d0
         Cm = 0.0d0
         PHI 1 = 0.0d0
         M = 150.0d0
         D1 MAX = 0.0d0
         D2 MAX = 0.0d0
         D3 MAX = 0.0d0
         D4 MAX = 0.0d0
c
c Fiber Failure Indicators
        if (s11 .ge. 0.d0) then
            ft = ((s11/xt)**2) + ((s12**2 + s13**2)/(Shear12**2))
            D1_MAX = 0.930d0
        endif
c
        if (s11 .lt. 0.d0) then
           fc = (s11/xc)**2
            D2_MAX = 0.8d0
        endif
c
c Matrix Failure Indicators
        if ((s22+s33) .ge. 0.d0) then
           a1 = ((s22 + s33)**2)/(yt**2)
           a2 = (s23**2 - s22*s33)/(Shear23**2)
           a3 = (s12**2 + s13**2)/(Shear12**2)
           Tm = a1 + a2 + a3
            D3 MAX = 0.85d0
        endif
c
        if ((s22+s33) .le. 0.d0) then
           b1 = ((yc/(2*Shear23))**2 - 1) * (s22 + s33) / (yc)
           b2 = ((s22 + s33)**2) / (4*(Shear23**2))
           b3 = (s23**2 - s22*s33) / (Shear23**2)
           b4 = (s12**2 + s13**2) / (Shear12**2)
           Cm = b1 + b2 + b3 + b4
            D4_MAX = 0.85d0
        endif
c
        stateNew(k,1) = ft
        stateNew(k,2) = fc
        stateNew(k,3) = Tm
        stateNew(k,4) = Cm
c
        if (stateNew(k,1) .lt. stateOld(k,1)) then
            stateNew(k,1) = stateOld(k,1)
        endif
        if (stateNew(k,2) .lt. stateOld(k,2)) then
            stateNew(k,2) = stateOld(k,2)
        endif
        if (stateNew(k,3) .lt. stateOld(k,3)) then
```

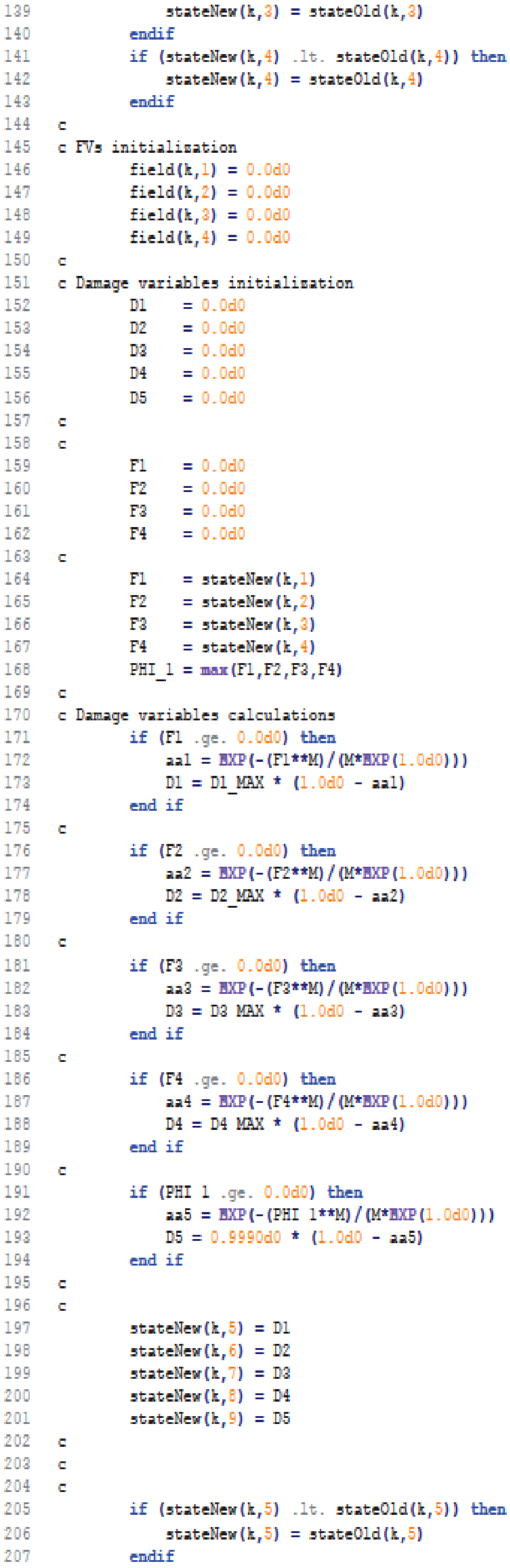

```
            stateNew(k,3) = stateOld(k,3)
         endif
         if (stateNew(k,4) .lt. stateOld(k,4)) then
            stateNew(k,4) = stateOld(k,4)
         endif
c
c FVs initialization
         field(k,1) = 0.0d0
         field(k,2) = 0.0d0
         field(k,3) = 0.0d0
         field(k,4) = 0.0d0
c
c Damage variables initialization
         D1    = 0.0d0
         D2    = 0.0d0
         D3    = 0.0d0
         D4    = 0.0d0
         D5    = 0.0d0
c
c
         F1    = 0.0d0
         F2    = 0.0d0
         F3    = 0.0d0
         F4    = 0.0d0
c
         F1    = stateNew(k,1)
         F2    = stateNew(k,2)
         F3    = stateNew(k,3)
         F4    = stateNew(k,4)
         PHI_1 = max(F1,F2,F3,F4)
c
c Damage variables calculations
         if (F1 .ge. 0.0d0) then
            aa1 = EXP(-(F1**M)/(M*EXP(1.0d0)))
            D1 = D1_MAX * (1.0d0 - aa1)
         end if
c
         if (F2 .ge. 0.0d0) then
            aa2 = EXP(-(F2**M)/(M*EXP(1.0d0)))
            D2 = D2_MAX * (1.0d0 - aa2)
         end if
c
         if (F3 .ge. 0.0d0) then
            aa3 = EXP(-(F3**M)/(M*EXP(1.0d0)))
            D3 = D3 MAX * (1.0d0 - aa3)
         end if
c
         if (F4 .ge. 0.0d0) then
            aa4 = EXP(-(F4**M)/(M*EXP(1.0d0)))
            D4 = D4 MAX * (1.0d0 - aa4)
         end if
c
         if (PHI 1 .ge. 0.0d0) then
            aa5 = EXP(-(PHI 1**M)/(M*EXP(1.0d0)))
            D5 = 0.9990d0 * (1.0d0 - aa5)
         end if
c
c
         stateNew(k,5) = D1
         stateNew(k,6) = D2
         stateNew(k,7) = D3
         stateNew(k,8) = D4
         stateNew(k,9) = D5
c
c
c
         if (stateNew(k,5) .lt. stateOld(k,5)) then
            stateNew(k,5) = stateOld(k,5)
         endif
```

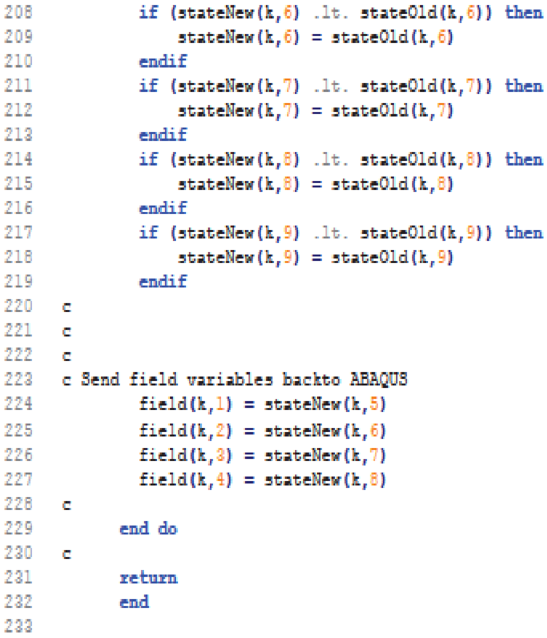

```
        if (stateNew(k,6) .lt. stateOld(k,6)) then
            stateNew(k,6) = stateOld(k,6)
        endif
        if (stateNew(k,7) .lt. stateOld(k,7)) then
            stateNew(k,7) = stateOld(k,7)
        endif
        if (stateNew(k,8) .lt. stateOld(k,8)) then
            stateNew(k,8) = stateOld(k,8)
        endif
        if (stateNew(k,9) .lt. stateOld(k,9)) then
            stateNew(k,9) = stateOld(k,9)
        endif
c
c
c
c Send field variables backto ABAQUS
        field(k,1) = stateNew(k,5)
        field(k,2) = stateNew(k,6)
        field(k,3) = stateNew(k,7)
        field(k,4) = stateNew(k,8)
c
      end do
c
      return
      end
```

B2. VUSDFLD subroutine used for a mesoscale model

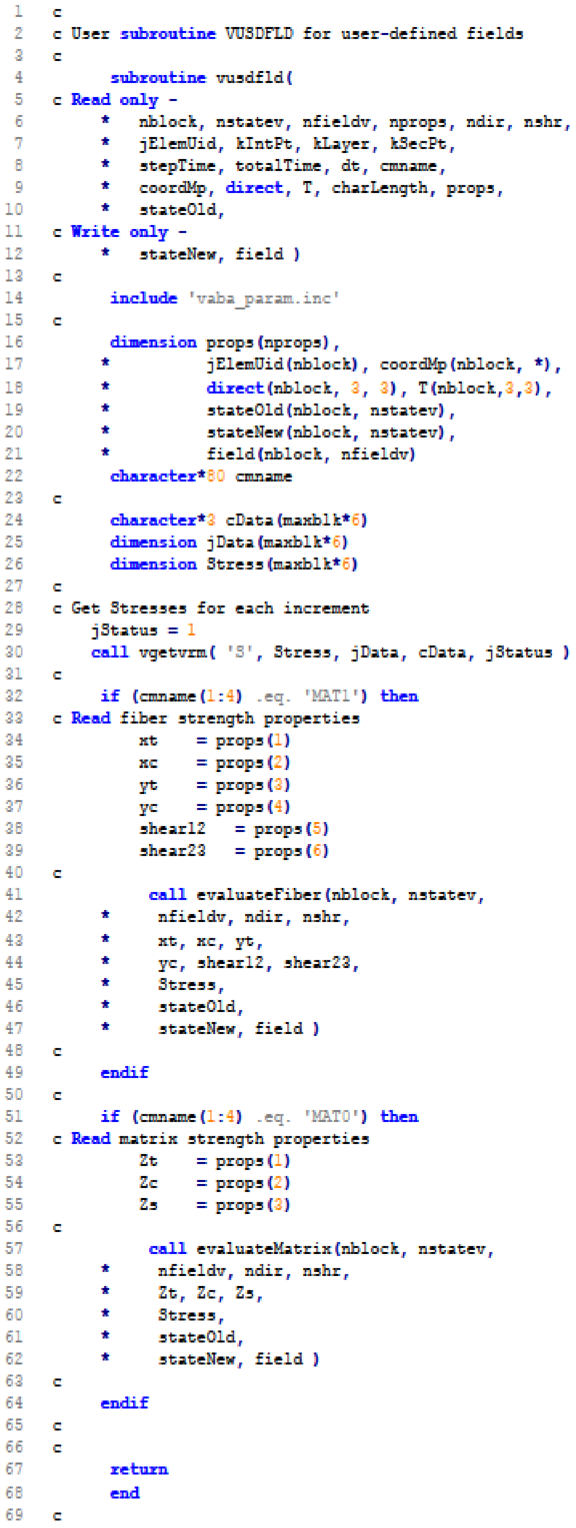

```
c
c User subroutine VUSDFLD for user-defined fields
c
      subroutine vusdfld(
c Read only -
     *   nblock, nstatev, nfieldv, nprops, ndir, nshr,
     *   jElemUid, kIntPt, kLayer, kSecPt,
     *   stepTime, totalTime, dt, cmname,
     *   coordMp, direct, T, charLength, props,
     *   stateOld,
c Write only -
     *   stateNew, field )
c
      include 'vaba_param.inc'
c
      dimension props(nprops),
     *          jElemUid(nblock), coordMp(nblock, *),
     *          direct(nblock, 3, 3), T(nblock,3,3),
     *          stateOld(nblock, nstatev),
     *          stateNew(nblock, nstatev),
     *          field(nblock, nfieldv)
      character*80 cmname
c
      character*3 cData(maxblk*6)
      dimension jData(maxblk*6)
      dimension Stress(maxblk*6)
c
c Get Stresses for each increment
    jStatus = 1
    call vgetvrm( 'S', Stress, jData, cData, jStatus )
c
     if (cmname(1:4) .eq. 'MAT1') then
c Read fiber strength properties
         xt     = props(1)
         xc     = props(2)
         yt     = props(3)
         yc     = props(4)
         shear12   = props(5)
         shear23   = props(6)
c
          call evaluateFiber(nblock, nstatev,
     *    nfieldv, ndir, nshr,
     *    xt, xc, yt,
     *    yc, shear12, shear23,
     *    Stress,
     *    stateOld,
     *    stateNew, field )
c
     endif
c
     if (cmname(1:4) .eq. 'MAT0') then
c Read matrix strength properties
         Zt     = props(1)
         Zc     = props(2)
         Zs     = props(3)
c
          call evaluateMatrix(nblock, nstatev,
     *    nfieldv, ndir, nshr,
     *    Zt, Zc, Zs,
     *    Stress,
     *    stateOld,
     *    stateNew, field )
c
     endif
c
c
      return
      end
c
```

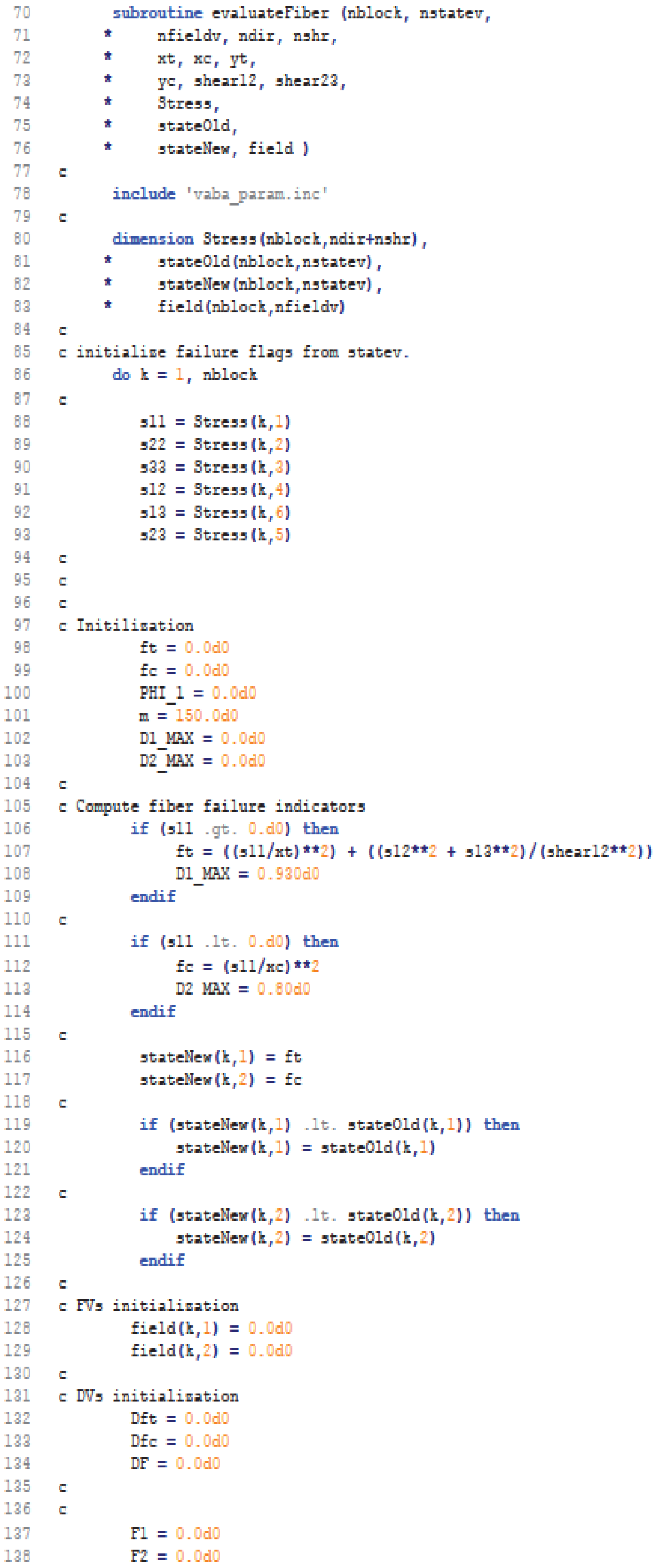

```
      subroutine evaluateFiber (nblock, nstatev,
     *     nfieldv, ndir, nshr,
     *     xt, xc, yt,
     *     yc, shear12, shear23,
     *     Stress,
     *     stateOld,
     *     stateNew, field )
c
      include 'vaba_param.inc'
c
      dimension Stress(nblock,ndir+nshr),
     *     stateOld(nblock,nstatev),
     *     stateNew(nblock,nstatev),
     *     field(nblock,nfieldv)
c
c initialize failure flags from statev.
      do k = 1, nblock
c
         s11 = Stress(k,1)
         s22 = Stress(k,2)
         s33 = Stress(k,3)
         s12 = Stress(k,4)
         s13 = Stress(k,6)
         s23 = Stress(k,5)
c
c
c
c Initilisation
         ft = 0.0d0
         fc = 0.0d0
         PHI_1 = 0.0d0
         m = 150.0d0
         D1_MAX = 0.0d0
         D2_MAX = 0.0d0
c
c Compute fiber failure indicators
        if (s11 .gt. 0.d0) then
            ft = ((s11/xt)**2) + ((s12**2 + s13**2)/(shear12**2))
            D1_MAX = 0.930d0
        endif
c
        if (s11 .lt. 0.d0) then
            fc = (s11/xc)**2
            D2_MAX = 0.80d0
        endif
c
         stateNew(k,1) = ft
         stateNew(k,2) = fc
c
         if (stateNew(k,1) .lt. stateOld(k,1)) then
             stateNew(k,1) = stateOld(k,1)
         endif
c
         if (stateNew(k,2) .lt. stateOld(k,2)) then
             stateNew(k,2) = stateOld(k,2)
         endif
c
c FVs initialization
        field(k,1) = 0.0d0
        field(k,2) = 0.0d0
c
c DVs initialization
        Dft = 0.0d0
        Dfc = 0.0d0
        DF = 0.0d0
c
c
        F1 = 0.0d0
        F2 = 0.0d0
```

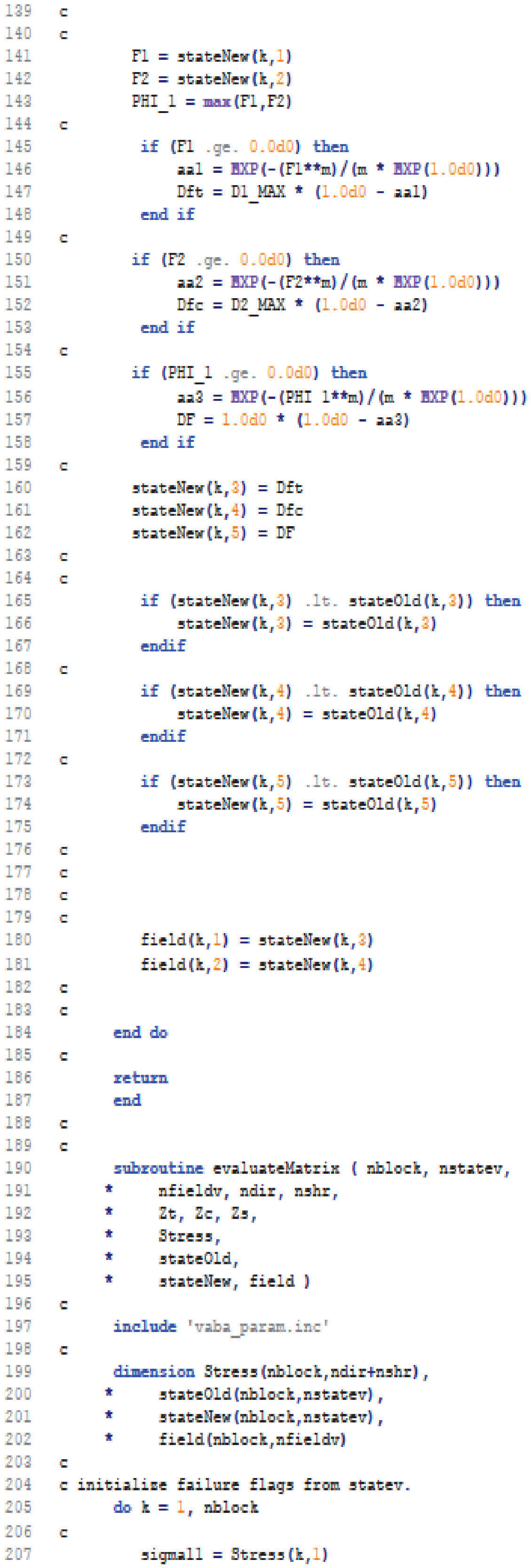

```
c
c
        F1 = stateNew(k,1)
        F2 = stateNew(k,2)
        PHI_1 = max(F1,F2)
c
         if (F1 .ge. 0.0d0) then
             aa1 = EXP(-(F1**m)/(m * EXP(1.0d0)))
             Dft = D1_MAX * (1.0d0 - aa1)
         end if
c
        if (F2 .ge. 0.0d0) then
             aa2 = EXP(-(F2**m)/(m * EXP(1.0d0)))
             Dfc = D2_MAX * (1.0d0 - aa2)
         end if
c
        if (PHI_1 .ge. 0.0d0) then
             aa3 = EXP(-(PHI 1**m)/(m * EXP(1.0d0)))
             DF = 1.0d0 * (1.0d0 - aa3)
         end if
c
        stateNew(k,3) = Dft
        stateNew(k,4) = Dfc
        stateNew(k,5) = DF
c
c
         if (stateNew(k,3) .lt. stateOld(k,3)) then
             stateNew(k,3) = stateOld(k,3)
         endif
c
         if (stateNew(k,4) .lt. stateOld(k,4)) then
             stateNew(k,4) = stateOld(k,4)
         endif
c
         if (stateNew(k,5) .lt. stateOld(k,5)) then
             stateNew(k,5) = stateOld(k,5)
         endif
c
c
c
c
         field(k,1) = stateNew(k,3)
         field(k,2) = stateNew(k,4)
c
c
      end do
c
      return
      end
c
c
      subroutine evaluateMatrix ( nblock, nstatev,
     *     nfieldv, ndir, nshr,
     *     Zt, Zc, Zs,
     *     Stress,
     *     stateOld,
     *     stateNew, field )
c
      include 'vaba_param.inc'
c
      dimension Stress(nblock,ndir+nshr),
     *     stateOld(nblock,nstatev),
     *     stateNew(nblock,nstatev),
     *     field(nblock,nfieldv)
c
c initialize failure flags from statev.
      do k = 1, nblock
c
         sigma11 = Stress(k,1)
```

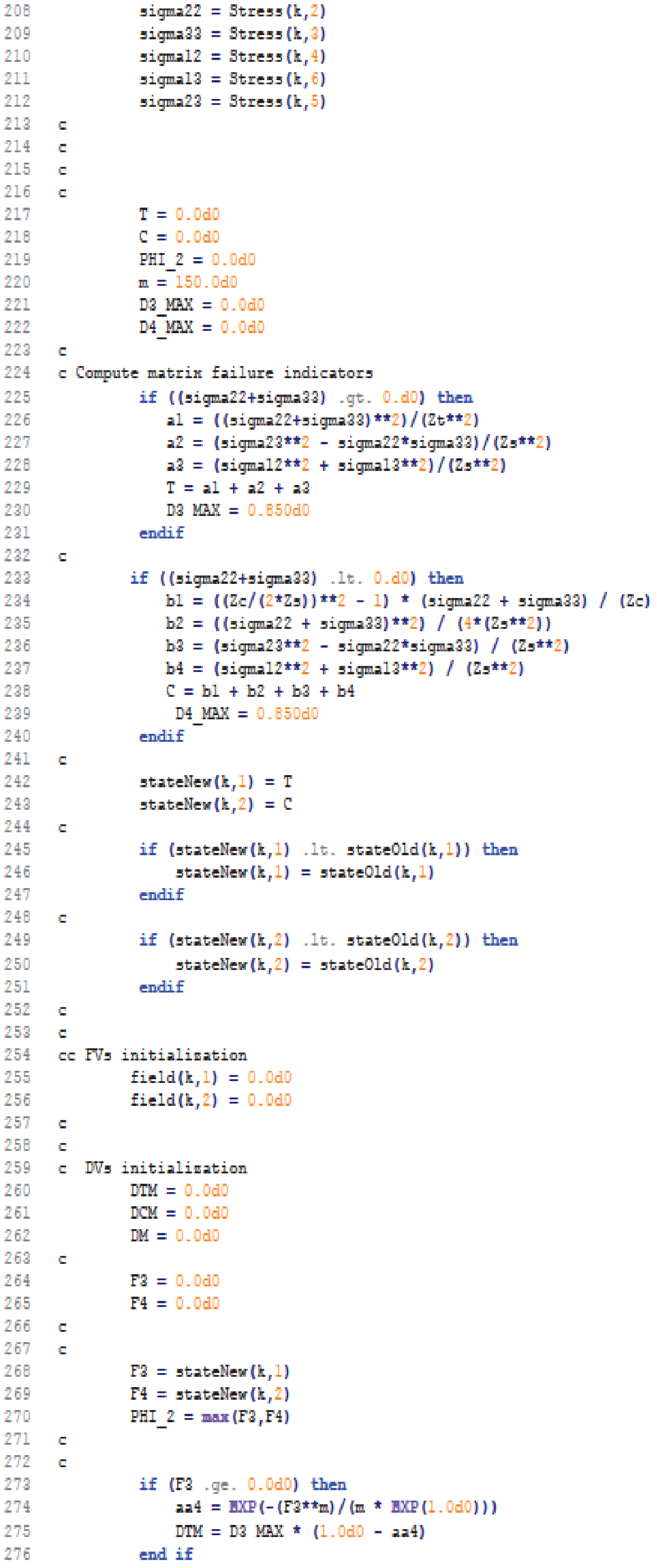

```
         sigma22 = Stress(k,2)
         sigma33 = Stress(k,3)
         sigma12 = Stress(k,4)
         sigma13 = Stress(k,6)
         sigma23 = Stress(k,5)
c
c
c
c
         T = 0.0d0
         C = 0.0d0
         PHI_2 = 0.0d0
         m = 150.0d0
         D3_MAX = 0.0d0
         D4_MAX = 0.0d0
c
c Compute matrix failure indicators
         if ((sigma22+sigma33) .gt. 0.d0) then
            a1 = ((sigma22+sigma33)**2)/(Zt**2)
            a2 = (sigma23**2 - sigma22*sigma33)/(Zs**2)
            a3 = (sigma12**2 + sigma13**2)/(Zs**2)
            T = a1 + a2 + a3
            D3 MAX = 0.850d0
         endif
c
        if ((sigma22+sigma33) .lt. 0.d0) then
            b1 = ((Zc/(2*Zs))**2 - 1) * (sigma22 + sigma33) / (Zc)
            b2 = ((sigma22 + sigma33)**2) / (4*(Zs**2))
            b3 = (sigma23**2 - sigma22*sigma33) / (Zs**2)
            b4 = (sigma12**2 + sigma13**2) / (Zs**2)
            C = b1 + b2 + b3 + b4
             D4_MAX = 0.850d0
         endif
c
         stateNew(k,1) = T
         stateNew(k,2) = C
c
         if (stateNew(k,1) .lt. stateOld(k,1)) then
             stateNew(k,1) = stateOld(k,1)
         endif
c
         if (stateNew(k,2) .lt. stateOld(k,2)) then
             stateNew(k,2) = stateOld(k,2)
         endif
c
c
cc FVs initialization
        field(k,1) = 0.0d0
        field(k,2) = 0.0d0
c
c
c  DVs initialization
        DTM = 0.0d0
        DCM = 0.0d0
        DM = 0.0d0
c
        F3 = 0.0d0
        F4 = 0.0d0
c
c
        F3 = stateNew(k,1)
        F4 = stateNew(k,2)
        PHI_2 = max(F3,F4)
c
c
         if (F3 .ge. 0.0d0) then
             aa4 = EXP(-(F3**m)/(m * EXP(1.0d0)))
             DTM = D3 MAX * (1.0d0 - aa4)
         end if
```

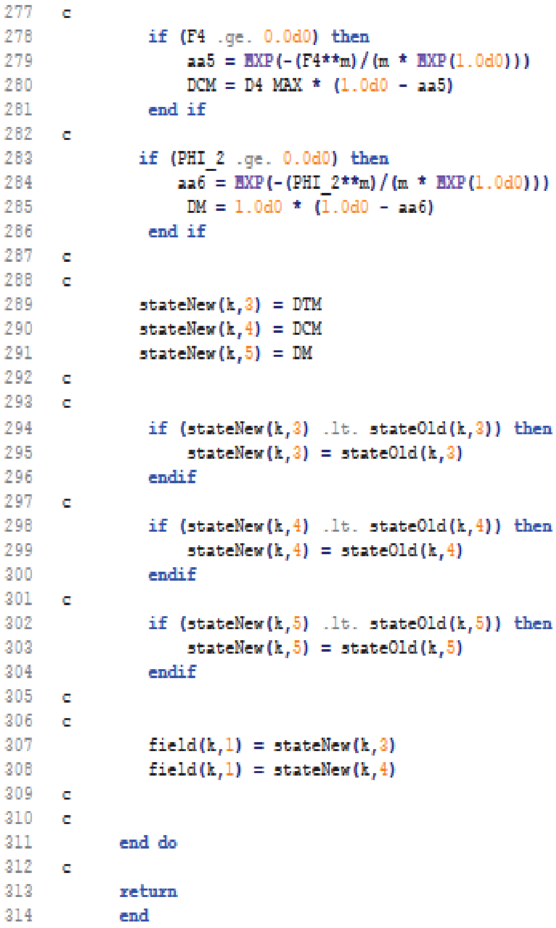

```
c
         if (F4 .ge. 0.0d0) then
             aa5 = EXP(-(F4**m)/(m * EXP(1.0d0)))
             DCM = D4 MAX * (1.0d0 - aa5)
         end if
c
        if (PHI_2 .ge. 0.0d0) then
            aa6 = EXP(-(PHI_2**m)/(m * EXP(1.0d0)))
             DM = 1.0d0 * (1.0d0 - aa6)
         end if
c
c
        stateNew(k,3) = DTM
        stateNew(k,4) = DCM
        stateNew(k,5) = DM
c
c
         if (stateNew(k,3) .lt. stateOld(k,3)) then
             stateNew(k,3) = stateOld(k,3)
         endif
c
         if (stateNew(k,4) .lt. stateOld(k,4)) then
             stateNew(k,4) = stateOld(k,4)
         endif
c
         if (stateNew(k,5) .lt. stateOld(k,5)) then
             stateNew(k,5) = stateOld(k,5)
         endif
c
c
         field(k,1) = stateNew(k,3)
         field(k,1) = stateNew(k,4)
c
c
      end do
c
      return
      end
```

BIOGRAPHY OF THE AUTHOR

Maitham Alabbad was born in Alahsa, Saudi Arabia. He received his primary education in Saudi Arabia and graduated from Aljafr High School in 2010. He obtained his B.S. degree in Mechanical Engineering from the University of Maine in 2017. Maitham worked as a graduate research assistant in the field of Solid Mechanics, and as a graduate teaching assistant for the Department of Mechanical Engineering. Maitham Alabbad is a candidate for the Master of Science degree in Mechanical Engineering from the University of Maine in May 2020.